A Search for $\nu_\mu \rightarrow \nu_\tau$ Neutrino Oscillations in the $\tau \rightarrow \rho$ Decay Channel Using the NOMAD Detector

A thesis presented
by

DAVID CLARK DANIELS

to

The Department of Physics

in partial fulfillment of the requirements
for the degree of

Doctor of Philosophy

in the subject of

Physics

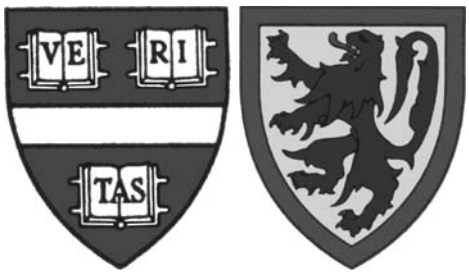

Harvard University
Cambridge, Massachusetts
February 2000

Abstract

The standard model of particle physics includes three flavors of massless neutrinos. If neutrinos in fact have mass and non-zero mixing angles, one flavor may oscillate into another. A rich panoply of experiments have searched for this phenomenon using different types of neutrinos, from both man-made and extraterrestrial sources, over a wide range of energies, and employing a variety of detection techniques. Some recent experiments have claimed positive results in the search for neutrino oscillations.

The NOMAD detector examined the neutrino beam at the CERN SPS for four years, from 1995 to 1998. These data are analyzed in a search for $\nu_\mu \rightarrow \nu_\tau$ oscillations in the $\tau \rightarrow \rho$ decay channel. The analysis employs a multidimensional kinematic likelihood function to separate signal events from backgrounds.

The analysis finds no evidence of neutrino oscillations, and sets upper limits on the coupled parameters $\sin^2 2\theta$ and Δm^2 of $\sin^2 2\theta < 8.79 \times 10^{-3}$ for large Δm^2, and $\Delta m^2 < 3.75$ eV^2/c^4 at $\sin^2 2\theta = 1$.

Contents

List of Figures

List of Tables

Acknowledgments

There are a large number of people to whom I am indebted in one way or another for helping me write this thesis. It would be irresponsible not to give them all credit, but as I will almost certainly forget one or two people here, I apologize in advance if I fail to mention someone.

I am especially thankful to those people who directly contributed to the work presented in this thesis: to my advisor, Gary Feldman, whose idea it was to undertake the $\tau \rightarrow \rho$ analysis in the first place, and who invariably had fixes for my "insurmountable" problems, I especially want to thank for his help with the statistical analysis; to Mark Messier, for reading and offering useful criticisms on Chapter 1; to Peter Hurst, who never complained when I pestered him with questions about NOMAD, and always listened patiently when I needed someone to hear my ideas (thanks especially for your advice about taking thesis defenses); to Fred Weber, for helping me to understand the CALISTO analysis environment; to Emmanuel Tsesmelis for getting me started working on NUBEAM, and to Thomas Weisse, for guiding me through its innards "way back when."

There are a lot of others who, though they may not have directly contributed to this work, certainly made the graduate school experience a lot more pleasant. Without some of them I may not have made it at all. Along this line I would like to thank Sanjib Mishra, for encouraging me to enroll at Harvard in the first place, and for inspiration along the way when I lacked it; Tom Dignan, who gave me my first warning, and to whom I should have listened sooner; Guy Sciacca at HEPL, who was the one person at Harvard I knew who really understood how this place worked; Mary Lampros in the physics department, forever cheerful, who always reminded me when deadlines were approaching or when forms needed to be filled out; Sarah Pohlen and Paul Callan, for helping me get through our classes together, and for good times to boot; and Jim Bensinger and Kevan Hashemi, for much help and a very productive time at Brandeis building the laser alignment system for NOMAD STAR, and to Allan Wellenstein who kept me sane when we had to install it.

Last, but certainly not least, I want to thank my wife, who I made endure far more than she should have had to, for not giving up on me in the face of it all.

Cosmic Gall

Neutrinos, they are very small
They have no charge and have no mass
And do not interact at all.
The earth is just a silly ball
To them, through which they simply pass,
Like dustmaids down a drafty hall
Or photons through a sheet of glass.
They snub the most exquisite gas,
Ignore the most substantial wall,
Cold-shoulder steel and sounding brass,
Insult the stallion in his stall,
And, scorning barriers of class,
Infiltrate you and me! Like tall
And painless guillotines, they fall
Down through our heads into the grass.
At night, they enter at Nepal
And pierce the lover and his lass
From underneath the bed—you call
It wonderful; I call it crass.

—John Updike
from "Telephone Poles and Other Poems," New York: A. Knopf, 1963.

Introduction

This thesis presents a search for $\nu_\mu \rightarrow \nu_\tau$ neutrino oscillations in the accelerator-based NOMAD experiment. If confirmed, neutrino oscillation would represent the first real departure from Standard Model physics. Although there have been numerous hints, including strong support from recent atmospheric neutrino experiments, no *direct* evidence has yet been found. The NOMAD experiment is capable of detecting the τ lepton that results from ν_τ charged current interactions, and is therefore able to make such a direct confirmation of $\nu_\mu \rightarrow \nu_\tau$ oscillations.

Apart from actually detecting them, studying neutrino oscillations in NOMAD is important for a number of reasons. First, with its high statistics, NOMAD is sensitive to a large region of the ($\sin^2 2\theta$,Δm^2) plane, especially at low $\sin^2 2\theta$. Results from NOMAD explore this region and serve as cross checks for other experiments, such as CHORUS. Finally, the analysis techniques developed by the NOMAD collaborators and used in this thesis can serve as a template for similar analyses in future long-baseline accelerator neutrino experiments.

Studying $\nu_\mu \rightarrow \nu_\tau$ oscillations in the $\tau \rightarrow \rho$ decay channel in NOMAD is a compelling challenge. The neutrino beam used by the experiment is composed mostly of ν_μ and contains an insignificant amount of ν_τ, and is therefore an ideal environment in which to search for the appearance of ν_τ. The decay chain $\tau \rightarrow \rho$ is compelling because of its large branching fraction (25%), larger than any other single τ decay mode. It is a challenge because of the ρ's complicated cascade of decays which makes the identification difficult, and the large hadronic background to the signal. The analysis presented in this thesis aims to overcome these difficulties and make a meaningful measurement.

The thesis is organized into four chapters. The first begins with a history of neutrinos, discusses some of the phenomenology behind neutrino mass and oscillations, and reviews the relevant experimental searches for oscillation. Chapter 2 describes the apparatus and data used for this analysis. The apparatus consists of the neutrino beamline at CERN and the NOMAD detector itself. The data collection and processing is then briefly explained. The third chapter describes the analysis. The general analytic methods are described, the backgrounds are illustrated, and the particle identification is detailed. The chapter concludes with a detailed list of all cuts used and their effects on the signal and backgrounds. The final chapter presents the conclusions from the analysis outlined in Ch. 3.

Chapter 1

Background

In this chapter, the groundwork is laid for the rest of the thesis. First, a brief history of major neutrino discoveries is given. Then the role of neutrino mass is discussed, followed by the phenomenology of neutrino oscillations. Finally, the relevant previous experimental results are reviewed.

1.1 History of Neutrinos

Neutrinos have played an integral part in the development of physics in the 20^{th} century. Non-participatory in the electromagnetic or strong nuclear forces, neutrinos are ideal probes of the weak nuclear force. Produced copiously in the Sun and in other astronomical events, they have begun to play a large role in astrophysics and cosmology. They have been intensely studied to understand the inner workings of our sun, and have been proposed as at least a component of the dark matter which makes up most of the mass of the universe.

Neutrinos were originally proposed as a "desperate remedy" to the problem of nuclear β-decay. According to nuclear theory of the 1920's, β-decay was the two-body decay of a nucleus wherein the atomic mass remained the same but the atomic number changed by one unit:

$$(A, Z) \rightarrow (A, Z \pm 1) + e^{\mp}. \tag{1.1}$$

Momentum conservation equated the momentum of the electron with that of the recoiling nucleus. Given the difference in masses between the incident and final nuclei, $Q \simeq M(A, Z) - M(A, Z \pm 1)$, the predicted energy spectrum of the electron which should be a spike at nearly the value Q. Instead, the observed spectrum was a continuum peaking at $\sim Q/2$ with an endpoint near Q. While Niels Bohr concluded that energy conservation must therefore be broken [1], Wolfgang Pauli noted that an unobserved (electrically neutral) particle emitted along with the electron could induce

such a spectrum. In a now-famous letter[1] dated December 1930 Pauli proposed a new elementary particle, which he called the *neutron*.

Pauli promoted his idea at several physics meetings after that, speculating about the properties of this neutron. In his original letter he had stated that the neutron should have spin-$\frac{1}{2}$, mass on the order of the electron mass, a small magnetic moment, and about ten times the penetrating capacity of a gamma ray. In June 1931 at an American Physical Society meeting in Pasadena he claimed that his neutrons "should have an angular momentum $\frac{1}{2}h/2\pi$ and also a magnetic moment, but no charge. They are kept in the nucleus by magnetic forces and are emitted together with beta-rays in radioactive disintegration." [3] In October of that year, at a meeting in Rome organized by Enrico Fermi, he discussed the new particle with both Bohr, who vehemently opposed it, and Fermi, who favored the idea. Although his neutron concept was widely known among physicists by then, Pauli first presented it for publication at the Seventh Solvay Conference [4] in October 1933. It is unclear whether Pauli still held the belief that his neutrons were nuclear constituents at that point, but in the published account he claimed no longer to favor the idea that they had a magnetic moment. That massless particles could be *created* in conjunction with electron emission in β-decay was proposed [5] in the same year by Francis Perrin, who had also attended the Solvay Conference.

It was Fermi who gave the neutrino its name. In 1932, James Chadwick had discovered [6] what we now know as the neutron in beryllium decays, for which he was awarded the Nobel prize in 1935. This clearly was not Pauli's particle, though, since its mass was close to the proton's and not the electron's. In order to distinguish the two neutrons, then, Carlson and Oppenheimer referred [7] to the Pauli particle as the *magnetic neutron*, because of the assumption that it would have a non-zero magnetic moment. Perhaps because he was by then trying to decouple the existence of his particle from the assertion of its magnetic moment, Pauli used the term "neutrino"[2] in his presentation at the Solvay Conference, a name he claimed was suggested by the Italian Fermi.

The next year Fermi published [8] his theory of β-decay, in which not only the existence, but also the properties of the neutrino are assumed. His Hamiltonian described β-decay as a product of two vector currents, one relating the nucleons and the other connecting the leptons:

$$\mathcal{H} = \frac{G_F}{\sqrt{2}} \left(\psi_p^\dagger j_\mu \psi_n\right) \left(\psi_e^\dagger j^\mu \psi_\nu\right), \tag{1.2}$$

where ψ stands for a fermion field (spinor), j is a matrix which relates spinors to each other, and G_F is the interaction coupling strength. Called by Victor Weisskopf [9] "the first example of modern field theory," Fermi's theory of the weak interaction was im-

[1] An English translation of Pauli's letter may be found in Ref. [2].

[2] Italian for "little neutral one."

mediately accepted because of its excellent description of the electron energy spectrum as measured by experiment. Based on the success of the theory, Bohr was even compelled to retract [10] his belief that energy was not conserved in β-decays. Thus, the neutrino's existence was established long before it was ever seen.

Interestingly, the first direct evidence [11] for the existence of the neutrino came in the same year that parity violation in weak interactions was found, demonstrating that the current could not have the vector form given by Fermi (Eq. 1.2). In 1956 Clyde Cowan and Fred Reines, working at the Savannah River nuclear reactor in South Carolina, were able to observe the so-called "inverse β-decay" reaction:

$$^{37}\mathrm{Cl} + \overline{\nu} \rightarrow {}^{37}\mathrm{Ar} + e^{+}. \tag{1.3}$$

Bruno Pontecorvo had first suggested [12] the chlorine reaction above, and Luis Alvarez further developed [13] this suggestion into a detector design. Reines' initial plan had been to try to observe neutrinos from a nuclear explosion, and he had even approached Fermi about such a possibility at Los Alamos; but he eventually decided that a reactor would provide a more stable source. Initial work [14] at the Hanford, Washington reactor was published in 1953, but that showed only a 2σ signal above a large background from cosmic rays. The Savannah River facility provided them with far better shielding and reactor neutrino flux, the lab being placed 12 meters underground and only 11 meters from the reactor center. The detector Cowan and Reines used consisted of two modestly-sized (~200 liter) tanks of a cadmium chloride solution in water. Using these they were able to detect the γ-ray emitted when a positron, liberated as per Eq. 1.3, annihilated with an electron, followed closely by the photon emitted when a cadmium nucleus de-excited after absorbing the neutron. Reines was awarded the Nobel prize for this work in 1995; Cowen had already died.

By the late 1950's parity non-conservation in weak interactions had been observed [15] and the two-component theory [16] of neutrinos was proposed to explain it. In the two-component theory neutrinos are massless by definition, and their helicities are fixed, although the sign of the helicity was unknown. It remained to Goldhaber [17] in 1958 to determine experimentally that neutrinos are in fact left-handed, a fact that was incorporated into the $V-A$ theory of Feynman and Gell-Mann [18] and Sudarshan and Marshak [19].

The discovery that the ν_μ and the ν_e were separate particles came in the 1960's. If the neutrinos associated with β-decay and the neutrinos associated with pion decay were the same, then the decay $\mu \rightarrow e + \gamma$ should occur [20] at a rate of about 10^{-4} times the rate for $\mu \rightarrow e + \nu + \overline{\nu}$, yet it had been measured [21] to be less than 10^{-8}. Around 1960, Pontecorvo [22] and Melvin Schwartz [23] independently proposed the idea of making beams of neutrinos from the decays-in-flight of pions and kaons produced at particle accelerators. In 1962, a team from Columbia University, which included Schwartz, constructed a neutrino beam and found that upon reinteraction these

neutrinos always produced muons, not a combination of muons and electrons. This result [24] confirmed that the two types of neutrinos were separate, and the ν_μ was established. In 1988, Jack Steinberger, Leon Lederman, and Schwartz were awarded the Nobel Prize for this work.

The discovery of a third lepton family [25] in 1975 implied the existence of the tau neutrino (ν_τ), although it has yet to be directly observed. By measuring the width of the Z-boson mass distribution in 1989, collaborations at SLAC [26] and CERN [27] were able to determine that there can be no other weakly interacting light neutrinos. The current best value [28] of the number of light neutrino species is 2.994 ± 0.012.

The production of neutrino beams from high energy particle accelerators has proved to be an invaluable tool in the study of neutrinos. In 1973, using a ν_μ beam at CERN, the Gargamelle collaboration first discovered [29] evidence for the neutral weak current, which was an important confirmation of electroweak theory. Furthermore, by measuring the ratio of neutral current (NC) to charged current (CC) interactions for neutrinos and anti-neutrinos, they were able to measure the weak mixing angle θ_W. Later neutrino experiments at CERN, Brookhaven, and Fermilab provided better measurements of $\sin^2\theta_W$, which remained the most precise values until LEP began running in the late 1980's. A neutrino beam experiment at Brookhaven in 1975 was the first to see [30] charmed baryons. Neutrino experiments at accelerators have tested the lepton number conservation laws, looked for flavor changing neutral currents (FCNC), and measured the nuclear structure functions [31].

Large underground particle detectors, some of which were initially built to look for proton decay, have proved to be ideal "neutrino telescopes" as well. Through widely varying detection techniques (water Cherenkov, radiochemical, iron calorimetric), neutrinos coming from the Sun, from distant astrophysical events (supernovae, e.g.), and from cosmic ray showers in our atmosphere can be detected. In 1987 neutrinos from a supernova explosion (SN 1987A) were seen for the first time in two water Cherenkov detectors: Kamiokande [32] and IMB [33].

So, what began in the 1930's as a desperate remedy has become a familiar set of three particles (ν_e, ν_μ, ν_τ) in the Standard Model today. Beams of these particles produced at accelerators have been essential probes of the weak interaction, and extraterrestrial neutrinos can shed light on astrophysical processes.

1.2 Neutrino Mass

In the Standard Model of particle physics, the neutrino properties are clearly prescribed: they are particles of intrinsic spin $\frac{1}{2}\hbar$ (fermions), zero electric charge, and no mass. This last property is motivated entirely by experimental considerations, the mass terms which would ordinarily arise in the Standard Model Lagrangian being set to zero. There is no good theoretical justification for the masslessness of the neutrinos. The only other

massless particle, the photon, must be so in order to satisfy gauge invariance, but there is no such principle that requires massless neutrinos. This then begs the question "If neutrinos are not required to be massless, why are they?" or alternatively, "Do neutrinos in fact have mass?"

From the beginning, Fermi recognized that the neutrino must at least be very light or the endpoint of the β-decay electron spectrum would be deformed; but he did not assume it would be exactly massless. By the 1950's it was known [34] that the neutrino's mass was much smaller than the electron's, and the authors of the two-component neutrino theory assumed it to be zero. Conversely, in the $V-A$ theory of weak interactions, neutrinos were treated like all other massive fermions, allowing the possibility of mass but not requiring it.

1.2.1 Dirac and Majorana masses

The charged quarks and leptons are Dirac particles; that is, they are described by four-component complex spinors which obey the Dirac equation. One might assume that if neutrinos were massive they would be similar; however, since neutrinos have no electric charge, there is another possibility. Neutrinos could be described by a two-component spinor, in a way first suggested [37] by Ettore Majorana in 1937.

To understand Dirac particles, it is instructive to consider a generic charged fermion ℓ with mass $m_\ell > 0$. The four components of its Dirac spinor represent the left and right helicity states of the particle and antiparticle:

$$\ell^D = \begin{bmatrix} \ell_L \\ \ell_R \\ \overline{\ell}_L \\ \overline{\ell}_R \end{bmatrix} . \tag{1.4}$$

Suppose one had an ℓ moving with velocity v in the direction $\hat{z}$ in some inertial reference frame $\mathcal{F}_1$, with its spin aligned in the opposite direction, i.e. along $-\hat{z}$. To an observer in this frame, this appears to be the state ℓ_L. Now, because the particle ℓ has mass, it is possible to boost into another reference frame $\mathcal{F}_2$ moving along $+\hat{z}$ with speed greater than v. To an observer in frame $\mathcal{F}_2$, the particle appears to be moving in the direction $-\hat{z}$, and its spin is aligned with its velocity. This represents a right-handed state, but we have two right-handed states to choose from: ℓ_R and $\overline{\ell}_R$. In the case of a charged particle there is no ambiguity, since charge is Lorentz-invariant. The states before and after the Lorentz boost must have the same charge; so, if we had ℓ_L in frame $\mathcal{F}_1$, we must have ℓ_R in frame $\mathcal{F}_2$.

If neutrinos have mass and are Dirac particles, then they are described by a four-component spinor as well, the components being ν_L, ν_R, $\overline{\nu}_L$, and $\overline{\nu}_R$. Then, in the above example, the Lorentz-boosted state is ν_R, in direct analogy to the charged lepton case. One important point is that if neutrinos are Dirac particles, a Lorentz boost con-

serves lepton number. This is in agreement with all experimental tests of lepton number conservation to date.

Majorana particles are massive particles with no Lorentz-invariant quantity (like electric charge) to distinguish particle from anti-particle. They only have two degrees of freedom, i.e. they are described by two-component spinors, which for a neutrino might have states ν_L and $\overline{\nu}_R$. So, in the Lorentz boost example above, the original ν_L would be boosted into a $\overline{\nu}_R$, its own anti-particle. It is therefore evident that if neutrinos are Majorana particles, lepton number must not be conserved.

The difference between Dirac and Majorana particles is similar to the difference between the charged and neutral pions. The charged pions are represented by a complex scalar field (two degrees of freedom), and the π^0 by a real scalar field (one d.o.f.). Since there is no quantum number which distinguishes between particle and anti-particle for the π^0, it is said to be its own anti-particle.

Weyl particles represent another type of fermion modeled by a two-component spinor, but they should be contrasted with Majorana particles. Both types of particles might have the same two components, but Weyl particles are explicitly massless. One cannot therefore transform a Weyl particle to its anti-particle via a Lorentz boost.

It should be noted that in the Standard Model it is very difficult to distinguish Dirac from Majorana neutrinos. The weak Lagrangian only involves the left-handed components of neutrinos, and in the limit of vanishing masses there is no difference between Dirac and Majorana particles at all. Certain lepton number violating processes (neutrinoless double β-decay, e.g.) can only occur if neutrinos have Majorana mass, but for the measurement of this thesis there is no such distinction.

1.2.2 Direct limits on neutrino masses

Most of direct limits on the mass of the ν_e (m_{ν_e}) to date come from fits to the endpoint of the energy spectrum in tritium β-decay. These experiments actually measure m^2, not m, and most best fits to data suggest a negative value of m^2, which is clearly non-physical. Furthermore, recent groups have reported that unknown effects lead to an excess of events in the electron energy spectrum near the the endpoint. Nonetheless, the Particle Data Group (PDG) has quoted an upper limit on m_{ν_e} of 15 eV/c^2 with the following caveat:

> Given the status of the tritium results, we find no clear way to set a meaningful limit on m_{ν_e}. On the other hand, a mass as large as 10–15 eV would probably cause detectable spectrum distortions near the endpoint. [28]

An interesting way to set a limit on m_{ν_e} presented itself with the detection of neutrinos from SN 1897A. Massive particles of differing energies should travel at different speeds, so the correlation of energies with arrival times for the neutrinos detected from

Neutrino	Mass Limit
ν_e	15 eV/c^2
ν_μ	170 keV/c^2
ν_τ	18.2 MeV/c^2

Table 1.1: Direct neutrino mass limits.

this supernova should give an estimate of m_{ν_e}. The PDG gives one conservative limit based on this approach of $m_{\nu_e} < 23$ eV/c^2.

The best direct limit on the muon neutrino mass (m_{ν_μ}) is from a pion decay ($\pi^+ \rightarrow \mu^+\nu_\mu$) experiment [35], where the mass is inferred from the value of the muon momentum in direct analogy to the way m_{ν_e} is measured in β-decay. The upper limit from this experiment is $m_{\nu_\mu} < 170$ keV/c^2. More stringent limits (down to a few keV/c^2) can be made using cosmological arguments, but these are highly model-dependent, and often only hold for Dirac neutrinos (discussed in Sec. 1.2.1).

Measuring m_{ν_τ} is much more difficult than measuring either of the other two neutrinos' masses. Constructing a τ-emitter (like tritium is for ν_e or pions are for ν_μ) is harder because of the large mass of the τ. In addition, while the electron is stable and the muon has a relatively long lifetime, the τ decays almost instantly at practical laboratory energies. Instead, the most straightforward technique for measuring the mass is to reconstruct the "missing" energy and momentum in hadronic final states of τ decays. In the hadronic decay modes, only the ν_τ will escape detection, so the missing energy and momentum belongs to it. (In leptonic τ decays, there are two neutrinos which carry away a higher fraction of the energy.) The difference of the squares of energy and momentum gives $m^2_{\nu_\tau}$. Using this approach, the ALEPH collaboration has put the best limit [36] on the $\nu_\tau$mass: $m_{\nu_\tau} < 18.2$ MeV/c^2.

The best direct mass limits obtained for the three species of neutrinos are summarized in Tab. 1.1.

1.3 Neutrino Oscillations

Neutrinos are created in weak charged current (CC) interactions, which produce eigenstates of the weak interaction (sometimes called flavor neutrinos): $|\nu_\alpha\rangle$, $\alpha \in \{e, \mu, \tau\}$. The physical states (mass eigenstates) are in general not identical to the weak eigenstates, but they can be related by a unitary transformation. For n states $|\nu_1\rangle \ldots |\nu_n\rangle$

with masses $m_1 \ldots m_n$, and ignoring time evolution, we have:

$$|\nu_\alpha\rangle = \sum_{k=1}^{n} U_{\alpha k} |\nu_k\rangle \,, \tag{1.5}$$

where U is a unitary matrix.

1.3.1 Vacuum oscillations

1.3.1.1 General case

A ν_α at its moment of creation is a superposition of n mass states.[3] If the neutrino is produced in a definite momentum eigenstate with eigenvalue P, then the mass states will have energies $E_k = \sqrt{P^2 + m_k^2}$ with $k = 1 \ldots n$. So, if the masses are non-degenerate, the mass states will have different energies. Since it is these physical mass eigenstates (not the flavor states) which evolve freely in time, the time evolution of the flavor neutrinos is:

$$|\nu_\alpha(t)\rangle = \sum_{k=1}^{n} e^{-iE_k t} U_{\alpha k} |\nu_k\rangle \,. \tag{1.6}$$

If at least some of the masses m_n are different from each other, these mass states will evolve differently in time so that $|\nu_\alpha(t > 0)\rangle \neq |\nu_\alpha(0)\rangle$. The amplitude for finding a flavor state $|\nu_\beta\rangle$ at time t in an originally pure beam of $|\nu_\alpha\rangle$ is:

$$\begin{aligned} \langle \nu_\beta | \nu_\alpha(t) \rangle &= \sum_{j,k} \langle \nu_j | \, U^\dagger_{j\beta} e^{-iE_k t} U_{\alpha k} \, |\nu_k\rangle \\ &= \sum_{k} e^{-iE_k t} U_{\alpha k} U^*_{\beta k}. \end{aligned} \tag{1.7}$$

At $t = 0$, $e^{-iE_k t} = 1$ and $\sum_k U_{\alpha k} U^*_{\beta k} = \delta_{\alpha\beta}$, so the amplitude is $\langle \nu_\beta | \nu_\alpha(0) \rangle = \delta_{\alpha\beta}$, as expected. At $t > 0$, the probability of finding ν_β in a ν_α beam is the square of the

[3] n is normally taken to be three, to correspond to the number of light flavor neutrinos, but it may be more. $n > 3$ implies the existence of sterile neutrinos that do not participate in the weak nuclear force.

amplitude:

$$\begin{aligned}
P_{\nu_\alpha \to \nu_\beta}(t) &= |\langle \nu_\beta | \nu_\alpha(t) \rangle|^2 \\
&= \langle \nu_\beta | \nu_\alpha(t) \rangle \langle \nu_\beta | \nu_\alpha(t) \rangle^* \\
&= \sum_j e^{-iE_j t} U_{\alpha j} U^*_{\beta j} \sum_k e^{iE_k t} U^*_{\alpha k} U_{\beta k} \\
&= \sum_{j,k} e^{-i(E_j - E_k)t} U_{\alpha j} U^*_{\beta j} U^*_{\alpha k} U_{\beta k} \\
&= \sum_{j,k} e^{-i(E_j - E_k)t} \left| U_{\alpha j} U^*_{\beta j} U^*_{\alpha k} U_{\beta k} \right| e^{i\varphi_{\alpha\beta jk}} \\
&= \sum_{j,k} e^{-i\left[(E_j - E_k)t - \varphi_{\alpha\beta jk}\right]} \left| U_{\alpha j} U^*_{\beta j} U^*_{\alpha k} U_{\beta k} \right| \\
&= \sum_{j,k} \left| U_{\alpha j} U^*_{\beta j} U^*_{\alpha k} U_{\beta k} \right| \cos\left[(E_j - E_k)t - \varphi_{\alpha\beta jk}\right], \qquad (1.8)
\end{aligned}$$

where $\varphi_{\alpha\beta jk} \equiv \arg(U_{\alpha j} U^*_{\beta j} U^*_{\alpha k} U_{\beta k})$. The last step is justified since we know the sum to be real by construction, and can therefore ignore the imaginary parts of the summands.

Now, assuming the masses to be much smaller than the momentum, we can expand the energies of the mass states as:

$$\begin{aligned}
E_k &= \sqrt{P^2 + m_k^2} = P\sqrt{1 + \left(\frac{m_k}{P}\right)^2} \\
&= P\left[1 + \frac{1}{2}\left(\frac{m_k}{P}\right)^2 + \cdots\right] \\
&\simeq P + \frac{m_k^2}{2P}. \qquad (1.9)
\end{aligned}$$

Thus,

$$\begin{aligned}
E_j - E_k &\simeq \left(P + \frac{m_j^2}{2P}\right) - \left(P + \frac{m_k^2}{2P}\right) \\
&= \frac{m_j^2 - m_k^2}{2P} \equiv \frac{\Delta m_{jk}^2}{2P}. \qquad (1.10)
\end{aligned}$$

Also, since the neutrinos are highly relativistic, distance travelled is approximately equal to time:

$$\frac{L}{t} \simeq c = 1 \Longrightarrow L \simeq t. \qquad (1.11)$$

Putting Eqs. 1.8, 1.10, and 1.11 together, we get:

$$\boxed{P_{\nu_\alpha \to \nu_\beta}(t) \simeq \sum_{j,k} \left| U_{\alpha j} U^*_{\beta j} U^*_{\alpha k} U_{\beta k} \right| \cos \left[\frac{\Delta m^2_{jk} L}{2P} - \varphi_{\alpha\beta jk} \right]}. \tag{1.12}$$

Sometimes it is useful to define a characteristic distance scale L_{jk} for $j \to k$ oscillations at momentum P:

$$L_{jk} \equiv \frac{4\pi P}{\Delta m^2_{jk}}. \tag{1.13}$$

Then Eq. 1.12 reads:

$$P_{\nu_\alpha \to \nu_\beta}(t) \simeq \sum_{j,k} \left| U_{\alpha j} U^*_{\beta j} U^*_{\alpha k} U_{\beta k} \right| \cos \left[\frac{2\pi L}{L_{jk}} - \varphi_{\alpha\beta jk} \right]. \tag{1.14}$$

1.3.1.2 Two-family oscillations

If we consider oscillations between only two lepton families, the situation is considerably simpler. The general unitary matrix is real and can be characterized by a single parameter, the mixing angle θ:

$$U = \begin{pmatrix} \cos\theta & -\sin\theta \\ \sin\theta & \cos\theta \end{pmatrix}. \tag{1.15}$$

Since U is real, all values of φ are zero, and Eq. 1.12 becomes:

$$P_{\nu_\alpha \to \nu_\beta}(t) \simeq \sum_{j,k} |U_{\alpha j} U_{\beta j} U_{\alpha k} U_{\beta k}| \cos \frac{\Delta m^2_{jk} L}{2P}. \tag{1.16}$$

If we restrict ourselves to the non-trivial case where $\beta \neq \alpha$, we have:

$$\begin{aligned} P_{\nu_\alpha \to \nu_\beta}(t) &\simeq \sum_{j \neq k} |U_{\alpha j} U_{\beta j} U_{\alpha k} U_{\beta k}| \cos \frac{\Delta m^2_{jk} L}{2P} + \sum_k U^2_{\alpha k} U^2_{\beta k} \\ &= 2 \underbrace{U_{11} U_{12} U_{21} U_{22}}_{-\sin^2\theta \cos^2\theta} \cos \frac{\Delta m^2_{jk} L}{2P} + 2 \sin^2\theta \cos^2\theta \\ &= \underbrace{2 \sin^2\theta \cos^2\theta}_{\frac{1}{2}\sin^2 2\theta} \underbrace{\left(1 - \cos \frac{\Delta m^2_{jk} L}{2P} \right)}_{2 \sin^2 \left(\frac{\Delta m^2_{jk} L}{4P} \right)} \end{aligned}$$

$$\boxed{P_{\nu_\alpha \to \nu_\beta}(t) \simeq \sin^2 2\theta \sin^2\left(\frac{\Delta m^2_{jk} L}{4P}\right)}. \tag{1.17}$$

In laboratory units, and inserting the appropriate factor of $\hbar c$, this is:

$$\boxed{P_{\nu_\alpha \to \nu_\beta}(t) \simeq \sin^2 2\theta \sin^2\left(\frac{1.27\Delta m^2_{jk}(eV^2/c^4) L(m)}{P(MeV/c)}\right)}. \tag{1.18}$$

Thus, for a given experiment, looking at a neutrino beam of momentum P at a distance L from the source, the probability of oscillation is a function of only two parameters. Typically, experiments quote results in terms of the parameters $\sin^2 2\theta$ and Δm^2, by excluding a region of two dimensional phase space (e.g. Fig. 1.11).

1.3.2 Matter oscillations

Wolfenstein pointed out [38] that when travelling through matter, the forward scattering of neutrinos becomes important. The interaction terms in the Hamiltonian lead to changes in the effective mass of particles travelling through a medium. A similar case is that of an electromagnetic wave which travels at c in vacuum but, picking up an effective mass, travels slower in a medium with non-zero index of refraction. Likewise, neutrinos passing through matter gain effective masses through the weak interactions; alternately, the medium can be said to have a "weak index of refraction", which is in general different for each type of neutrino.

1.3.2.1 Neutrino wave equations

Although neutrinos have non-zero spin, for very relativistic neutrinos the spin is irrelevant. The SM weak interaction only couples to the left-handed component of the neutrino field, and since chirality is conserved up to $\mathcal{O}(m/E)$, only the left-handed component need be considered for $m \ll E$. Thus, whether a neutrino is a Dirac or a Majorana particle, neglecting the spin component of the wave equation yields the (spinless) Klein-Gordon equation:

$$(\partial_\mu \partial^\mu + m_k^2)\,|\nu_k\rangle_L = 0. \tag{1.19}$$

For n neutrino states with in general different masses, $|\nu_k\rangle_L$ becomes an n-dimensional column vector Ψ_k and m_k^2 is replaced by an $n \times n$ diagonal matrix, $\mathcal{M}^2$. Leaving the subscript k as a reminder that the elements of Ψ_k are mass eigenstates, this is:

$$(\partial_\mu \partial^\mu + \mathcal{M}^2)\Psi_k = 0. \tag{1.20}$$

1.3.2.2 Propagation in vacuum

If we consider the propagation of mass states with equal momenta p in vacuum, the space derivative yields a common term for all states. The resulting second-order differential equation

$$\frac{\partial^2}{\partial t^2}\Psi_k = (p^2 + \mathcal{M}^2)\Psi_k \tag{1.21}$$

can be solved trivially, yielding two solutions. Ignoring the negative energy solution, we end up with the first-order Schrödinger-like equation:

$$i\frac{\partial}{\partial t}\Psi_k = H\Psi_k, \tag{1.22}$$

where we have used $|\nu_k\rangle_L = \exp(-iE_k t)$. In the mass eigenstate basis, H is diagonal with elements $E_k \equiv \sqrt{m_k^2 + p^2}$.

In the weak eigenstate basis, we can make the simple substitution $H \rightarrow H' = UHU^\dagger$, with U coming from Eq. 1.5:

$$i\frac{\partial}{\partial t}\Psi_\alpha = UHU^\dagger\Psi_\alpha, \tag{1.23}$$

where Ψ_α is the column vector of the weak eigenstates $|\nu_\alpha\rangle$.

For the case of two-neutrino oscillations, U is given by Eq. 1.15 and

$$H' = p + \frac{\Sigma m_{12}^2}{4p} + \frac{\Delta m_{12}^2}{4p}\begin{pmatrix} -\cos 2\theta & \sin 2\theta \\ \sin 2\theta & \cos 2\theta \end{pmatrix}, \tag{1.24}$$

where Δm_{12}^2 is given by Eq. 1.10 and Σm_{12}^2 is defined analogously:

$$\Sigma m_{jk}^2 \equiv m_j^2 + m_k^2. \tag{1.25}$$

1.3.2.3 Propagation in matter

The interaction terms in the Hamiltonian alter the picture somewhat. The neutral current component (Fig. 1.1a) is the same for all active (non-sterile) neutrino flavors. The magnitude of the charged current interaction (Fig. 1.1b) will be greater for ν_e than for ν_μ or ν_τ, though, since the electron density in normal matter is greater than the μ or τ densities, which are negligible.

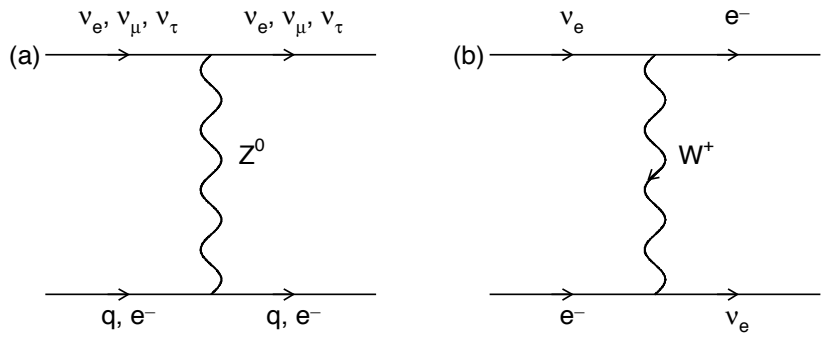

Figure 1.1: a) Neutral current and b) charged current interactions of neutrinos in normal matter. Since normal matter contains almost no μ or τ, the charged current interaction is shown only operating on ν_e.

We can write the interaction Hamiltonian for the charged current reaction as

$$\begin{aligned} H_{CC}^{int} &= \frac{G_F}{\sqrt{2}}\bar{e}\gamma^\mu(1-\gamma_5)\nu_e\overline{\nu_e}\gamma_\mu(1-\gamma_5)e \\ &\quad \text{Fierz reorder} \\ &= \frac{G_F}{\sqrt{2}}\overline{\nu_e}\gamma^\mu(1-\gamma_5)\nu_e\bar{e}\gamma_\mu(1-\gamma_5)e. \end{aligned} \tag{1.26}$$

Averaging the electron part of this gives

$$H_{CC}^{int} = \sqrt{2}G_F\{\overline{\nu_{eL}}\gamma^\mu\nu_{eL}\}\langle\bar{e}\gamma_\mu(1-\gamma_5)e\rangle. \tag{1.27}$$

In the non-relativistic limit, the axial vector part of this picks out spin, but the expectation value of the spin of unpolarized electrons is zero. Likewise, the spatial indices on the vector term describe the electron velocity, but the expectation value is again zero in the reference frame where the matter is at rest. The only non-trivial term in the average is thus $\langle\bar{e}\gamma_0 e\rangle = \langle\bar{e}e\rangle$, which is just the electron number operator N_e. Thus, the CC interaction Hamiltonian modifies the potential of the neutrino by an amount $V_{CC} = \sqrt{2}G_F N_e$.

The neutral current contributions to the Hamiltonian are the same for all active neutrino species. Contributions from interactions with electrons, protons, and neutrons can be summarized by the interaction Hamiltonian

$$H_{NC}^{int} = \sqrt{2}G_F\sum_f n_f\left[I_{3L}^{(f)} - 2\sin^2\theta_W Q^{(f)}\right], \tag{1.28}$$

where $f \in \{e, p, n\}$, Q is the electric charge, and I_3 is the third component of weak

isospin. For electrons and protons the addends are equal and opposite, so in electrically neutral matter their contributions exactly cancel. The only remaining part is an effective potential $V_{NC} = -\sqrt{2}G_F N_n/2$, where N_n is the neutron number operator. [4] This will lead to differences for active-sterile oscillations as the CC interactions do for $\nu_e \to \nu_\alpha$.

These additional potential terms may now be included in the analogue of Eq. 1.23, where H' now becomes

$$H' = UHU^\dagger + V_{CC}|\nu_e\rangle + V_{NC}\sum_{active}|\nu_\alpha\rangle\,. \tag{1.29}$$

Assuming only the two neutrinos ν_e and ν_μ for simplicity, this is

$$H' = p - \frac{\sqrt{2}G_F N_n}{2} + \frac{\Sigma m_{12}^2}{4p} + \frac{1}{4p}\begin{pmatrix} -\Delta m_{12}^2\cos 2\theta + 2\mathcal{A} & \Delta m_{12}^2\sin 2\theta \\ \Delta m_{12}^2\sin 2\theta & \Delta m_{12}^2\cos 2\theta \end{pmatrix}, \tag{1.30}$$

where $\mathcal{A} \equiv 2\sqrt{2}G_F N_e p$. As usual for a 2×2 matrix, the diagonalizing angle, $\tilde{\theta}$, is given by

$$\tan 2\tilde{\theta} = \frac{2H_{12}}{H_{22}-H_{11}} = \frac{\Delta m_{12}^2\sin 2\theta}{\Delta m_{12}^2\cos 2\theta - \mathcal{A}}. \tag{1.31}$$

If $\mathcal{A} = \Delta m_{12}^2\cos 2\theta$, the effective mixing angle goes to $\pi/4$. Thus the effective mixing can be maximal between ν_e and ν_μ in matter, even if the vacuum mixing angle θ is very small. Figure 1.2 shows a plot of $\sin^2 2\tilde{\theta}$ as it goes through its resonance. The half-width of the peak is proportional to $\Delta m_{12}^2\sin 2\theta$.

1.3.2.4 The MSW effect

Consider the form of the effective mixing angle in Eq. 1.31. If we take the limit of $\mathcal{A} \to +\infty$ (or at least $\mathcal{A} \gg \Delta m_{12}^2\cos 2\theta$), $\tan 2\tilde{\theta}$ goes to 0^-, which means that $\tilde{\theta}$ approaches $\pi/2$ as long as it is required to be positive. This represents a state of maximal mixing, where the ν_e is almost entirely made up of the heavier state ν_2, whereas the ν_μ state is almost all ν_1. In the other extreme, where $\mathcal{A} \to 0$, we have the vacuum oscillation parameters, as expected: $\tilde{\theta} \to \theta$. If the vacuum mixing angle is small, then the ν_e state should be mostly ν_1 with the ν_μ being ν_2.

If it is possible to create neutrinos in a region where $\mathcal{A}$ is sufficiently large and propagate those neutrinos out to a near-vacuum region, one would effectively be swapping ν_e for ν_μ and vice versa. For example, suppose the electron density in the Sun were sufficiently high so that ν_e created in nuclear reactions there were composed of mostly

[4] See Sec. 9.3 in reference [40].

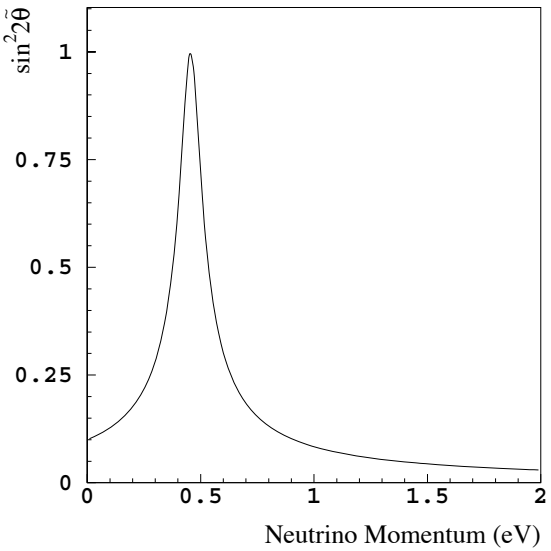

Figure 1.2: The effective mixing angle in matter, $\sin^2 2\tilde{\theta}$ as a function of neutrino momentum, showing the resonant peak. Δm^2_{12} is taken to be 10^{-5} here, $\sin^2 2\theta$ is 10^{-2}, and the electron density is taken to be one mole per cm^3.

ν_2. The ν_2 would then propagate outward into space, where $\mathcal{A} \approx 0$. When these ν_2 reinteract, they would then be mostly ν_μ. This is the essence of the MSW effect, named for Wolfenstein, who first described matter oscillations, and for Mikheyev and Smirnov, who noted [39] that this level-crossing behavior might be important in describing solar neutrino fluxes.

1.3.3 Experimental considerations

One fairly obvious but important caveat about neutrino oscillation experiments is that they do not measure neutrino masses directly; instead, they measure the differences between the squares of masses. This distinction may come into play in discussions of the cosmological significance of neutrino mass. It is commonly assumed that the largest mass difference represents the approximate mass of the heaviest mass neutrino, and that the masses of the other neutrinos are negligible. In this case, the sum of the neutrino masses could be very small; however, the aggregate mass of three neutrinos of nearly degenerate masses may be much larger.

Another point is that a positive result for neutrino oscillations demonstrates neutrino mass, but the inverse does not hold. If the flavor and mass eigenstates are identical or if the masses are truly degenerate, no flavor oscillations will occur.

1.3.3.1 Appearance vs. disappearance experiments

Experiments looking for neutrino oscillation can be categorized as either appearance or disappearance experiments. In the archetypal appearance experiment, one begins with a pure beam of one type of neutrino (of arbitrary flux). Then the detection of any other type of neutrino in this beam is a "smoking gun" signature of neutrino oscillation. In an appearance experiment, only a small fraction of the beam needs to oscillate (or, the beam needs to oscillate with only a small probability) in order to detect the oscillation.

Disappearance experiments must know the flux of the beam precisely. They look for a deficiency in the known flux at their detector. A typical disappearance experiment would be one at a reactor, where the neutrino source is essentially a point. Then, one would perform two measurements of the neutrino flux at two distances from the reactor core. One measurement would measure the flux and, given the solid angles subtended by the two detectors, would also predict the flux at the other. Any deviation from this prediction would signal some sort of loss (or enhancement) of the neutrino beam, possibly from oscillation. This type of experiment with two detectors is called a near-far experiment, for obvious reasons. At an accelerator, a disappearance experiment should be performed with three detectors: two to measure the flux *and divergence* of the beam, and the third to check for deviations from predictions.

Disappearance experiments potentially provide less information about neutrino oscillations than appearance experiments. Since they do not observe the final state, disappearance experiments cannot tell into which flavor a neutrino has oscillated. Because they need to observe a deficiency in the beam, rather than simply see a few events, they are not sensitive to very small oscillation probabilities. Also, apart from oscillations, other perhaps more exotic explanations may account for deficiencies in neutrino beams, examples being neutrino decay [41], flavor-changing interactions [42], transition magnetic moments [43], and inherent neutrino non-orthonormality [44].

1.3.3.2 Experimental sensitivities

From the form of the oscillation amplitude (Eq. 1.7), one notes that no oscillation will occur if the exponential is unity. For the oscillation between two neutrino species (Eq. 1.18), this translates to the following requirement:

$$\Delta m^2(eV^2) \gtrsim \frac{P(MeV/c)}{L(m)}. \tag{1.32}$$

Detecting neutrino oscillations at small values of $\sin^2 2\theta$ is more complicated. As Δm^2 gets large, the second $\sin^2$ term in Eq. 1.17 rapidly oscillates. Averaging this term to $\frac{1}{2}$, we see that the oscillation probability is directly related to the parameter $\sin^2 2\theta$. In order to probe small values of this parameter, then, an experiment must be able to detect small oscillation probabilities. This is in general a complicated function of

Experiment	Events	L (m)	E (MeV)	$\sin^2 2\theta$	$\Delta m^2(eV^2)$
Solar	10^3	10^{11}	10^0	10^{-1}	10^{-11}
Atmospheric	10^3	10^7	10^3	10^{-1}	10^{-4}
Reactor SB	10^5	10^2	10^0	10^{-3}	10^{-2}
Reactor LB	10^3	10^3	10^0	10^{-1}	10^{-3}
Meson Factory	10^3	10^1	10^1	10^{-2}	10^{-1}
Accelerator SB	10^6	10^3	10^3	10^{-4}	10^0
Accelerator LB	10^3	10^6	10^3	10^{-1}	10^{-3}

Table 1.2: Typical neutrino experiment configurations and sensitivities to oscillation parameters. SB=Short-Baseline, LB=Long-Baseline

the analysis, including the detection efficiencies, the number of expected background events, and the confidence level. A naïve estimate is that for an analysis with zero expected background and a 6% detection efficiency for the "wrong type" of neutrino in an otherwise pure beam, then for large Δm^2 oscillations would be detected at the 3σ level for

$$\sin^2 2\theta \gtrsim \frac{100}{N}, \tag{1.33}$$

where N is the total number of CC events detected by the experiment.

Given the guidelines given by Eqs. 1.32 and 1.33, the expected sensitivities of different types of experiments can be estimated. Table 1.2 gives an order of magnitude listing for different types of experiments.

1.4 Experimental Evidence for Oscillation

Many experiments have searched for evidence of neutrino oscillations. This section will examine some of the experiments that have been done, and quote their results.

This section is organized into five subsections, grouping experiments according to neutrino production. This grouping also roughly correlates with increasing Δm^2, although there is some overlap. Those experiments capable of detecting the very low energy (<10 MeV) neutrinos from the Sun are in the first section. Experiments to detect the ν_e and ν_μ flux coming from cosmic rays in the earth's atmosphere are grouped in the next section. Next are the detectors designed to observe the $\overline{\nu}_e$ flux emitted by nuclear reactors. Medium energy proton accelerators can produce large amounts of ν_e, $\overline{\nu}_\mu$, and ν_μ, and oscillation searches at such meson factories are considered together. Finally, high energy accelerators can produce beams of neutrinos from meson decays-in-flight, and these are considered in the last subsection. Some experiments

Source	Reaction	$\langle E_\nu \rangle$ (MeV)	Max. E_ν (MeV)
pp	$p + p \rightarrow d + e^+ + \nu_e$	0.2668	0.423 ± 0.030
pep	$p + e^- + p \rightarrow d + \nu_e$	1.445	1.445
^{7}Be	$e^- + {}^7\mathrm{Be} \rightarrow {}^7\mathrm{Li} + \nu_e$	0.3855, 0.8631	0.3855, 0.8631
^{8}B	$^8\mathrm{B} \rightarrow {}^8\mathrm{Be} + e^+ + \nu_e$	6.735 ± 0.036	~ 15
Hep	$^3\mathrm{He} + p \rightarrow {}^4\mathrm{He} + e^+ + \nu_e$	9.628	18.778
^{13}N	$^{13}\mathrm{N} \rightarrow {}^{13}\mathrm{C} + e^+ + \nu_e$	0.7063	1.1982 ± 0.0003
^{15}O	$^{15}\mathrm{O} \rightarrow {}^{15}\mathrm{N} + e^+ + \nu_e$	0.9964	1.7317 ± 0.0005
^{17}F	$^{17}\mathrm{F} \rightarrow {}^{17}\mathrm{O} + e^+ + \nu_e$	0.9977	1.7364 ± 0.0003

Table 1.3: Solar neutrino sources and energies. Values obtained from Ref. [46].

(KamLAND, e.g.) are sensitive to neutrinos from more than one type of source, and they are mentioned in all relevant subsections.

1.4.1 Solar neutrinos

In addition to electromagnetic energy, the Sun emits about 2% of its radiation in the form of electron neutrinos. At the earth's surface, the flux should be roughly $6.5 \times 10^{10}/\mathrm{cm}^2/\mathrm{sec}$. These neutrinos come from several nuclear reactions inside the Sun, which can be grouped into one of two families: the pp cycle (Fig. 1.3) and the CNO cycle (Fig. 1.4). The energy distributions and fluxes of these neutrinos (Fig. 1.5, Tab. 1.3) can be calculated within the framework of the Standard Solar Model (SSM) [45].

Because of the extremely low energies of the ν_e's from the Sun, only disappearance experiments are performed; the neutrinos are below the energy threshold for μ or τ creation in CC interactions. Near-far experiments are impractical, so the measured ν_e flux at the earth is compared to the theoretical predictions.

The first measurement of solar neutrinos at the Homestake gold mine in the 1960's showed [47] that the measured flux was significantly less than theory predicted. The Homestake detector is a large underground tank of tetrachloroethylene ($Cl_2C{=}C\,Cl_2$), and solar neutrinos are detected through the process

$$\nu_e + \mathrm{Cl}^{37} \rightarrow e^- + \mathrm{Ar}^{37}, \tag{1.34}$$

where the (radioactive) argon atoms are counted as they decay. Since the photons we see come only from the outer layer of the Sun, the Homestake experiment was designed to use neutrinos to probe the Sun's inner structure. After the initial results became available, however, the focus changed towards the study of the properties of the neutrinos

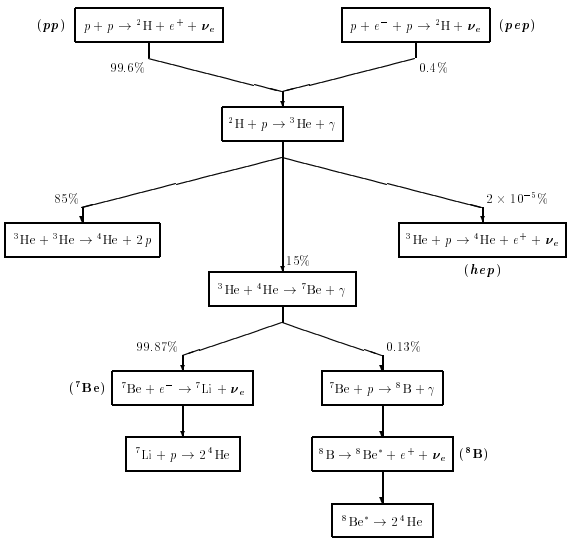

Figure 1.3: The pp cycle. Figure reprinted from Ref. [46].

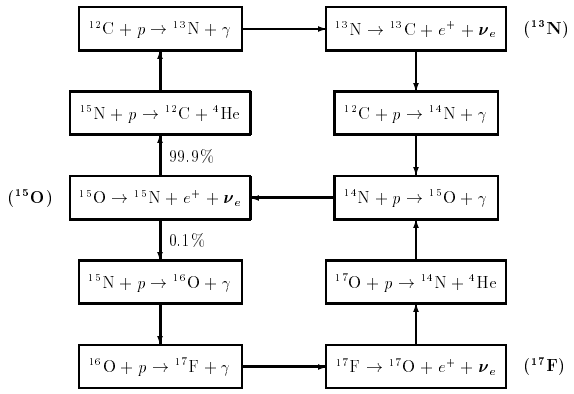

Figure 1.4: The CNO cycle. Figure reprinted from Ref. [46].

themselves. Improvements in the SSM and in the experimental measurements have only made the discrepancy more stark, so further experiments were devised.

Since the chlorine ν_e capture process of Eq. 1.34 has a threshold of around 850 keV, the Homestake detector is not sensitive to the plentiful but low-energy pp neutrinos (see Fig. 1.5). In order to take advantage of these neutrinos two experiments were designed using gallium as a target. Gallium undergoes the equivalent process to Eq. 1.34:

$$\nu_e + \mathrm{Ga}^{71} \rightarrow e^- + \mathrm{Ge}^{71} \tag{1.35}$$

with an energy threshold of 233 keV, and the germanium is detected through its subsequent decay. The SAGE [48] detector, located underground in Russia's Baksan Neutrino Observatory, consists of fifty-five tons of liquid gallium metal, whereas the

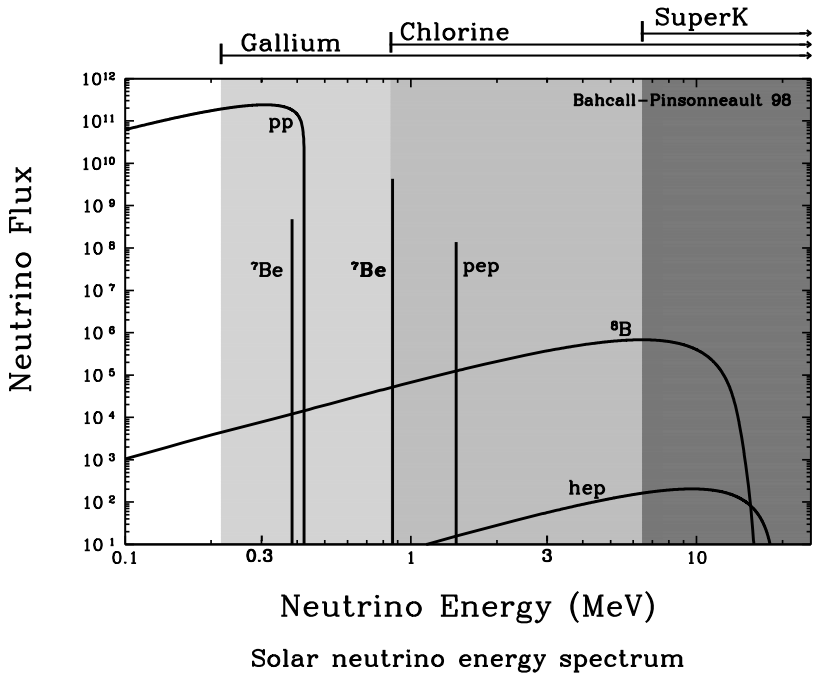

Figure 1.5: Estimated energy distributions for solar neutrinos in the SSM, showing the sensitivities of different types of detectors.

GALLEX [49] experiment uses a solution of gallium chloride.

In addition to the radiochemical detectors, Kamiokande [50] and its successor Super-Kamiokande [51] are water Cherenkov detectors, used for both solar and atmospheric neutrino studies. The targets are purified water, and light emitted inside the targets is detected in large arrays of photomultipliers. These detectors are sensitive to the Cherenkov light emitted by a recoil electron from a solar neutrino elastic scattering event as the electron traverses the detector. [5] Although only sensitive to the relatively high energy ^{8}B and hep neutrinos (see Fig. 1.5), the water Cherenkov detectors give more information about the neutrino capture events. They can measure the direction of the recoil electron, showing that the neutrinos come from the Sun, they can measure the time dependence of the neutrino events (day vs. night, e.g.), and they can measure the energy of the recoil electrons.

The results of all these experiments are consistent with each other and inconsistent with the SSM. Table 1.4 lists the SSM predictions and the experimental results.

These results can be interpreted in a number of ways. If neutrino oscillations are used to account for the difference between experiment and theory, one may define pre-

[5] For the higher energy atmospheric neutrinos, both electrons (from ν_e CC events) and muons (from ν_μ CC events) can be identified by their individual Cherenkov light signatures.

Experiment	Type	SSM Prediction	Measured	$\frac{\text{Exp}}{\text{SSM}}$
Homestake	Cl	$9.3^{+1.2}_{-1.4}$	$2.55 \pm 0.14 \pm 0.14$	0.273 ± 0.021
SAGE	Ga	137^{+8}_{-7}	$69 \pm 10^{+5}_{-7}$	0.504 ± 0.089
GALLEX			$69.7 \pm 6.7^{+3.9}_{-4.5}$	0.509 ± 0.059
Combined			69.5 ± 6.7	0.507 ± 0.049
Kamiokande	H_2O	$6.62^{+0.93}_{-1.12}$	$2.80 \pm 0.19 \pm 0.33$	0.423 ± 0.058
Super-K			$2.51^{+0.14}_{-0.13} \pm 0.18$	0.379 ± 0.034
Combined			2.586 ± 0.195	0.391 ± 0.029

Table 1.4: Solar neutrino fluxes and the SSM predictions. Units are SNU (1 Solar Neutrino Unit (SNU) = 10^{-36} interactions per target atom per second) for the radiochemical experiments and $10^6 \text{cm}^{-2}\text{sec}^{-1}$ for the water Cherenkov experiments. Values obtained from Ref. [52].

ferred regions in a $\sin^2 2\theta$ vs. Δm^2 plot, and several of these may be drawn depending on which type of oscillation is used. Assuming MSW oscillations in the Sun ($\nu_e \rightarrow \nu_\mu$ or $\nu_e \rightarrow \nu_\tau$), two distinct regions of phase space may be allowed: the small and large mixing angle solutions. (See Fig. 1.6.) Also possible are MSW ν_e-sterile oscillations and vacuum oscillations, shown in Fig. 1.7.

In addition to the experiments which have already produced results, there are several experiments which may provide more insight into the solar neutrino deficit in the near future. The Sudbury Neutrino Observatory (SNO) experiment [53], which is currently taking data, uses a heavy-water (D_2O) Cherenkov detector to observe both NC and CC events. This should provide information on both the flux of ν_e and the flux of *all* non-sterile neutrinos crossing the detector, which should determine whether the oscillations are active-active or active-sterile. The ICARUS experiment [54], scheduled for installation in the Gran Sasso Laboratory in Italy in 2000, will use a large liquid argon time projection chamber (TPC), and it should have similar detection capabilities to SNO.

Borexino[6] [55] and KamLAND[7] [56] use liquid scintillators and should be able to combine the time and directional capabilities of a water Cherenkov detector like

[6]The Borexino collaboration successfully built and operated a prototype of their detector from 1994–1996, and construction is now under way on the full-scale detector in Hall C of the Gran Sasso Laboratory, with an expected completion date of 2001. The neutrino sensitivity is expected to reach down to 250 keV.

[7]The Kamioka Liquid scintillator Anti-Neutrino Detector (KamLAND) is a dual-purpose neutrino detector currently under construction in Japan. It it scheduled to begin taking data in 2001, and will observe both solar neutrinos and reactor neutrinos.

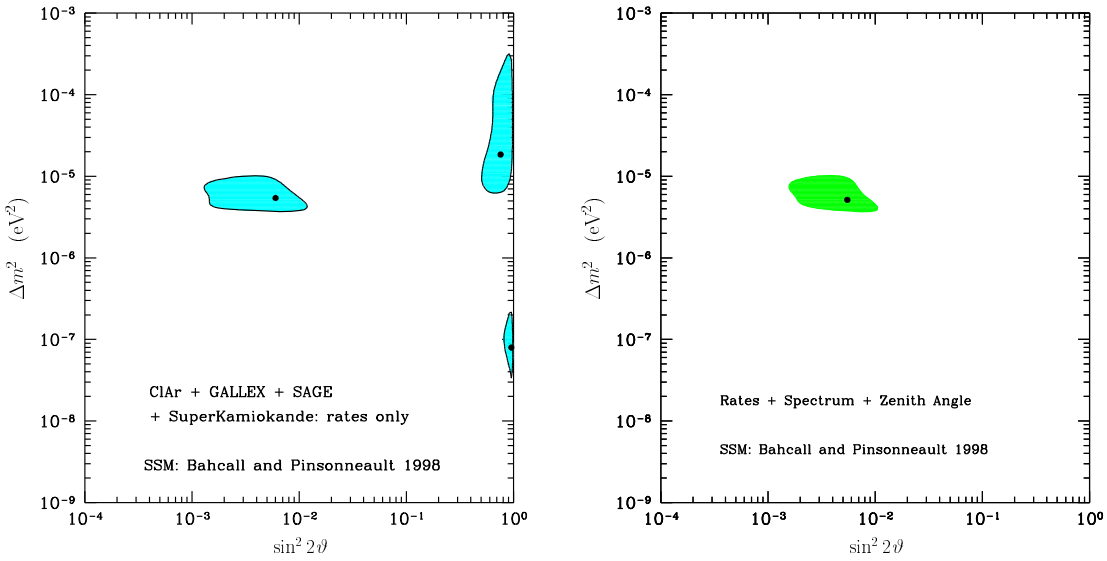

Figure 1.6: Favored phase space regions for solar MSW oscillations. Shadowed regions represent the 99% confidence regions. Results of a fit to data from Tab. 1.4, taken from Ref. [46]. The left plot uses the neutrino rates only, the right plot also uses energy spectrum and zenith-angle distributions from the Super-Kamiokande experiment.

Kamiokande with the low energy threshold of the gallium experiments. Both experiments claim to be sensitive to pp neutrinos.

Future proposed experiments include the liquid scintillator LENS experiment at Gran Sasso; HELLAZ [57], which will use a helium gas TPC for tracking, also at Gran Sasso; and HERON, which proposes to use a ~10 ton target of superfluid helium. These experiments also purport to measure the pp solar neutrino spectrum.

1.4.2 Atmospheric neutrinos

Cosmic rays incident on the upper atmosphere of the earth produce particle showers containing large amounts of charged pions. These pions decay through the chain

$$\begin{aligned} \pi^+ &\rightarrow \mu^+ \nu_\mu \\ &\hookrightarrow e^+ \nu_e \overline{\nu}_\mu \end{aligned} \tag{1.36}$$

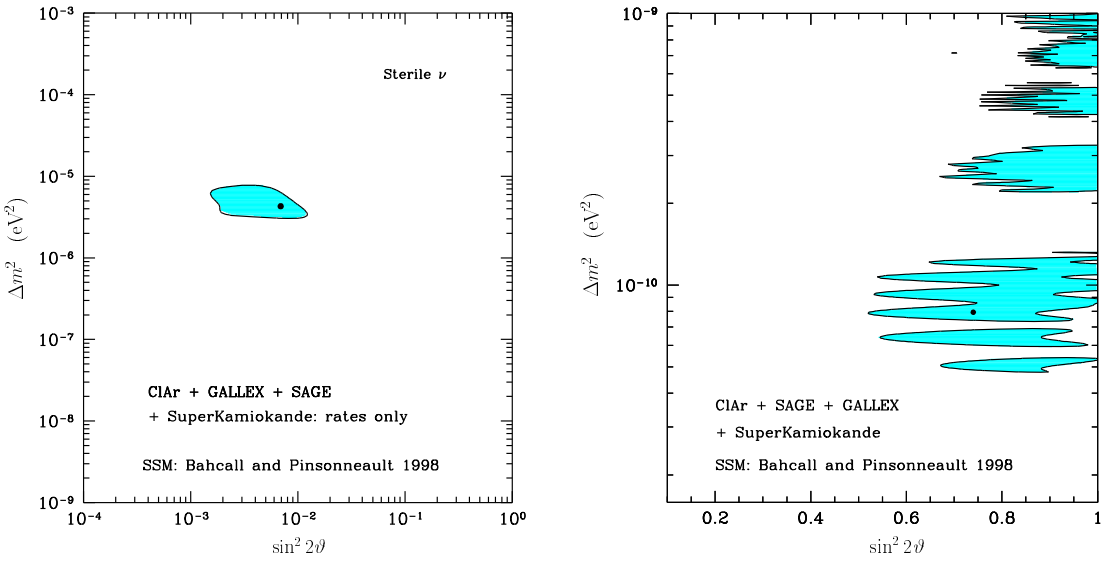

Figure 1.7: Favored phase space regions for solar neutrino oscillations. Shadowed regions are the 99% confidence regions. Left plot shows MSW active-sterile oscillation parameters, right plot shows vacuum oscillation parameters. Plots taken from Ref. [46].

and its charge conjugate equivalent. At the surface of the earth, therefore, there are approximately twice as many ν_μ as ν_e.[8] The flux at the earth's surface is approximately $1/\mathrm{cm}^2/\mathrm{sec}$. Although the absolute fluxes of the neutrinos can only be calculated with a certainty of 20%, the ratio ν_μ/ν_e can be predicted [58] to better than 5%. In order to cancel systematic uncertainties, experiments normally report the ratio of ratios:

$$\mathcal{R} \equiv \frac{(\nu_\mu/\nu_e)_{\mathrm{exp}}}{(\nu_\mu/\nu_e)_{\mathrm{MC}}}. \tag{1.37}$$

If neutrinos oscillate, then measurements of $\mathcal{R}$ should produce values different from unity. If ν_e oscillate into any other species, there will be a deficit of ν_e and $\mathcal{R}$ will be greater than one. Likewise, if ν_μ oscillate into another species, $\mathcal{R}$ will be less than one. There are other explanations for a non-unit $\mathcal{R}$, however. As in the case of solar neutrinos, neutrino decay [59] and FCNC [60] have been proposed as viable solutions to an atmospheric anomaly.

In addition to the ratio $\mathcal{R}$, experiments that can distinguish upward-going from downward-going neutrinos have another handle on neutrino oscillations. Neutrinos originating directly above the detector travel downward about 10 km through the at-

[8] At neutrino energies greater than 3 GeV the ratio of ν_μ to ν_e increases since higher energy muons may not decay before they reach the earth.

mosphere and earth's crust. Since the upward-going neutrinos must travel though the entire earth before reaching the detector, their path lengths are correspondingly longer, up to 13 000 km. If the oscillation length is on the same scale as this difference, the data should show a corresponding flux anomaly.

Atmospheric neutrino detectors are usually located in deep underground halls in order to filter out the associated atmospheric muons. The first experiments to record atmospheric neutrino interactions were performed in the 1960's in India [62] and South Africa [61], but they lacked the statistics to perform an accurate flux measurement. In the 1980's several new experiments began recording atmospheric neutrino fluxes in earnest, and in 1986 the first suggestion [63] of a non-unit $\mathcal{R}$ was found by the IMB collaboration.

In the 1980's several detectors were built to look for proton decay, but they were also sensitive to atmospheric neutrinos. The IMB [64] and Kamiokande [65] experiments used water Cherenkov detectors, and they measured a ratio $\mathcal{R}$ significantly less than one. (See Tab. 1.5.) NUSEX and Fréjus [66] were fine-grained iron plate calorimeter detectors, and both measured $\mathcal{R} \sim 1$. Both types of detectors were sensitive to the lepton type (e or μ only), and to its direction (and hence to the direction of the incident neutrino); but neither were sensitive to the lepton charge, so they could not distinguish between ν_μ and $\overline{\nu}_\mu$ events.

Because of the discrepancy in the measured value of $\mathcal{R}$, and especially because the discrepancy seemed to correlate with detector type, two more sensitive detectors were built. Super-Kamiokande was a larger water Cherenkov detector built in the same Kamioka mine in Japan as the earlier Kamiokande detector, and Soudan-2 was an iron-plate calorimeter built in the Soudan mine in northern Minnesota. These newer experiments agreed with each other and with the earlier water Cherenkov measurements. In fact, because of their relatively poor precision, the early calorimeter results only differ by 1–2 standard deviations. Table 1.5 shows the results for the ratio $\mathcal{R}$ obtained by all six experiments.

First Kamiokande and now also Super-Kamiokande have also found more evidence to support the hypothesis of neutrino oscillations in the angular dependence of their atmospheric neutrino data. For a given solid angle, the flux entering from the antipodes should be equal. The flux from above comes from a surface area in the atmosphere that is smaller than that from below by a factor L^2, but the flux from below is decreased by the same relative amount because of dispersion. However, Kamiokande found [71] a slight zenith angle dependence in their multi-GeV ν_μ sample, and Super-Kamiokande, with much better statistics, found [73] a more pronounced dependence in both the sub- and multi-GeV samples. (See Fig. 1.8.)

Another way to view the Super-Kamiokande oscillation evidence is to plot the ratio of data to Monte Carlo as a function of the variable L/E_ν. From Eq. 1.17 or 1.18 one can see that the oscillation probability should vary directly with the square of L/E_ν for small Δm^2, and the ratio of data to Monte Carlo would just be $1 - P$. Super-Kamiokande can

Experiment	Type	$\mathcal{R}$
IMB [67]	H_2O	$0.54 \pm 0.05 \pm 0.11$
Fréjus [68]	Fe Cal.	$1.00 \pm 0.15 \pm 0.08$
NUSEX [69]	Fe Cal.	$0.96^{+0.32}_{-0.28}$
Soudan-2 [70]	Fe Cal.	$0.61 \pm 0.15 \pm 0.05$
Kamiokande [71]	H_2O	$0.60^{+0.07}_{-0.06} \pm 0.05$
(multi-GeV [72])		$0.57^{+0.08}_{-0.07} \pm 0.07$
Super-Kamiokande [73]	H_2O	$0.63 \pm 0.03 \pm 0.05$
(multi-GeV [73])		$0.65 \pm 0.05 \pm 0.08$

Table 1.5: Results on the ratio $\mathcal{R}$ for the different atmospheric neutrino experiments to date. The two results given for Kamiokande and Super-Kamiokande represent the sub-GeV and multi-GeV events, respectively.

Oscillation	$\sin^2 2\theta$	Δm^2 (eV^2)	χ^2	d.o.f.
$\nu_\mu \rightarrow \nu_\tau$	1	3.5×10^{-3}	6.21	6.7
$\nu_\mu \rightarrow \nu_s$	1	4.5×10^{-3}	64.3	67

Table 1.6: Best-fit values for the oscillation parameters Δm^2 and $\sin^2 2\theta$ from the up-down asymmetry in the Super-Kamiokande data. Reprinted from Ref. [77].

estimate the neutrino energy by measuring the outgoing lepton's energy, and they can estimate the distance travelled, L, by the correlation between L and neutrino direction. Figure 1.9 shows the results from the Super-Kamiokande fully contained μ and e event samples.

The fact that the electron spectrum is not distorted suggests that ν_μ is not oscillating into ν_e. The long-baseline reactor experiment CHOOZ has been able to verify [76] this in the relevant region of phase-space. This leaves $\nu_\mu \rightarrow \nu_\tau$ and $\nu_\mu \rightarrow \nu_s$ as the only possible oscillation solutions to the Super-Kamiokande data. The best-fit parameters for their data are summarized in Tab. 1.6.

1.4.3 Reactor neutrinos

Nuclear reactors produce copious amounts of $\overline{\nu}_e$ in β-decay reactions inside their cores. Because of the large fluxes, reactor experiments were the first to probe small values

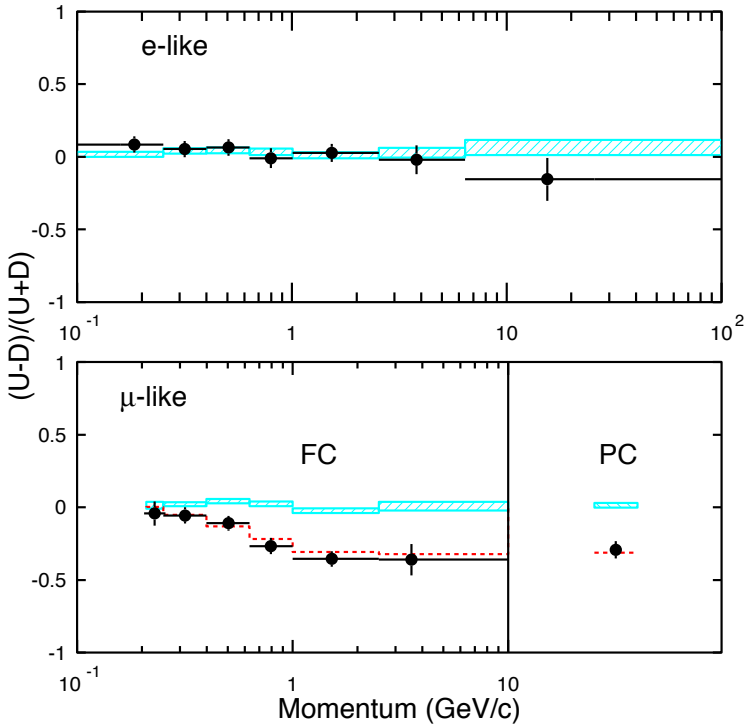

Figure 1.8: Super-kamiokande up-down asymmetry. The hatched regions show the Monte Carlo-predicted 1σ confidence intervals for the assumption of no oscillations. The dashed line is the expected value for $\nu_\mu \rightarrow \nu_\tau$ oscillations with $\Delta m^2 = 3.5 \times 10^{-3} \mathrm{eV}^2$ and $\sin^2 2\theta = 1$. Figure reprinted from Ref. [74].

of $\sin^2 2\theta$; however, because the neutrinos are produced essentially isotropically, the detectors were usually located near the reactor core (short-baseline). Because of the low $\overline{\nu}_e$ energies, reactor oscillation experiments are run in disappearance mode; thus, they are sensitive to $\overline{\nu}_e \rightarrow \nu_x$ oscillations only.

The three short-baseline reactor experiments Bugey [78], Gösgen [79], and Krasnoyarsk [80], did not find evidence of neutrino oscillations. The evidence from atmospheric and solar neutrino experiments suggested that the Δm^2 values were too high in these experiments, so long-baseline reactor experiments were proposed.

Long-baseline reactor experiments need high neutrino fluxes (high power reactors), so they generally take place at commercial power reactors instead of research reactors. The CHOOZ experiment [76] in France uses the neutrinos from two reactors located 1.0 km away, and the Palo Verde experiment [81] in California uses three reactors located 0.8 km away. These two experiments each use a Gadolinium-doped liquid scintillator for detection, and are sensitive to similar regions of phase-space. They have already excluded the possibility of $\nu_\mu \rightarrow \nu_e$ as an explanation of the atmospheric neutrino results.

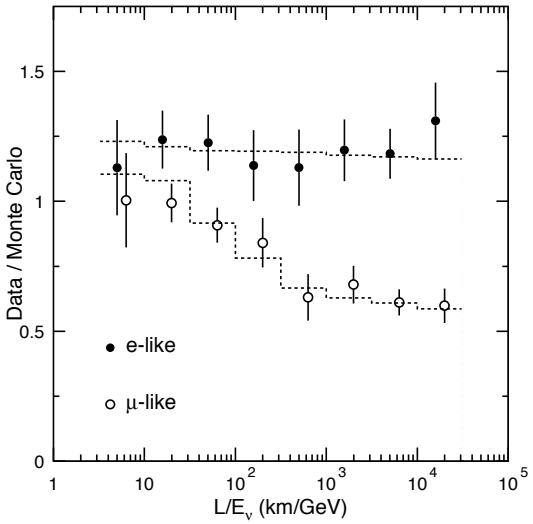

Figure 1.9: L/E_ν for Super-Kamiokande fully contained events. The ratio of data to Monte Carlo in the assumption of no neutrino oscillations is shown for both e and μ events. Figure taken from Ref. [75].

Another future long-baseline reactor experiment, KamLAND [56], may be able to probe one of the solar neutrino MSW regions. This experiment will use the Kamioka site in Japan to house its 1000 ton mineral oil liquid scintillator, and will be sensitive to neutrinos coming from 5 separate nuclear power plants at varying distances away (140 to 215 km). KamLAND is scheduled to begin data taking in 2001. Fig. 1.10 shows the projected sensitivity for KamLAND after three years of data, along with the preliminary results from the other two long-baseline reactor experiments.

1.4.4 Meson factories

Meson factories use medium energy accelerators to produce ν_μ and $\overline{\nu}_\mu$ at energies in the 10's of MeV's. Pions are typically produced in proton beam dumps, and these decay at rest via the chain in Eq. 1.36 to produce the neutrinos. Since they are at rest, the energy of the ν_μ is 30 MeV, and the energies of the ν_e and $\overline{\nu}_\mu$ are broadly distributed with a maximum energy of 53 MeV. All three neutrino species are produced with approximately the same abundances.

Since the only anti-neutrinos produced this way are $\overline{\nu}_\mu$, experiments can look for an oscillation signal through the appearance of $\overline{\nu}_e$. $\overline{\nu}_e$ interacts via the CC reaction

$$\overline{\nu}_e + p \rightarrow e^+ + n, \tag{1.38}$$

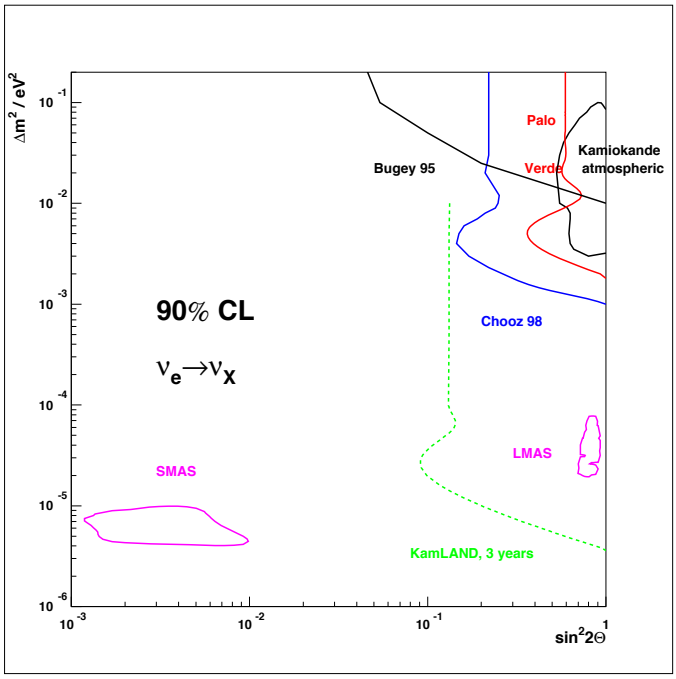

Figure 1.10: Results of the reactor experiments described in the text. Preliminary results from CHOOZ and Palo Verde already cover the region allowed by Kamiokande, and KamLAND is expected to cover the large angle MSW solar solution. Figure taken from Ref. [82].

where the neutron is subsequently captured, emitting a characteristic 2.2 MeV photon. The spatial and temporal coincidence of the positron with the 2.2 MeV γ represents a clean signal for $\overline{\nu}_\mu \rightarrow \overline{\nu}_e$ oscillation.

Some of the pions (~3.4% in LSND, see below) decay in flight, producing higher energy ν_μ. These can interact with carbon in the detector to produce a single electron:

$$\nu_e + {}^{12}\mathrm{C} \rightarrow e^- + \mathrm{X}. \tag{1.39}$$

The ν_e background from μ decay-in-flight is suppressed by the muon's longer lifetime, and the energy spectrum is softer due to the three-body decay; the background from $\pi^+ \rightarrow e^+ + \nu_e$ is suppressed due to the small branching fraction (10^{-4}); and the ν_e background from muon decay-at-rest lies entirely below the kinematic endpoint of 53 MeV. So, the detection of a single electron with energy above about 60 MeV represents a low background candidate for $\nu_\mu \rightarrow \nu_e$ oscillation.

The Large Scintillator Neutrino Detector (LSND) [83, 84] at Los Alamos and the KArlsruhe Rutherford Medium Energy Neutrino (KARMEN) experiment [85] in England are two meson factory neutrino experiments with similar sensitivities. Both use

neutrinos produced in the beam dumps of 800 MeV proton beams, both detectors are liquid scintillators, and neither is sensitive to the charge of the lepton.

LSND has reported evidence for $\nu_\mu \rightarrow \nu_e$ oscillations in two different channels. First, they reported [83] an excess of $\overline{\nu}_e$ events, in which the positron and photon from neutron capture were correlated in space and time in their detector. Second, they observed [84] an excess of ν_e events, in which the electron had energies in the range 60–200 MeV. The favored regions of phase-space from the LSND results are given in Fig. 1.11.

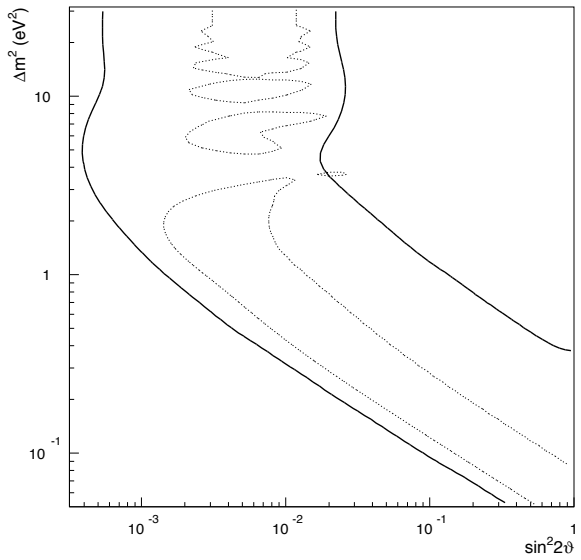

Figure 1.11: Allowed regions for $\nu_\mu(\overline{\nu}_\mu) \rightarrow \nu_e(\overline{\nu}_e)$ from the LSND experiment. The region between the solid lines is allowed at 95% for $\nu_\mu \rightarrow \nu_e$ from the π^+ decay-in-flight analysis. The regions enclosed by dotted lines are allowed at 99% for $\overline{\nu}_\mu \rightarrow \overline{\nu}_e$ from the μ^+ decay-at-rest analysis. Figure reprinted from Ref. [46].

The KARMEN experiment has not confirmed the LSND result. Using a similar detector and similar analysis techniques, they see no anomalous events. The sensitivity of the KARMEN experiment is not quite identical to LSND's[9] so it is not able to rule out the entire allowed region. Fig. 1.12 shows the LSND allowed region along with various exclusion curves, including the latest KARMEN results. One can see a small allowed region below about 1 eV^2 which is not excluded by any experiment.

At least one future experiment has been approved to test the LSND result with much higher sensitivity. The Booster Neutrino Experiment (BooNE) [87] at Fermilab will be-

[9]The KARMEN detector has a shorter baseline (18 meters as opposed to about 30 m for LSND), and until a detector upgrade in 1996 it had a problem with cosmic ray backgrounds. It is projected to achieve comparable sensitivity to LSND in one or two years [86].

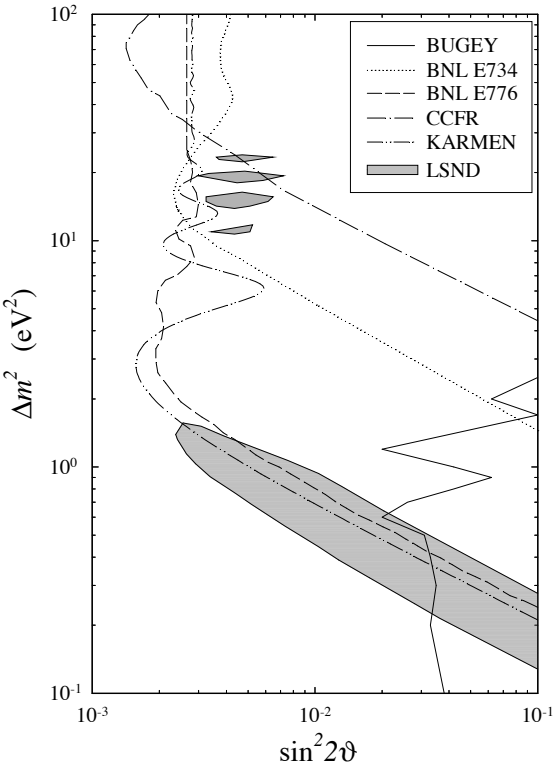

Figure 1.12: LSND 90% CL allowed regions (shaded) superimposed on the exclusion curves from other experiments. The KARMEN exclusion curve is derived from their Bayesian analysis. Plot taken from Ref. [46].

gin data-taking in 2001 using protons from the 8 GeV booster to produce the neutrinos. Other experiments with similar goals have been proposed at CERN (I-216 [88]), Oak Ridge (ORLaND [89]), and at the future European Spallation Source (NESS [90]). Clearly, the evidence is far from conclusive one way or the other.

1.4.5 Accelerators

Neutrino oscillation searches at accelerators are similar to the decay-in-flight analyses of meson factories. Proton beams from high energy accelerators are focused onto a target, from which secondary meson beams (mostly π and K) emerge. The secondary beam can be momentum-selected and/or focused by beamline magnets, after which it is allowed to decay in a dedicated (usually evacuated) volume. The beam remnants and the decay muons are then absorbed and/or swept out by a magnetic field, so that at the detector only a (somewhat diffuse) beam of neutrinos remains.

The important secondary mesons and their decays are listed in Tab. 1.7. The most important are the pion and kaon decays. Muons are mainly produced in pion and kaon

ν_μ			ν_e		
Decay	Br%	$c\tau$ (m)	Decay	Br%	$c\tau$ (m)
$\pi^+ \to \mu^+\nu_\mu$	99.99	7.8	$K^+ \to \pi^0 e^+\nu_e$	4.82	3.7
$K^+ \to \mu^+\nu_\mu$	63.51	3.7	$K^0_L \to \pi^- e^+\nu_e$	38.78	15.5
$K^+ \to \pi^0\mu^+\nu_\mu$	3.18	3.7	$\mu^+ \to e^+\nu_e\overline{\nu}_\mu$	100.	658.
$K^0_L \to \pi^-\mu^+\nu_\mu$	27.17	15.5			
$\mu^- \to e^-\overline{\nu}_e\nu_\mu$	100.	658.			

Table 1.7: Secondary decays that are important for neutrino production in accelerator experiments. $\overline{\nu}_\mu$ and $\overline{\nu}_e$ are produced from the charge conjugate reactions.

decays, so their production point is further down the beamline than the others. This, along with the long lifetime of the muons and the fact that they undergo three-body decay, suppresses the contribution of ν_e in the beam. Furthermore, if a positively charged secondary beam is selected, the $\overline{\nu}_\mu$ (from π^- and K^-) is also reduced. Thus, one can generate a ~90% pure ν_μ beam. More importantly for $\nu_\mu \to \nu_\tau$ oscillation searches, the neutrino beam in an accelerator-based experiment contains practically no ν_τ.

The advantage of accelerators is the ability to control the production and detection of the neutrinos. Both the distance L and the momentum P (cf. Eq. 1.18) can be controlled somewhat in order to probe specific regions of phase space. To get better precision, the neutrino energy spectrum and production point can be modeled in a Monte Carlo beamline simulation.

Accelerator experiments tend to fall into one of two categories. Fine-grained detectors with high spatial resolution are needed to distinguish the τ decay vertex in $\nu_\mu \to \nu_\tau$ appearance searches. Examples of this type of experiment are FNAL-E531 (emulsion) [91], CHARM-II (bubble chamber) [92], and CHORUS (emulsion) [93]. Massive calorimeters have a higher neutrino interaction cross section, and they only need to distinguish between electrons and muons for $\nu_\mu \to \nu_e$ searches. Examples of this type are the Brookhaven experiments BNL-E734 [94] and BNL-E776 [95], CDHS [96] at CERN, and CCFR/NuTeV [97] at Fermilab.

The NOMAD detector [98] at CERN has elements of both categories. It is a multipurpose, fine-grained, low density electronic detector with good momentum resolution and electron identification capabilities. Although it cannot resolve the decay vertex directly, it can identify τ via kinematic considerations. Because of its momentum resolution and particle identification, it is also able to make a sensitive $\nu_\mu \to \nu_e$ search.

None of these accelerator experiments has observed any evidence for neutrino oscillations. The exclusion plot for $\nu_\mu \to \nu_\tau$ is shown in Fig. 1.13.

If the correct interpretation of the atmospheric neutrino data (cf. Sec. 1.4.2) is as

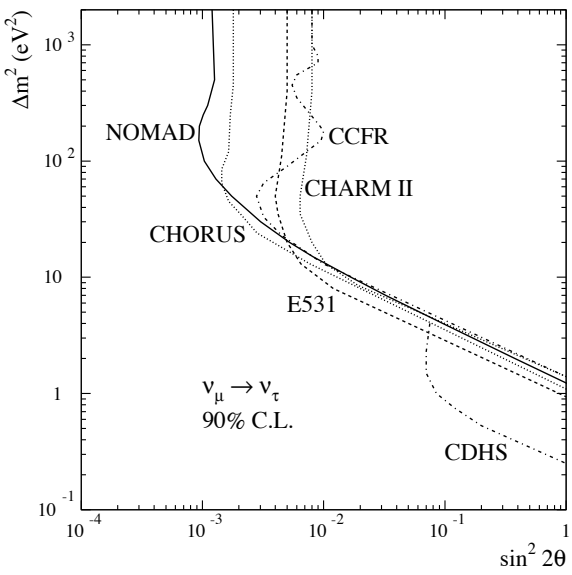

Figure 1.13: Exclusion plot for $\nu_\mu \rightarrow \nu_\tau$ oscillations, derived from accelerator-based neutrino experiments. Figure taken from Ref. [99]. Note that CHORUS has since updated their results [100] to be equivalent with NOMAD's.

evidence for $\nu_\mu \rightarrow \nu_\tau$ oscillations, then the current accelerator-based experiments will not be sensitive to them. The ratio L/P for these experiments is too small (cf. Eq. 1.32) to probe the small Δm^2 suggested by Super-Kamiokande. In order to explore this region, several long-baseline accelerator-based experiments have been proposed.

The first experiment to begin taking data is the K2K experiment [101] in Japan. It is examining a 1–2 GeV beam from KEK in the Super-Kamiokande detector, 235 km away. K2K will also include a 1 kton water Cherenkov "near detector" to measure the neutrino spectrum about 1 km from the KEK beam dump. Because of the low beam energy, the neutrinos will be below threshold for τ production; thus, K2K will only be able to perform ν_μ disappearance and $\nu_\mu \rightarrow \nu_e$ appearance analyses. Data-taking began in March 1999, and it is expected to be sensitive to $\Delta m^2 \gtrsim 2 \times 10^{-3}\text{eV}^2$.

The MINOS experiment [102] will detect neutrinos produced by Fermilab's Main Injector at one detector on-site at Fermilab and another 730 km away at the Soudan mine in northern Minnesota. The neutrinos will have an average energy of ~10 GeV, so $\nu_\mu \rightarrow \nu_\tau$ appearance searches are possible with a sensitivity of $\Delta m^2 \gtrsim 10^{-3}\text{eV}^2$. MINOS will also be sensitive to $\nu_\mu \rightarrow \nu_e$ and $\nu_\mu \rightarrow \nu_s$ oscillations, the latter being evidenced by a deficit in the NC/CC ratio. MINOS is scheduled to begin taking data in 2003.

There are several proposals [103, 104, 105, 106] for experiments using a neutrino beam from CERN near Geneva to the Gran Sasso laboratory in Italy, a distance of about 730 km. Of these, ICARUS is the first to win approval, and it is slated to begin in 2000.

ICARUS will initially feature a 0.6 kton liquid argon detector, and will be expanded up to an eventual fiducial mass of 2.4 kton. The neutrino beam energy is expected to be ~25 GeV, and its sensitivity should be equivalent to MINOS'.

1.5 The Case for NOMAD

An accelerator-based experiment like NOMAD is most sensitive to $\nu_\mu \rightarrow \nu_\tau$ oscillations occurring in the region of very low $\sin^2 2\theta$ ($\gtrsim 10^{-4}$) and relatively high Δm^2 ($\gtrsim 1$ eV^2/c^4) compared to other types of neutrino oscillation experiments. Why is this an interesting region in which to search for oscillations?

There seems to be a profound symmetry between the quarks and leptons: both come in three families with similar mass hierarchies, the electric charges are closely related, etc. It seems natural to presume based on this symmetry that if the leptons' mass and weak eigenstates mix as they do in the quark sector their mixing angles might also be similar. The quark mixing angles are described by the CKM matrix, with $\sin^2 2\theta$ for the two-family oscillations between the second and third families being ~4–9$\times 10^{-3}$. If the lepton sector follows this pattern, we might also expect 2–3 family oscillations with similarly small mixing angles.

In addition, if the relative masses of the three families of neutrinos follow the pattern of the quarks and charged leptons, the ν_τ should be the heaviest neutrino by far, so the mass difference between it and the ν_μ should be large and nearly identical to the ν_e–ν_τ mass difference. Since neutrino beams can be constructed with very little ν_τ contamination, it is convenient to perform a high-mass oscillation search in an accelerator-based ν_τ appearance experiment. The choice of focus on $\nu_\mu \rightarrow \nu_\tau$ instead of $\nu_e \rightarrow \nu_\tau$ is based on the neutrino beamline composition, which is comprised principally of ν_μ from π^+ and K^+ decay.

So, using quark–lepton symmetry arguments, one can see the rationale behind searching for small mixing angles and for choosing the ν_τ in a large mass oscillation search. But symmetry alone cannot provide the motivation for searching for neutrino mixing at large masses. This comes from cosmology.

The dark matter problem has become well-known in astrophysics: luminous matter comprises only a small fraction of the known matter in the universe. The identity of this dark matter is unknown, but the COBE results [107] on the anisotropy of the microwave background radiation as well as measurements [108] of galaxy clustering suggest that at least part of the dark matter must be hot, i.e. it was relativistic when it decoupled from thermal equilibrium [109]. If neutrinos have mass, they would contribute to this hot dark matter. Assuming that the dark matter is composed mainly of ν_τ (assuming it is the most massive neutrino), a mass of 1–10 eV/c^2 would account for the unobserved mass in the universe. This is precisely the mass range that the NOMAD experiment is designed to explore.

Chapter 2

Apparatus and Data

The analysis in this thesis was performed on data taken over four years (1995–1998) by the NOMAD collaboration at the CERN particle physics laboratory near Geneva, Switzerland. This chapter describes the neutrino beam facility at CERN, the NOMAD detector, the data collection, and the Monte Carlo simulated data.

2.1 West Area Neutrino Facility (WANF)

The West Area Neutrino Facility (WANF) [110] at CERN is the source of the wide band neutrino beam that is simultaneously incident on both the NOMAD [98] and CHORUS [93] detectors. This beamline (T9) has been used for neutrino physics since its initial operation with the start of the Super Proton Synchrotron (SPS) in December 1976. The same facility, with a slightly different configuration, was also used for the CHARM II experiment [111]. A schematic diagram of the WANF is shown for reference in Fig. 2.1.

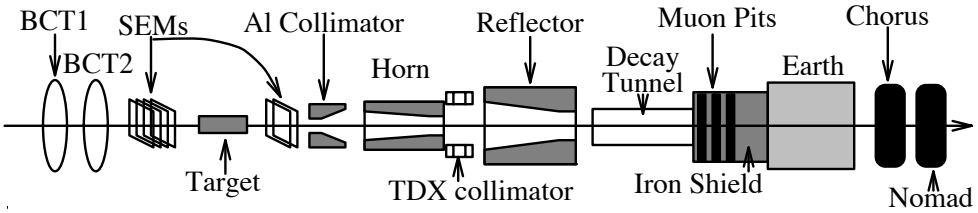

Figure 2.1: Schematic diagram of the West Area Neutrino Facility at CERN (not to scale). The beam travels from left to right in this picture.

A Monte Carlo simulation program, called NUBEAM, has been written to model the neutrino beam produced by the WANF. NUBEAM is based on the GEANT [112] particle tracking package and the FLUKA [113] generator. The particle distribution plots shown in this chapter were generated using NUBEAM version 5.02 and the standard FLUKA (FLUKA '92) generator. Since this generator does not accurately reflect

the extreme forward direction secondary particle distributions, two alternative models have beem developed. One model [114] is based on an updated version of the generator (FLUKA '95), and the other [115] uses neutrino interaction data from NOMAD to empirically parameterize the kaon and pion distributions at the T9 target. The flux tables shown in this chapter and used in the analysis are derived from the average values of these two NUBEAM modifications.

The SPS accelerates protons up to 450 GeV/c. It has a duty cycle of 14.4 seconds, during which two proton extractions are made to the T9 target. These two 6 ms spills are separated by about 2.7 seconds, and they each provide $\sim 10^{13}$ protons-on-target (p.o.t.) per SPS cycle. Two beam current transformers (BCTs) measure the intensity of the proton beam just prior to hitting the target, at which point it has a gaussian profile with a 0.5 mm width.

The proton extractions impinge upon a target composed of eleven cylindrical beryllium rods, each 10 cm long and 3 mm in diameter, with 9 cm gaps between them. The gaps are inserted to reduce the number of secondary particle reinteractions within the target material. The target thus has an effective length of 110 cm of Be, or 2.7 interaction lengths (λ_I). Proton–beryllium interactions in the target create numerous charged secondary mesons, mainly pions and kaons, whose total flux is measured in the secondary emission chambers (SEMs) just downstream of the target. Figure 2.2 shows the energy distributions from the NUBEAM simulation for some of the secondary particle species immediately after the target rods.

This secondary beam is collimated and focused in the 124 m long beam optics section of the WANF, between the target and the decay tunnel. Two specially designed toroidal magnets (labeled horn and reflector in Fig. 2.1 and operating at currents of 100 and 120 kA, respectively) focus positive particles while defocusing negatives. The TDX collimator removes some of the defocused negative particles, while allowing positives to pass through a hole in the middle.

The decay tunnel is a 290 m long evacuated pipe, which allows the pions and kaons to decay in flight. Figure 2.3 shows the expected fluxes for some of the particle species in the beam at the beginning of the decay pipe. Note the relative enhancement of the positive particles vis-à-vis Fig. 2.2.

An unwanted product of the neutrino-producing leptonic meson decays is a large muon flux. At the end of the decay volume there is an additional ~370 m of iron shielding and earth to stop these muons, and a defocusing magnet to bend away those that remain before they reach the experimental hall. The magnet is a 10 m long toroid, with an inner/outer diameter of 2/6 m, operating at a current of 3 kA for a maximum field of 0.72 T

The total distance from the T9 target to the center of the NOMAD detector is 835.6 m; however, it is only 421.5 m from the end of the decay pipe to the detector. The neutrino beam Monte Carlo calculates the average neutrino path length to be 626.2 m. The calculated neutrino distributions at the detector are shown in Fig. 2.4

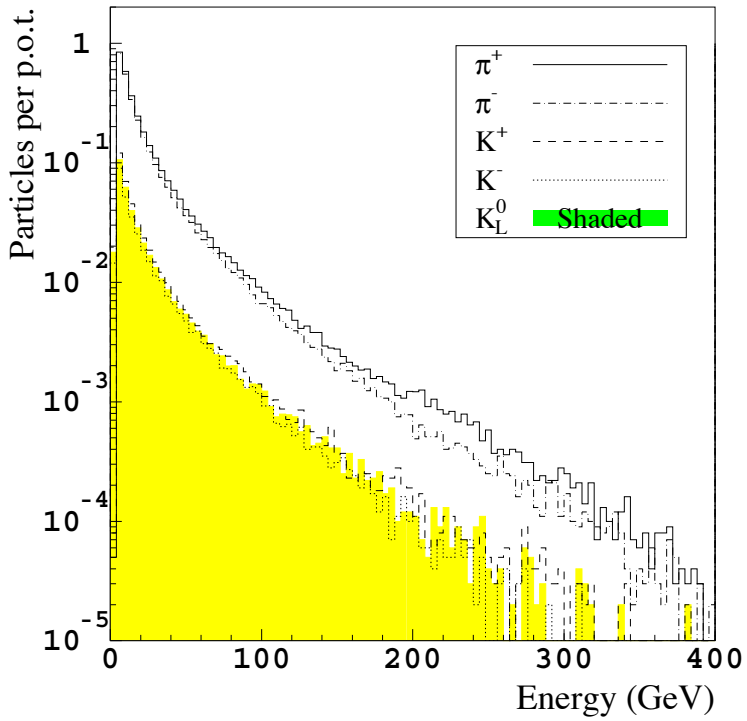

Figure 2.2: Energy distribution of secondary mesons produced in the T9 target, as predicted by the (GEANT-based) NUBEAM Monte Carlo program (version 5.02) using the FLUKA particle generator.

and listed in Tabs. 2.1, 2.3, and 2.2. The values from Tab. 2.3 are used for the data normalization of Ch. 4.

The ν_τ contamination in the neutrino beam has been calculated [117] to give 5×10^{-6} of the ν_μ CC interaction rate in NOMAD. Given the sensitivity of the experiment, this background is negligible.

Neutrino Species	Flux ($*10^4$ p.o.t.)	Fraction (%)	$\langle E \rangle$ (GeV)	Int. Frac. (%)	$\langle E_{int} \rangle$ (GeV)
ν_μ	125.20	91.75	23.6	91.28	45.5
$\overline{\nu}_\mu$	9.75	7.15	23.4	3.52	57.9
ν_e	1.17	0.86	37.2	1.34	59.5
$\overline{\nu}_e$	0.34	0.25	31.4	0.17	57.3
Total	136.47	100	23.7	100	46.6

Table 2.1: Neutrino flux at NOMAD, calculated by NUBEAM 5.02 with the FLUKA '92 generator. "Int. Frac." is the fraction of interactions coming from a certain neutrino type and E_{int} is the energy of neutrinos that interact, assuming a cross section that scales with energy, and also inserting a factor of 0.5 to account for the difference between ν and $\overline{\nu}$ cross sections.

Parent	ν_μ	$\overline{\nu}_\mu$	ν_e	$\overline{\nu}_e$
π^+	91.50%	—	neg	—
π^-	—	84.85%	—	neg
K^+	8.36%	—	65.8%	—
K^-	—	12.41%	—	26.0%
K^0_L	0.13%	1.62%	19.4%	71.4%
μ^+	—	1.12%	14.8%	—
μ^-	neg	—	—	2.6%

Table 2.2: Contributions to neutrino fluxes at NOMAD from various parent particles, as given by NUBEAM 5.02 with the FLUKA '92 generator. Contributions of less than 0.01% are listed as negligible ("neg").

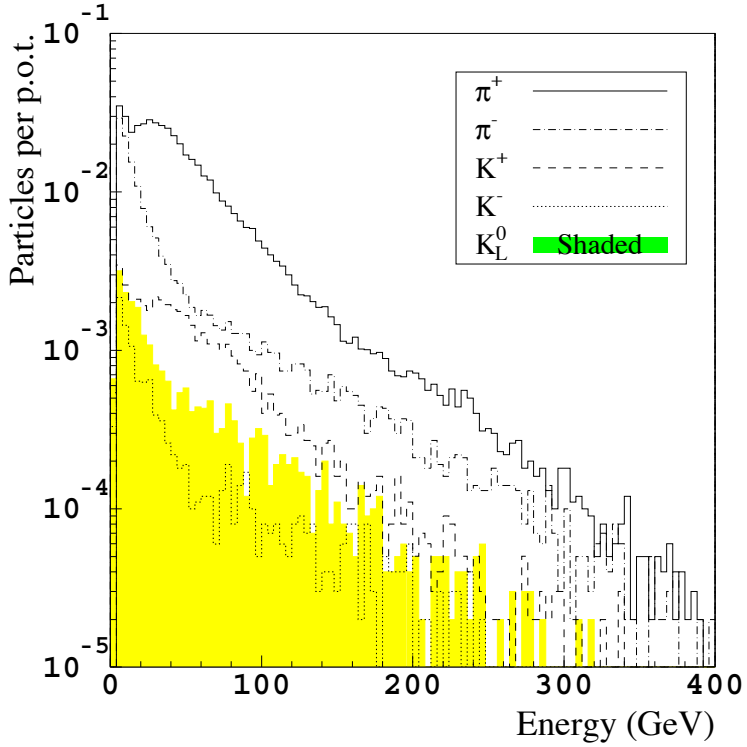

Figure 2.3: Secondary meson fluxes at the entrance to the decay tunnel, as predicted by NUBEAM 5.02.

Neutrino Species	Relative Flux	$\langle E \rangle$ (GeV)	Int. Rel. Flux
ν_μ	1.0	23.7 ± 1.2	1.0
$\overline{\nu}_\mu$	$(5.70 \pm 0.28) \times 10^{-2}$	20.6 ± 2.7	$(2.5 \pm 0.6) \times 10^{-2}$
ν_e	$(9.25 \pm 0.35) \times 10^{-3}$	37.6 ± 2.2	$(1.5 \pm 0.7) \times 10^{-2}$
$\overline{\nu}_e$	$(2.65 \pm 0.21) \times 10^{-3}$	31.3 ± 0.3	$(1.75 \pm 0.21) \times 10^{-3}$

Table 2.3: Neutrino flux at NOMAD, as predicted [116] by FLUKA '95 and the empirical parameterization. The errors reflect the difference between the two methods. "Int. Rel. Flux." is the relative flux of interactions coming from a given neutrino type, assuming a cross section that scales with energy, and also inserting a factor of 0.5 to account for the difference between ν and $\overline{\nu}$ cross sections.

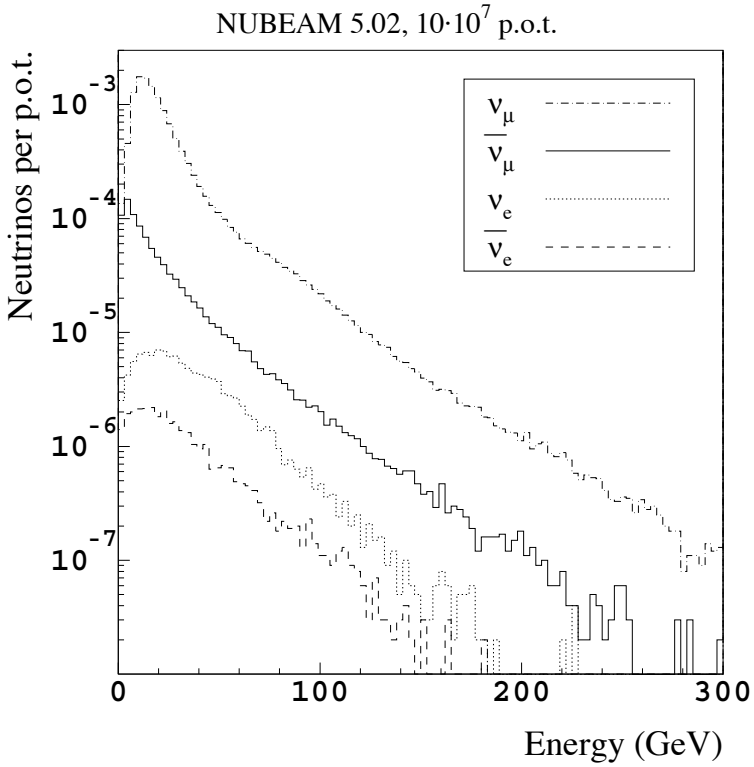

Figure 2.4: Monte Carlo calculation of the NOMAD neutrino beam composition, as predicted by NUBEAM 5.02.

2.2 NOMAD

2.2.1 Overview

The data used in this thesis was recorded by the NOMAD detector, shown in Fig. 2.5. The detector is a multi-purpose neutrino detector which can be used to search for evidence of neutrino oscillations through the reconstruction of kinematic event topologies.

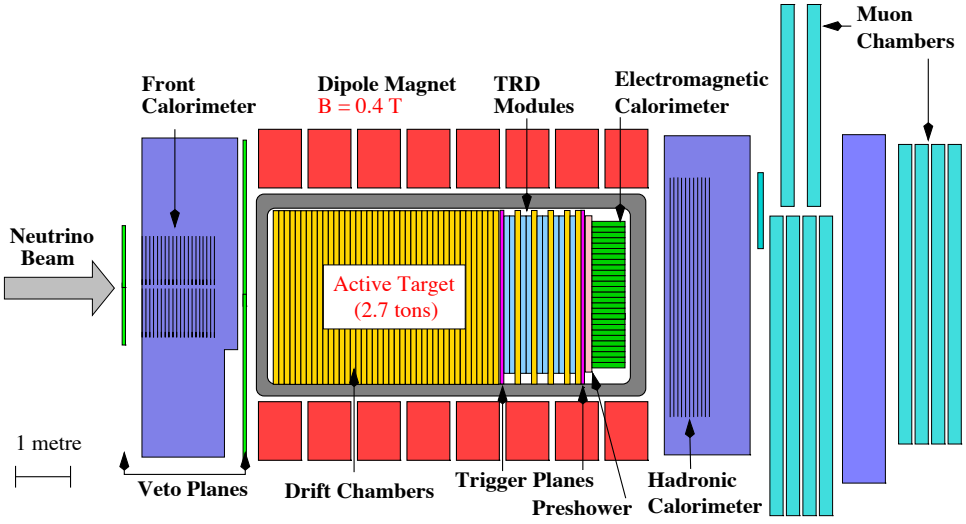

Figure 2.5: Cutaway side view of the NOMAD detector.

Traditional neutrino detectors normally fall into one of two types. On the one hand there are the bubble chambers and emulsion experiments. These detectors use either a supercooled liquid or a photographic emulsion for both the neutrino target and the tracking medium. Events are then scanned visually offline. The advantage of this type of detector is the excellent tracking, allowing precise momentum determination. The disadvantages are in the low event rate, the time-consuming analysis of the photographic data, and the limitations of scale (at least with bubble chambers).

The other type of neutrino detector is a massive instrumented detector, typically a scintillator-steel sandwich. This type of detector is simple and provides for a large fiducial volume with a high neutrino event rate. Since it is instrumented with electronics, most of the uninteresting events can be rejected on-line, making the data analysis simpler. The biggest disadvantages are their poor momentum reconstruction of the events, and their limited particle identification capabilities.

NOMAD has an unusual design in that it combines some of the best features from both of these types of neutrino detectors. It is an electronic detector built with a low

density target. This provides for on-line event discrimination while preserving good resolution. The fiducial volume is a $3 \times 3 \times 4$ m^3 space enclosed by a dipole magnet for momentum determination. It is filled with drift chambers, which serve for both the neutrino interaction target and the charged particle trackers. The entire target represents 2.7 tons with an average density of 0.1 g/m. The most common interaction nucleus in the target is carbon, and so the neutron/proton ratio is very close to unity.

A coordinate system is chosen in NOMAD where the z direction is along the longitudinal axis of the detector in approximately the same direction as the neutrino beam (left to right in Fig. 2.5). The $\hat{y}$ vector points toward the sky, and the x axis completes a right-handed coordinate system. Because of the geography of the SPS and the experimental hall, the neutrino beam is not exactly aligned with the z axis. The T9 target is slightly below the level of the detector, so the beam points upward (in the y–z plane) with a 42.53 mrad tilt. The origin of the coordinate system is at the center of the front face of the first (most upstream) drift chamber module.

2.2.2 Components

The main components of NOMAD are as follows:

- The **Veto Planes** are made of 59 plastic scintillators[1] which provide full coverage (26.3 m^2) of the front (upstream) end of the detector. The veto is used to reject events originating mainly from the muon contaminants in the neutrino beam. The efficiency of the veto counters is $\epsilon_{\text{veto}} = 0.970 \pm 0.005$.

- The **Front Calorimeter** (FCAL) is an instrumented iron/scintillator sandwich calorimeter. Mainly used as an additional veto, at 17.7 tons it is also a prolific source of neutrino interactions. While certain analyses can take advantage of these events, they are not suitable for the type of low background analysis presented in this thesis.

- The **Dipole Magnet** is a large aluminum magnet surrounding the entire drift region. The entire magnet, along with the steel return yoke, has been recycled from the UA1 [119] detector. It provides an average field of 0.4 T in the $+x$ direction, while drawing 5.7 kA of current. The aluminum coils weigh 20 tons and surround a volume of $3.5 \times 3.5 \times 7.5$m^3.

- The **Drift Chambers** (DCs) provide both the tracking for charged particles and the fiducial mass of the neutrino target. There are 44 DCs grouped into 11 modules of 4 DCs each. In addition, 5 DCs are placed in the TRD region for enhanced tracking.

[1] The scintillators were recycled from the "$n\overline{n}2$" experiment [118].

Each DC contains 3 planes of sense (anode) wires, arranged at angles of -5°, 0°, and $+5^\circ$ with respect to the magnetic field. The sense wires are spaced at 6.4 cm intervals, with one cathode wire in between each pair of sense wires. The tracking medium is a 60-40 ethane-argon gas mixture. Each drift chamber represents only 0.02 radiation lengths (X_0).

The sensitive region covered by the DCs extends from $0 < z < 400$ cm and $|x|, |y| < 150$ cm. The momentum resolution of tracks is given by

$$\frac{\sigma_p}{p} \approx \frac{0.05}{\sqrt{L}} \oplus \frac{0.008 \times p}{\sqrt{L^5}}, \tag{2.1}$$

where p is measured in GeV/c and L is in meters, which is roughly 3.5% for typical tracks of momentum $p < 20$ GeV/c.

- The **Trigger Planes** (T1 and T2) consist of strips of scintillator counters arranged into planes before (T1) and after (T2) the TRD region. The planes are 286 cm on a side, and they are separated by 161 cm, at z positions of 408 and 569 cm, respectively. Events are accepted in NOMAD if they register hits in both T1 and T2 and if the veto planes do not fire. The coincidence of these two counters prevents noise in either bank from triggering an event; in addition, it serves to reject most cosmic ray induced events, since only oblique rays could pass through both counters. The Monte Carlo simulation of the detector gives the trigger efficiencies [120] for CC and NC events as 98% and 83%, respectively.

- The **Transition Radiation Detector** (TRD) [121] is located directly behind the DC area, and between the trigger planes T1 and T2. It includes 9 transition radiation modules and 5 DCs interspersed among them for tracking. Each TRD module consists of a radiator followed by a plane of straw tubes. A radiator is an array of 315 polypropylene foils spaced 250 μm apart and filled with nitrogen gas. As charged particles pass the boundaries between foil and gas they radiate energy proportionately to their Lorentz factor γ. For a given momentum, a lighter particle will emit more energy than a heavier particle as it passes through the foils. The straw tubes collect and measure this energy. Each bank of straw tubes has 176 tubes, and successive planes have their tubes staggered to cover the less sensitive regions between individual tubes. The TRD is used mainly as a e/π discriminator, and can reject pions at a level of 10^3 while maintaining a 90% electron acceptance.

- The **Preshower** (PRS) is made of three metal sheets stacked in front of two planes of proportional tubes. The inner metal sheet is a 2 mm thick piece of aluminum, and it is sandwiched between two 4.5 mm Pb-Sb (4% Sb by weight) sheets. Together they represent 1.6 radiation lengths (X_0), and only 0.05 interaction lengths

(λ_I). The energy from conversion photons is detected in the proportional tubes. Since the tubes are arranged horizontally in one plane and vertically in the other, some position information is retained. The preshower is also used as a e/π discriminator, and it can reject pions at a level of 10^2 with 90% electron acceptance.

- The **Electromagnetic Calorimeter** (ECAL) [122] is the last element that is still inside the magnet. (See Fig. 2.5.) It is composed of 875 blocks of lead glass arranged in a 25×35 block array. The front face of each block is $7.9 \times 11.2\,cm^2$ — wider than it is tall. The blocks are 49.4 cm deep, which is $19.8X_0$ and $1.6\lambda_I$. The entire array weighs 20 tons. Cherenkov light emitted in particle showers within the ECAL is collected and gives an overall resolution of

$$\frac{\Delta E}{E} = (1.04 \pm 0.01)\% + \frac{(3.22 \pm 0.07)\%}{\sqrt{E}}, \tag{2.2}$$

  where E is in GeV.

  The glass blocks were calibrated in a test beam before installation. In situ, LEDs attached to each block periodically check and update that calibration, to account for degradation of the response with time. In addition, the effects of the magnetic field are taken into consideration when converting the ADC signal from a lead glass block into an energy.

- The **Hadronic Calorimeter** (HCAL) [123], which lies directly behind the magnet, is another iron/scintillator sampling calorimeter, like the FCAL. Since the total material upstream of the HCAL and downstream from the coordinate system origin represents only $2.1\lambda_I$, the HCAL is necessary to fully contain the hadronic energy in an event. This is extremely important in order to perform the kind of kinematic discrimination used in many $\nu_\mu \rightarrow \nu_\tau$ oscillation analyses, including this one. The HCAL is $3.1\lambda_I$ deep, so together there is only about 0.5% probability that a hadron will pass through without showering. It thus serves to further distinguish hadrons from muons. Since muons leave only a minimum ionizing signal in the ECAL/HCAL system, a muon with momentum above 3 GeVshould be able to penetrate through the calorimeters.

  The position resolution of the HCAL is about 20 cm in both the x and y directions. The y resolution comes from the size of the scintillators used for instrumentation, the x resolution comes from the limit on the amount of light gathered, i.e. on photon statistics. The energy resolution of the HCAL is:

$$\frac{\Delta E}{E} \leq \frac{1.2}{\sqrt{E}}, \tag{2.3}$$

  where E is in GeV.

- The **Muon Chambers** [124] are also recycled from the UA1 experiment. There are five modules of two chambers each, making ten chambers in all. Each chamber consists of four planes of drift tubes: two horizontal and two vertical. Three modules are placed immediately behind the HCAL (station 1), and the remaining two are placed behind an 80 cm thick iron absorber plate (station 2). A small gap in the coverage of the chambers in station 1 was covered by two scintillators, collectively called the muon veto, in late 1995. The geometry of the drift chambers can be seen in Fig. 2.6.

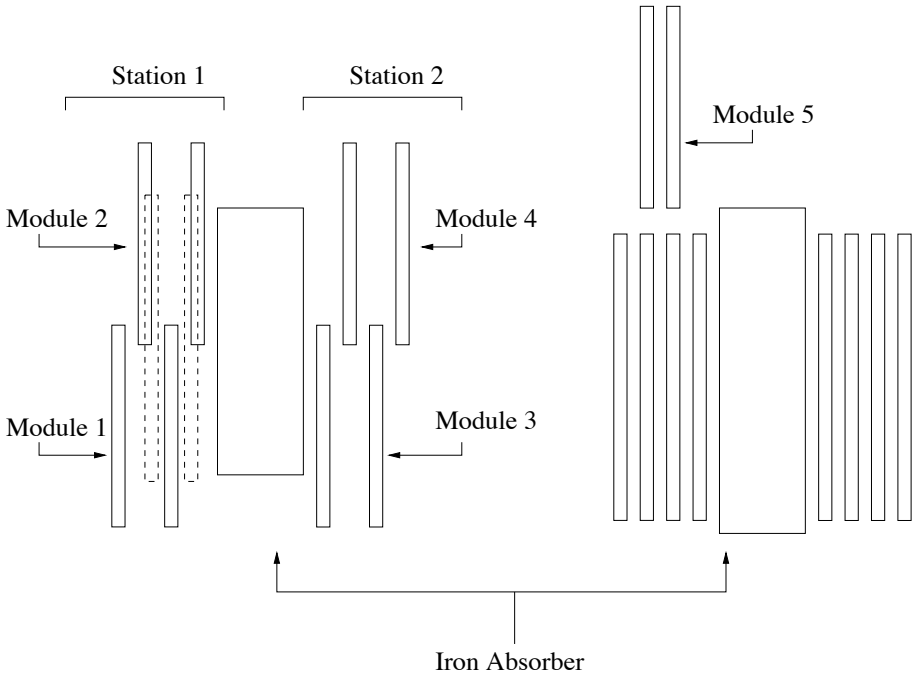

Figure 2.6: Schematic layout of the muon chambers in the NOMAD detector. The left diagram shows the view from above, the right shows a side view.

2.3 Data

The data analyzed in this thesis were gathered over a four year period, from 1995 to 1998. During each year's run, the SPS produced a neutrino beam on the T9 beamline from roughly April to October.

Though NOMAD was scheduled to begin taking data in 1994, a technical problem with the drift chambers caused the detector to be non-operational that year. The faulty chambers were replaced in three stages during the course of the 1995 run. At the

Sample	Protons on T9 Target	Reconstructed DST Events
1995_4	0.3×10^{19}	95712
1995_8	0.3×10^{19}	196989
1995_11	0.3×10^{19}	220844
1996	1.4×10^{19}	846697
1997	1.6×10^{19}	1211845
1998	1.3×10^{19}	752840
Total	5.2×10^{19}	3324927

Table 2.4: Total data collected by year in NOMAD. The trigger, the reconstruction, and the three classes of 1995 data are described in the text.

beginning of that year, between 9 May and 26 June 1995, only the four most upstream modules were present. They covered the region in z from 0 to 110 cm. The next four modules were placed directly behind the first four, $110 < z < 256$, and between 27 June and 15 August eight modules were operational. Finally, from 15 August until the end of the 1995 run on 11 October, all 11 modules were in place. There are thus three data samples from the 1995 run: 1995_4, 1995_8, and 1995_11, corresponding to the number of DC modules installed during those periods.

No major detector difficulties plagued the 1996–1998 runs; however, in 1998, part of the run was dedicated to a $\overline{\nu}$ mode. In this mode, the polarities of the WANF beamline magnets were reversed so that negative mesons would be preferentially focused. This produced a beam of predominantly $\overline{\nu}_\mu$ in the detector. This data sample is excluded from the analysis presented here.

Events were reconstructed offline and stored on data summary tapes (DSTs). Version v7r3 of the DST [125] package produced the data used in this thesis. The statistics for the collected data samples are presented in Tab. 2.4.

2.3.1 Event trigger

The online event trigger [120], as mentioned earlier, consists of the coincidence of the scintillator counters T1 and T2 and the anti-coincidence of the veto planes in front of the detector ($\overline{V} \times T_1 \times T_2$). Although other triggers were simultaneously operational, only the data from this trigger were used in this analysis.

The rate for the $\overline{V} \times T_1 \times T_2$ trigger was consistently around $5.0/10^{13}$ p.o.t. for the 1995–1998 runs. Of these, neutrino interactions in the DC fiducial volume accounted for only $0.5/10^{13}$ p.o.t. with the rest being interactions in the magnet and other non-

instrumented parts of the detector ($2.0/10^{13}$ p.o.t.), straight-through muons that fail to fire the veto counters ($1.5/10^{13}$ p.o.t.), and cosmic rays ($1.0/10^{13}$ p.o.t.).

2.3.2 Event reconstruction

Event reconstruction consists of the following steps: filtering, sub-detector reconstruction, and global fitting. The filtering step removes events with vertices outside the DC fiducial volume and events with only one track.

Each sub-detector then reconstructs appropriate "objects". For the PRS, TRD, and muon chambers this involves converting hits into spatial points for global matching later. The DC and ECAL reconstructions are discussed in separate sections.

2.3.2.1 Charged track reconstruction

Reconstruction of DC hits into track segments is performed in four distinct phases:

1. **Triplet Identification:** Triplets are sets of hits in the three planes ($+5°$, $0°$, $-5°$) of a given drift chamber. Because of the stereo nature of the sense wires in a chamber, left-right ambiguities can be resolved by a triplet, yielding a single (x,y) spatial coordinate.

2. **Helix Identification:** Three triplets (in different chambers) are enough to define a helix. The helix is then described by six parameters: a spatial point (x,y,z), two angles and the sign of the curvature.

3. **Triplet Collection:** After a helix is defined, other DC hits are matched against the projected helix to see if they also belong on it. If other triplets lie in a "road" around the helix they are assigned to this track.

4. **Track Fitting:** Track parameters are then determined from the collection of hits. Position, curvature (momentum), and direction may all be defined from the hits. A Kalman filter is used do determine these parameters in an efficient manner.

The Kalman filter is a step-wise least-squares fitting procedure that avoids the need for large matrix inversions inherent in global least-squares fits. It is especially useful in track fitting in the presence of perturbations from, e.g., multiple Coulomb scattering.

Once all tracks are defined in an event, they are grouped around vertices. A vertex is determined by minimizing a local χ^2 over a sum of tracks in the vicinity. This process is repeated over all local tracks, improving the vertex parameters at each step. This iterative procedure obviates the need for precise initial vertex parameters.

The most upstream vertex is considered to be the neutrino interaction vertex. A downstream vertex with a track leading into it is considered to be the result of a charged particle interaction or decay. The tracks eminating from this vertex are not included in

the determination of the total event energy, as their parent's momentum has presumably already been added.

A downstream vertex with no incoming track is considered to be a neutral particle interaction or decay, and the tracks attached to this vertex *are* included in the event total energy vector. A subclass of the neutral interactions is the V0, in which there are exactly two tracks coming from a neutral vertex, and these have opposite charges.

2.3.2.2 Calorimeter clustering

Calorimeter clustering algorithms determine the size, position, and energy of the showers initiated by particles interacting in the ECAL. The "Harvard" clustering algorithm is used in this thesis, as described below.

After the ADC response of each lead glass block (a "cell") in the ECAL has been converted into an energy, a threshold of 10 MeV is applied to all cells. The clustering algoithm then proceeds as follows:

- A seed cell is found in which the energy is above 30 MeV.
- Adjacent "lit" cells (with energy above 10 MeV) are added to the cluster if they do not already belong to another cluster.
- The cluster grows until no more adjacent lit cells cells are found.
- The cluster centroid is determined from the center-of-gravity method, and the radius is defined as the standard deviation of the distribution of cells.

2.3.2.3 Global fitting

After each subdetector has identified the relevant objects (track, hit, cluster, etc.) in an event, a modified version of the Kalman filter is used to associate objects in different detectors. The Kalman filter allows one to account for small-angle deviations in the flight path of a particle from one subdetector to the next.

The filter begins with tracks in the DC, matching them to TRD and PRS hits, to ECAL/HCAL clusters, and finally to muon chamber hits if possible. If there are calorimeter clusters remaining after matching all the DC tracks, these unmatched clusters are considered to come from neutral particles.

The event reconstruction may be summarized as follows. Charged particles leave hits in the DC, which are reconstructed as tracks. The charges and momenta of the particles are inferred from the curvature of these tracks. Neutral particles may leave no trace in the drift chambers, but they deposit their energy in the ECAL and/or HCAL. Because of the segmented nature of the ECAL, a particle shower may extend over several blocks. Therefore, a clustering algorithm is used to identify individual showers and separate them from neighboring ones. Tracks in the DC are then matched to clusters

in the ECAL; in this way, clusters belonging to charged particles detected in the DC can be separated from "neutral clusters."

So, physical particles are reconstructed either as charged DC tracks or as neutral calorimeter clusters or neutral vertices. In order to avoid clumsy notation, any such reconstructed particle will be referred to as a *particle object* (PO) in later chapters.

2.4 Monte Carlo Data Simulation

Events in NOMAD are simulated through a series of three Monte Carlo programs. The neutrino beam is modelled in the NUBEAM program, described in Sec. 2.1.

The spatial and energy distributions from NUBEAM are used by the next program, NEGLIB [126], to generate neutrino interactions in the fiducial volume[2] of the detector. NEGLIB simulates the Fermi motion of a nucleon and generates a deep inelastic neutrino–nucleon scattering event through the LEPTO [127] package. LEPTO generates parton-level interactions using standard model electroweak cross sections with first order QCD corrections. Hadronization of the partons is done via the Lund string model.

Final state particles are fed into the third Monte Carlo program, GENOM [128], another GEANT-based package, to simulate their interactions with the detector. GENOM simulates both the interactions (showers, decays) of the particles in the detector material and the responses of the individual subdetectors. The GHEISHA [129] package is used by GENOM to simulate interactions in the calorimeters, and FLUKA is used in the tracking detector regions. The results are output in the same format as that used by the real data.

After the event generation, triggering and reconstruction proceed exactly the same as for the data. The Monte Carlo reconstructed events are also stored in the same DST format (v7r3) as the data.

Table 2.5 lists the type and number of Monte Carlo events generated. For simplicity, only ν_μ NC Monte Carlo events were used in this analysis, and they were weighted to account for all NC interactions ($\overline{\nu}_\mu$NC, ν_e NC, $\overline{\nu}_e$ NC). The differences (in energy and vertex position) between the different NC interactions in NOMAD are small.

[2]The Monte Carlo samples used for the analysis in this thesis were generated in a fiducial volume of $|x|, |y| < 140$ cm, $0 < z < 408$ cm.

Sample	Reconstructed DST Events	Monte Carlo / Data (exp.)
ν_μ CC	5032958	3.1
$\overline{\nu}_\mu$ CC	588732	14.5
ν_e CC	2157453	92
$\overline{\nu}_e$ CC	296974	105
ν_μ NC	3067890	5.8
ν_τ 1-prong	637808	—

Table 2.5: Total Monte Carlo events generated by the NOMAD collaboration and used in this thesis. The third column shows the factor by which the Monte Carlo exceeds the number expected in the full data sample. The ν_τ sample includes all non-leptonic τ final states with exactly one charged particle, of which the $\tau \rightarrow \rho$ sample is about 50%.

Chapter 3

Analysis

This chapter presents the techniques used in the data analysis. The general approach is similar to some other ν_τ searches [99] in NOMAD, but the implementation is unique.

The general approach to searching for ν_τ interactions in the NOMAD environment is to identify the decay product(s) of the τ lepton and then determine whether the kinematics of the event has charged current (CC) characteristics with the τ-candidate as the leading lepton. This analysis is concerned with the $\tau^- \rightarrow \rho^-\nu_\tau$ decay channel, so the "visible" decay product is only the ρ^-. The ρ^- identification is detailed in Sec. 3.1. Kinematic determination of the ν_τ is outlined in Secs. 3.2 and 3.2.3.

This analysis was performed blindly on the data; that is, kinematic (cf. Sec. 3.2.3) and event quality cuts (cf. Sec. 3.3) were tuned on data samples distinct from the one used to search for a neutrino oscillation signal. This is a standard technique in NOMAD to avoid introducing biases through the use of cuts designed to eliminate individual events, e.g.

The entire analysis was performed on the data looking for a signal from events with a ρ^- as well as for events with a leading ρ^+. The latter are expected to be entirely from background, as the neutrino beam has only a small anti-neutrino component. The efficiency of the analysis on the Monte Carlo was compared to the data using the ρ^+ samples, and correction factors were derived from this comparison to account for systematic effects in the Monte Carlo (see Sec. 3.4). The signal efficiency and background expectation for the ρ^- analysis were derived from the Monte Carlo ρ^- samples, corrected by said factors. Only when a final set of cuts was determined from the ρ^+ samples and the Monte Carlo ρ^- was the ρ^- data examined in the predefined signal region, hereafter known as "the box". The examination of the ρ^- signal inside the box is called "opening the box". Chapter 4 presents the results from opening the box.

$$\nu_\tau\, n \rightarrow \tau^- p$$
$$\hookrightarrow \rho^-\nu_\tau \text{ (Br=25\%, } c\tau\text{=86}\mu\text{m)}$$
$$\hookrightarrow \pi^-\pi^0 \text{ (Br=}\sim\text{100\%, } c\tau\text{=1fm)}$$
$$\hookrightarrow \gamma\gamma \text{ (Br=98.8\%, } c\tau\text{=25nm)}$$

Figure 3.1: The ν_τ–N CC interaction and subsequent $\tau^- \rightarrow \rho^-\nu_\tau$ decay chain.

3.1 Rho Identification

Reconstructing ρ (770) mesons in NOMAD is a challenging task. The ν_τ interaction and $\tau \rightarrow \rho$ decay chain are shown in Fig. 3.1. The only particles which may be visible in the detector are the π^- and the photons. If both γ's are detected, their invariant mass should be close to the π^0 mass. Adding the momenta of the photons together gives the momentum of the π^0 from which they originated. The invariant mass of this new PO and the π^- should give the ρ^- mass. The width of the π^0 mass peak is limited by the resolution of the detector; the mass width of the ρ (770) is much larger (150 MeV/c^2) than the detector resolution. Nevertheless, both masses can be used to help identify the ρ^-.

3.1.1 Photon identification

Since photons shower electromagnetically, their shower energy should be contained within the ECAL. The other predominant neutral particles in NOMAD (neutrons and K^0_L's) have longer, hadronic showers. To a good approximation, then, any neutral ECAL cluster with no corresponding HCAL energy can be identified as a photon.

It is not certain that a γ produced at the interaction vertex will survive to the ECAL, though. The DCs themselves represent around 0.9 radiation lengths, although the photons would only have to pass through a fraction of that depending on the position of the neutrino interaction vertex. The TRD region contributes another $0.9X_0$ of material, and the probability of reconstructing the electron tracks decreases as one gets closer to the back of this region. Altogether, about half of the photons produced in π^0 decay convert in the detector.

The approach taken by this analysis is to begin as inclusively as possible in the ρ identification, and use kinematic requirements to remove the backgrounds. Only when it becomes apparent that the combinatorial backgrounds are drowning the signal in a given class will that class be excluded. This also applies directly to the γ and π^0 identification. Table 3.1 lists all the reconstructed photon classes described in this section.

Of the photons that convert, three classes of identification signals are defined. First, if the tracks of the electron and positron are both reconstructed and if the invariant

Class	Name	Description
1	ECAL	No photon conversion, cluster found in ECAL
2	V0	Photon converts to e^+e^- pair, both tracks reconstructed
3	Hanger	Photon converts to e^+e^- pair, only one track reconstructed
4	PVTX	Photon converts to e^+e^- pair near primary vertex

Table 3.1: Reconstructed photon classes, further description given in text.

mass of the pair is less than 100 MeV/c^2 (see Fig. 3.2) then the PO formed by the sum of the two tracks is called a V0, and because of the good resolution of the DC it should represent well the γ momentum. This is the clearest γ conversion signal in the detector.

If one of the electrons has very low energy, its track's radius of curvature may be too small for the track reconstruction algorithm to identify cleanly. In this case, only one of the conversion electrons will be found, and it should be separated by some distance from the event vertex. These tracks are called "hangers"; for this analysis all hangers separated from the event vertex by at least 15 cm in z and 5 cm in x and y are accepted as γ candidates. This imaginary box around the event vertex is called the "loose vertex", and will be referred to later.

The third conversion class includes photons which convert soon after production, near the primary event vertex (PVTX). This class is expected to have the largest combinatorial background so a few loose cuts are applied to help reduce the obvious misidentifications. All pairs of oppositely charged tracks are considered, and only those with invariant mass less than 50 MeV/c^2 are kept (see Fig. 3.2). The point of closest contact between the lines defined by the tracks' starting points and their momenta must be less than 1 cm. This is a somewhat complicated way of ensuring spatial proximity.

The third requirement for PVTX photons relies on the fact that the electron–positron pair from a photon conversion will have no inherent opening angle. Initially, the electron and positron should be travelling in the same direction, and they are only separated by the action of the magnet. Because of imperfect resolution/reconstruction, this separation might appear to give the electrons a small, but non-zero opening angle. Since the magnetic field is in the x direction, any induced opening angle should be in the y–z plane. The coplanarity $\mathcal{C}$ of two vectors $\vec{a}$ and $\vec{b}$ in the presence of a magnetic field $\vec{B}$

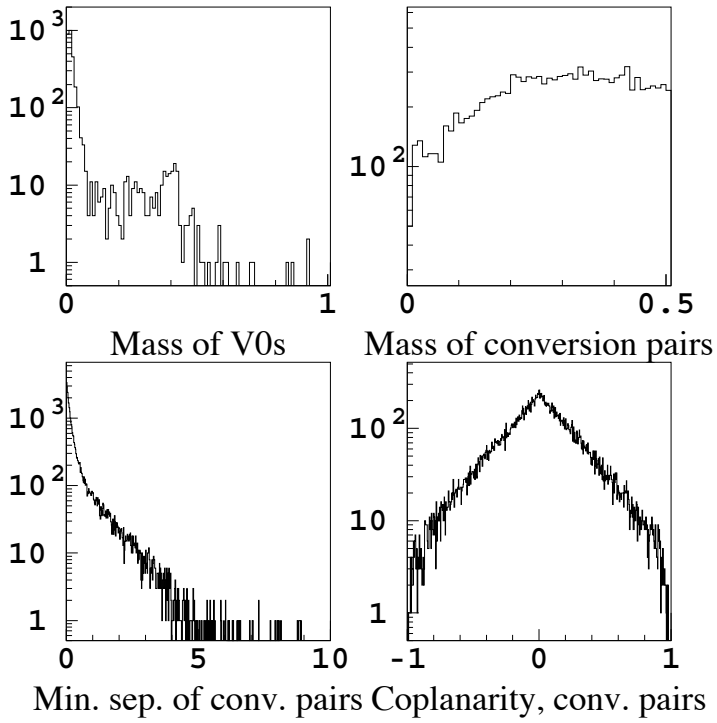

Figure 3.2: Clockwise from top left: V0 invariant mass (GeV/c^2), PVTX pair invariant mass (GeV/c^2), coplanarity for PVTX pairs, minimum separation for PVTX pairs (cm). Data taken from a sample of τ MC events, and each plot includes both real photons and the combinatorial backgrounds.

in the x direction is defined as:

$$\mathcal{C}(\vec{a}, \vec{b}|\vec{B} \propto \hat{x}) \equiv \frac{(\vec{a} \times \vec{b}) \cdot \hat{y}}{|\vec{a}||\vec{b}|}. \tag{3.1}$$

In NOMAD this reduces to the product $\sin\xi \sin\zeta$, where ξ is the opening angle of the two tracks and ζ is the angle between the plane defined by the two momentum vectors and the y–z plane. As both angles tend to zero for photon conversions, $\mathcal{C}$ should be very small; it is larger for most of the combinatorial background. $|\mathcal{C}|$ was required to be less than 0.05 (cf. Fig. 3.2).

3.1.2 π^0 identification

Once a collection of photons has been identified in an event, an attempt is made to form a π^0 candidate from them. The simplest case would be to find two γ candidates

whose invariant mass lies close to the π^0 mass of 135 MeV/c^2. Given the four classes of photons defined above, there are ten categories of π^0 made up of pairs of γ's. In principle, the resolutions may be different for each photon class, so the π^0 mass cuts should be different for each of these ten classes. However, for simplicity, and in keeping with the inclusive nature of the particle identification of this analysis, the mass range was chosen uniformly to be [50,200] MeV/c^2. This represents at least 2σ on each side of the centroid for each of the ten π^0 classes. Figure 3.3 shows the expected mass peaks for four of the π^0 classes.

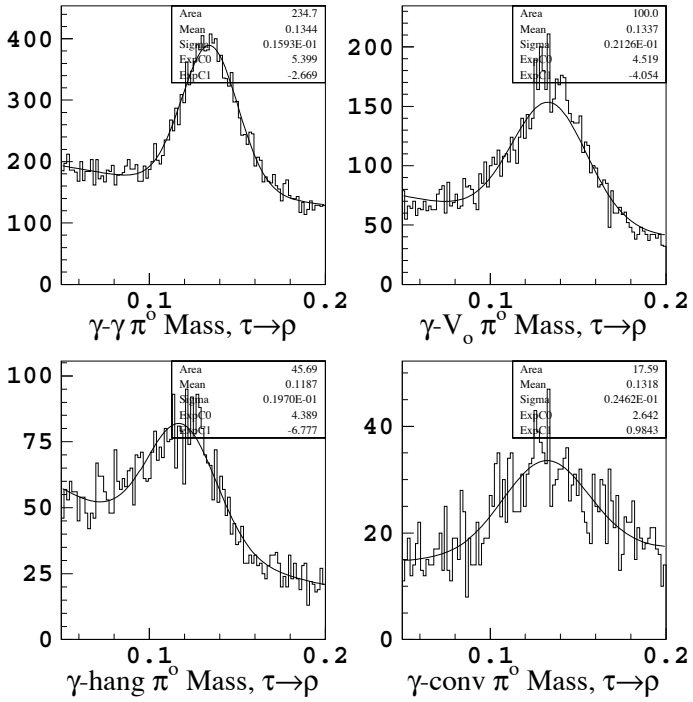

Figure 3.3: π^0 invariant mass plots (in GeV/c^2) from a sample of $\tau \rightarrow \rho$ MC events, for various combinations of photons. Clockwise from top left are shown: two neutral ECAL clusters, one ECAL cluster and one V0, ECAL–PVTX conversion, and ECAL–hanger.

Sometimes the two photons from π^0 decay are not resolved in the ECAL. If the distance from the event vertex to the ECAL is too small, or the π^0 energy is too great, the photons' showers will overlap sufficiently in the ECAL that they will only be reconstructed as a single cluster. In this case, the energy of the neutral PO will reflect the π^0 energy, and the position of the cluster with respect to the PVTX will define its direction. Since this approximates the π^0 energy and direction anyway, a single ECAL

photon is also accepted as a π^0 candidate, though of course no π^0 mass cuts can be made.

3.1.3 π^- identification

Identifying π^- in NOMAD is relatively straightforward. First, all negatively charged tracks coming from near the primary vertex (specifically, from the loose vertex) are considered. It is difficult to distinguish different hadrons efficiently in NOMAD, but electrons and muons can be removed from this sample.

3.1.3.1 Electron rejection

Charged particles are assumed to be hadrons in NOMAD unless identified as electrons or muons. Electrons have much lower masses than hadrons and so can be identified by the TRD, and they shower electromagnetically so they can also be identified in the PRS and ECAL.

In this analysis, electron identification is only necessary as a veto for the charged pion identification. Since the inherent leading electron contamination is smaller than the leading muon contamination (from ν_e and ν_μ CC interactions, respectively) by almost a factor of 100, the electron identification has a somewhat reduced importance.

For this analysis, a standard electron ID procedure was used that was found useful [130] in one $\nu_\mu \rightarrow \nu_e$ oscillation search in NOMAD. The cuts are as follows, the variables are defined afterwards:

- $P > 1.5$ GeV/c
- $|\text{POECVX}|, |\text{POECVY}| < 130$ cm
- $\text{ECLUS} > 0.75$ GeV
- $\text{PRSEV} + \text{PRSEH} > 5$ MIPs
- $\frac{E-P}{E+P} > -0.3$
- $\text{PICON} < 0.001$

P is the track momentum measured in the DCs. POECVX and POECVY are the x and y positions, respectively, of the intersection of the projected DC track with the front face of the ECAL. This cut ensures that the particle should hit the ECAL within its sensitive area. ECLUS is the ECAL cluster energy associated with the track. PRSEV (PRSEH) is the energy deposited in the horizontal (vertical) tubes of the PRS, normalized to the energy deposited by a minimum ionizing particle (MIP).

E is a modified ECAL cluster energy. If an electron undergoes Bremsstrahlung radiation in the detector, photons will be emitted at tangents to the electron track. These

photons will create clusters in the ECAL in a vertical strip above (below) the main electron (positron) cluster. A simple algorithm adds the energy found in such a strip to the cluster energy, ECLUS, to get a Bremsstrahlung-adjusted calorimeter energy, E.

PICON [131] is an acceptance variable based upon the response of the TRD. The TRD was calibrated in a test beam prior to installation in NOMAD, and the detector response to electrons and pions was observed. The energy deposition distributions can then be parameterized and probability distributions constructed. $P(\epsilon_i|e,p)$ is the probability that an electron of momentum p deposits an energy ϵ_i in TRD station i; $P(\epsilon_i|\pi,p)$ is the corresponding probability for a pion. The log-likelihood ratio is defined from these probabilities as:

$$LH \equiv \sum_{i=1}^{n_{hit}} \log \frac{P(\epsilon_i|e,p)}{P(\epsilon_i|\pi,p)}, \tag{3.2}$$

where n_{hit} is the number of TRD planes with energy deposited in them. Figure 3.4 shows the likelihood distributions for 10 GeV/c electrons and pions.

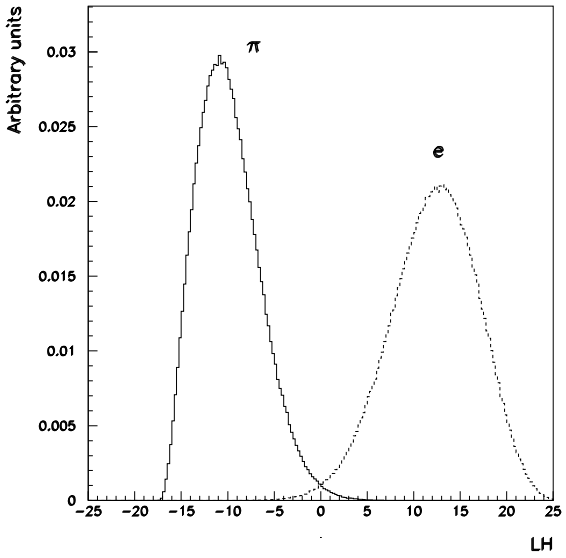

Figure 3.4: TRD log-likelihood distributions for 10 GeV/c electrons and pions. Figure taken from Ref. [131].

With a sample of likelihood distributions for particles at different energies, acceptance functions can be derived by integrating:

$$A_j = \frac{1}{N_j} \int_{LH}^{\infty} dl \left. \frac{dN_j}{dl} \right|_{p,n_{hit}}, \tag{3.3}$$

where $j \in (e, \pi)$, $\left.\frac{dN_j}{dl}\right|_{p,n_{hit}}$ is the likelihood distribution for particle j with momentum p, and N_j is the number of particles in each distribution. $A_\pi(LH) \equiv$ PICON is thus the fraction of pions with likelihood ratios greater than LH. A_e is the equivalent acceptance function for electrons, called ELACC. Figure 3.5 shows these functions.

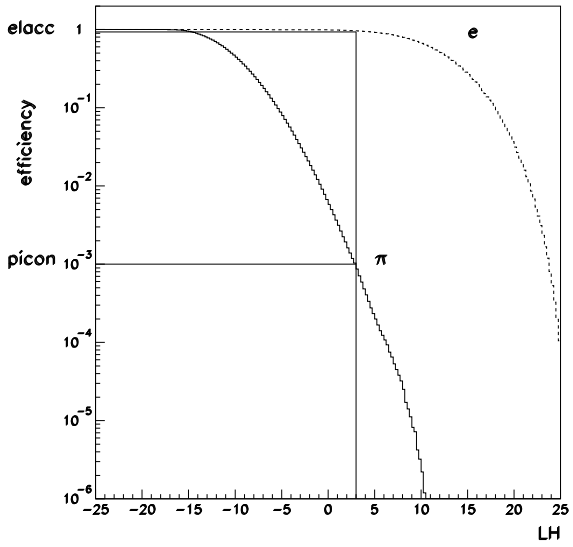

Figure 3.5: The TRD acceptance functions PICON and ELACC, derived by integrating the log-likelihood functions. Figure taken from Ref. [131].

The functions PICON and ELACC are correlated. For a cut of PICON < 0.001, only 0.1% of pions should be accepted, and correspondingly, about 90% of electrons are accepted. For an electron veto this is not a very stringent cut, but it is sufficient to reduce the electron background while maintaining a high pion detection efficiency.

3.1.3.2 Muon rejection

Muons are the most abundant backgrounds to the π^- in this analysis. If a leading μ^- from a standard ν_μ CC event is misidentified as a π^-, and then combined with a π^0 in the same event, that combination could look very much like the ρ^- from the τ^- decay in a ν_τ CC event.

The muon chambers and both calorimeters are used to reject muons from the π^- sample. Since muons are minimum ionizing particles (MIPs), they tend to leave only a small signal in the calorimeters relative to their momenta as measured in the DC. For the same reason, they are highly penetrating, much more so than electrons and hadrons.

Once parameterized, one can project a DC track into the muon chamber stations. Given the path length and detector geometry, one can also estimate the amount of material a muon would travel on its way to the muon chambers. Taking Coulomb scattering

into account yields a probability distribution for the position of a muon at the muon chambers. The integral of this p.d.f. over the sensitive area of a drift chamber element multiplied by the detector efficiency yields the probability to hit that element. The probabilities to hit station 1, station 2 and the muon veto are, respectively, PROBHIT1, PROBHIT2, and PROBHITV. These variables are calculated during the event reconstruction.

Three related variables are the probabilities of the muon ranging out in the material of the calorimeters and/or the iron absorber before reaching the muon stations, given the muon momentum and assuming it is a MIP. For reaching station 1, station 2, and the muon veto, the probabilities are PROBRCH1, PROBRCH2, and PROBRCHV, respectively.

Thus, the probability of a given muon PO to leave a signal in the muon station 1 would be PROBRCH1 $*$ PROBHIT1, for instance. The probability for a muon to *fail* to leave a hit in any of the muon chamber elements would then be the product

$$\prod_{i=1,2,V} (1 - \text{PROBRCH}i * \text{PROBHIT}i). \tag{3.4}$$

The probability of a muon to *hit* one of the muon chamber elements would just be the complement of this, labelled MUHITPROB. In order to reject muons from the pion sample, all pion candidates are required to have a high probability to hit the muon chambers, MUHITPROB $> 99\%$, combined with the lack of any hits in a circle of 40 cm around the projected track in any muon chamber elements.

The calorimeter information can be turned into a MIP likelihood by using the detector responses, similarly to the way the PICON and ELACC functions were derived from the TRD response (see Sec. 3.1.3.1). Both the ECAL and HCAL information is used, if available. If there is a possibility of track overlap in either detector, or if no energy is assigned to the track, then that calorimeter is not used in the likelihood. The MIP likelihood probability, PROBMUCAL, is required to be less than 10% for pion candidates in this analysis.

One further check is made on the projected track. Along with small perturbations from normal Coulomb scattering, sometimes a muon deposits a large amount of energy in one interaction, and its direction is changed at that point. In this case, a muon in the DC might still leave hits in the muon chambers, but they would not line up with the projected DC track. So, if a track segment (stub) can be defined from a series of hits in the muon chambers, this stub is projected backwards towards the DC. If this projection comes within 50 cm of the DC track (projected forward), the PO is rejected as a "catastrophic energy loss muon" or simply "muon catastrophe".

The muon veto requirements for the π^- candidates are summarized as follows:

- MUHITPROB $> 99\%$
- No hits in either muon station or in the muon veto scintillators

- PROBMUCAL $< 10\%$
- Not a muon catastrophe

Notably, there is no explicit momentum requirement made of the pion candidate. The MUHITPROB cut imposes an implicit lower threshold of about 3 GeV/c, though.

3.1.4 Rho isolation requirement

Once a collection of π^0 and π^- candidates has been selected, combinations are added to form ρ^- candidates. A loose mass cut of $600 < M_\rho < 1200$ MeV/c^2 is applied to these candidates. Of those that remain, a maximum of one per event is selected. This is done by requiring the ρ PO to have the highest isolation variable, I, of any PO in the event.

The isolation variable [132] is designed to select the PO with the momentum which is most separate (isolated) from the others. In a CC event, this should ideally be the leading lepton (or leading τ decay product). For an event with N PO's, the value of the isolation variable for a PO j is:

$$I(j) \equiv \frac{1}{N}\sum_{i=1}^{N}\left(\frac{\vec{p_i}\times\vec{P_0}}{|\vec{P_0}|}\right)^2 - \frac{1}{N-1}\sum_{i\neq j}\left(\frac{\vec{p_i}\times\vec{P_j}}{|\vec{P_j}|}\right)^2, \tag{3.5}$$

where each PO i has momentum $\vec{p_i}$, and

$$\vec{P_0} \equiv \sum_{i=1}^{N}\vec{p_i} \;\;,\;\; \vec{P_j} \equiv \sum_{i\neq j}\vec{p_i}.$$

The cross product terms can be interpreted as the transverse momentum of some PO with respect to a reference momentum vector listed in the denominator. For all the PO's in a given event, one can see that the first term in Eq. 3.5 is ordinarily a constant, as is the $1/(N-1)$ factor of the second term. If we are only interested in finding the PO with the maximum I in an event, then, we should only have to find the minimum of the second sum.

In this analysis, however, the number of PO's in an event can change depending on how the ρ is defined. For instance, if one had an event with N PO's initially, and then one formed a ρ^- from a π^- and a single ECAL γ, the effective number of PO's would be $N_{\text{eff}} = N - 1$. If the π^0 candidate comes from two photons, both of which convert near the PVTX, then $N_{\text{eff}} = N - 4$. Both of these ρ candidates could be found in the same event, so the full expression (Eq. 3.5) for I is necessary, taking into consideration the number of PO's in the event for each ρ candidate.

A successful ρ candidate must have the largest value of I for any PO in the event, including other ρ PO's.

3.2 Leading Lepton Identification

Since the NOMAD detector is incapable[1] of resolving the decay vertex of the τ from the ν_τ–N interaction vertex, the τ is identified by the kinematics of the event. Since a τ candidate may also originate from the hadronic shower of a NC or non-ν_τ CC event, one must show that the event comes from a CC interaction and that the identified τ is the leading lepton.

3.2.1 Neutral current and charged current events

The difference between NC and CC neutrino events is very simple: the outgoing lepton in NC events (a neutrino) is not observed in the detector. The effect on the kinematics of the event is best seen in the plane transverse to the beam axis. Since the baseline of the experiment is so long, the neutrinos crossing the detector are essentially parallel [2] to each other. Therefore, the x–y plane of the detector is approximately[3] transverse to the beam.

In this plane the neutrinos have no momentum, so by momentum conservation the vectorial sum of the momenta of the interaction products must be zero. This can be seen in Fig. 3.6, in which three vectors and two angles are defined by illustration.

Figure 3.6a shows the momentum vectors of an ideal CC event in the transverse plane. The lepton momentum is labelled $\vec{\ell}$, and the particles in the hadron jet are shown by the short lines with no arrows. Their vectorial sum forms the hadron vector, labelled $\vec{h}$. The angle in the transverse plane between $\vec{\ell}$ and $\vec{h}$ is $\phi_{\ell h}$. Since the diagram assumes an ideal detector, the sum of $\vec{\ell}$ and $\vec{h}$ is $\vec{0}$.

In a real detector there is some mismeasurement (see Fig. 3.6b), and a new vector $\not{\vec{P}}_\perp$ is defined such that $\vec{\ell} + \vec{h} + \not{\vec{P}}_\perp \equiv \vec{0}$. $\not{\vec{P}}_\perp$ is called the missing momentum, since in a CC event as the measurement errors vanish, so does $\not{\vec{P}}_\perp$. In a CC event, $|\not{\vec{P}}_\perp|$ ($\equiv \not{P}_\perp$) should be small compared to the magnitudes of $\vec{\ell}$ and $\vec{h}$ (P_ℓ and P_h, respectively). The angle between $\not{\vec{P}}_\perp$ and $\vec{h}$ is defined as ϕ_{mh}; this has no preferred value in a CC event.

An ideal NC event is diagrammed in Fig. 3.6c. Here, the outgoing neutrino (momentum marked by a dashed lined and labelled $\vec{\nu}$) escapes detection; only the hadron vector is measured. Thus, the missing momentum in a NC event takes on the characteristics of the lepton momentum of a CC event. The angle ϕ_{mh} is 180°, and $\phi_{\ell h}$ is undefined.

[1] At the energies of the NOMAD neutrino beam, the τ produced would travel on the order of 1.5 mm before decaying. The resolution of the detector in the z direction is on the order of several cm.

[2] The mean beam divergence is calculated in the NUBEAM Monte Carlo program to be ~1 mrad.

[3] There is a systematic angle in the neutrino beam of 42.5278 mrad in the y–z plane—the beam is coming slightly up out of the ground—but this is accounted for in software and thus neglected in all further discussions.

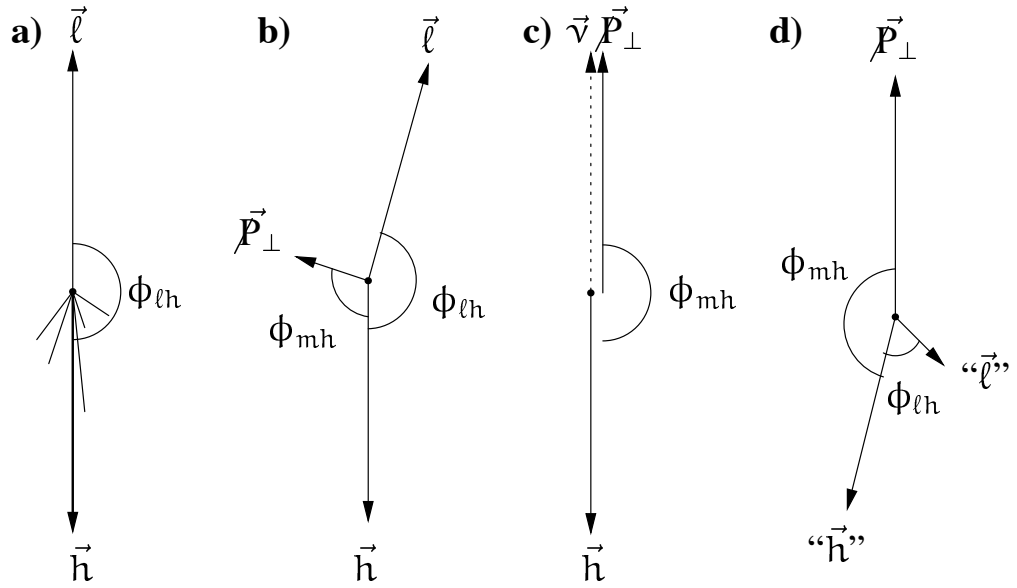

Figure 3.6: Lepton ($\vec{\ell}$), hadron jet ($\vec{h}$), and missing ($\vec{\not{P}}_\perp$) momentum vectors in the plane transverse to the neutrino beam for CC (a,b) and NC (c,d) interactions. Diagrams a) and c) assume perfect detector resolution, b) shows the effect of modest energy mismeasurement, and d) shows a NC event analyzed as a CC event.

In order for a NC event to mimic a CC event, one or more particles in the hadron jet must be assigned to the lepton vector; the remaining particles form the hadron vector. This situation is illustrated in Fig. 3.6d, where the quotation marks are used to note that neither $\vec{\ell}$ nor $\vec{h}$ represents the true lepton or hadron vector.

Comparing diagrams 3.6b and 3.6d, one can see several kinematic distinctions between CC and NC events. First, the missing momentum is generally larger in a NC than in a CC event. The angle $\phi_{\ell h}$ peaks at 180° in CC events, but is smaller in NC. ϕ_{mh} does the reverse: it peaks at 180° for NC, and has a flat distribution in CC.

It is common to show so-called ϕ–ϕ plots ($\phi_{\ell h}$ vs. ϕ_{mh}) to illustrate these differences. Figure 3.7 shows the differences between CC and NC events in this plane.

It was pointed out [133] that the angles $\phi_{\ell h}$ and ϕ_{mh} become undefined when the relevant momenta defined in Fig. 3.6 tend toward zero. The solution presented was a new set of variables based on the magnitudes of the momenta in the transverse plane.

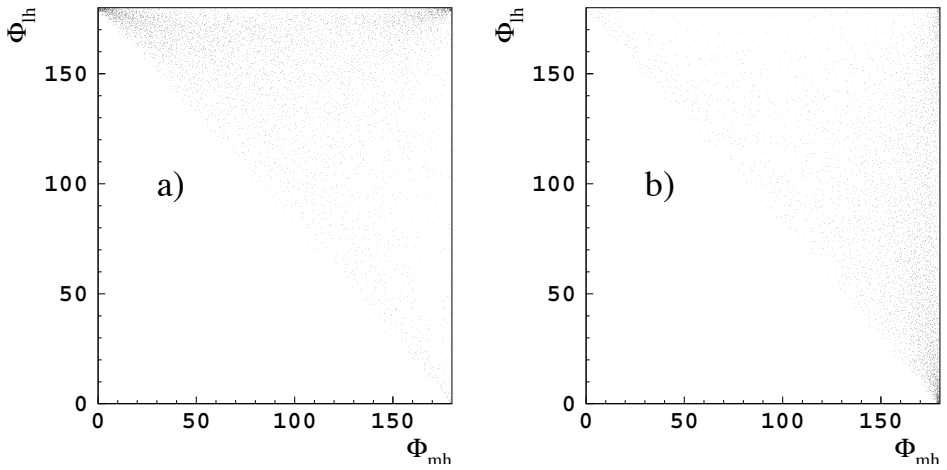

Figure 3.7: $\phi_{\ell h}$ vs. ϕ_{mh} for samples of CC (a) and NC (b) events from the Monte Carlo. All angles are in degrees.

With $M = P_\ell + P_h + \not{P}_\perp$, we have the three quantities:

$$\begin{aligned} \rho_\ell &= \frac{P_\ell}{M} \\ \rho_h &= \frac{P_h}{M} \\ \rho_m &= \frac{\not{P}_\perp}{M}. \end{aligned} \tag{3.6}$$

The data shown in Fig. 3.7 is replotted in a "ρ–ρ" plot (ρ_h vs. ρ_ℓ) in Fig. 3.8.

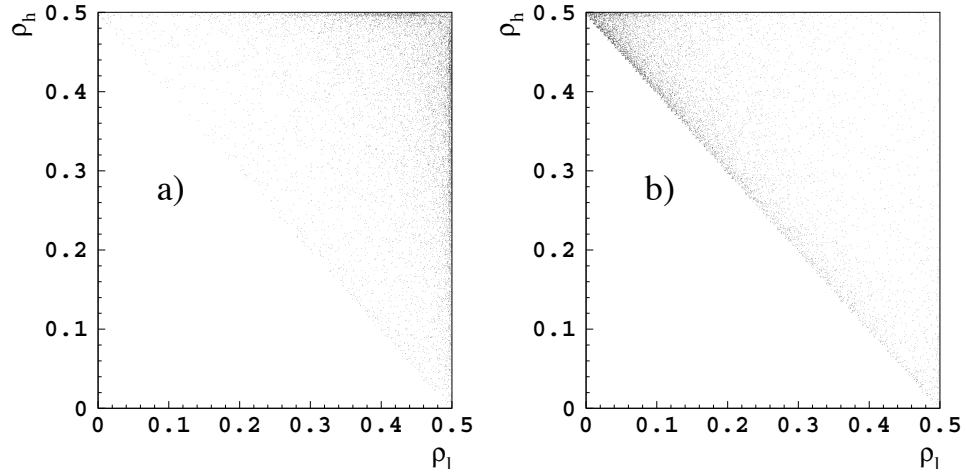

Figure 3.8: ρ_h vs. ρ_ℓ for samples of CC (a) and NC (b) events from the Monte Carlo.

3.2.2 Separating ν_τ events from charged current events

Once a particle or group of particles is identified as the τ decay product(s), one must show that these do not come from either a standard ν_μ (or ν_e) CC event or from a NC event.

The kinematics of ν_τ CC ($\tau \rightarrow \rho\nu_\tau$) events share elements of both ν_μ CC and NC events. Figure 3.9 shows a momentum vector diagram of a ν_τ CC event with the τ and hadron vectors drawn exactly like those in the equivalent ν_μ CC event of Fig. 3.6b. The τ vector is drawn with a dotted line, because it is not observed in the event. Instead, its decay ρ and ν_τ are shown, with only the ρ being detected. The ν_τ momentum is added vectorially to the missing momentum, and the new angles are labelled.

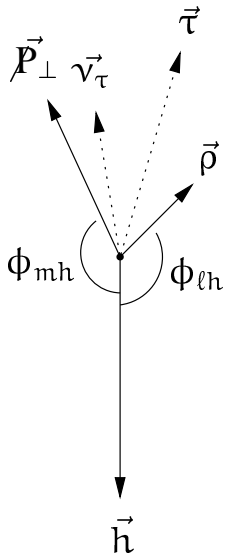

Figure 3.9: Kinematic vector diagram of a ν_τCC ($\tau \rightarrow \rho\nu_\tau$) event in the transverse plane.

Since the τ is unobserved, the ρ must take its place in the kinematics analysis. The ρ has the best estimation of the τ momentum, but because of the undetected ν_τ it is only a very rough approximation.

Comparing Fig. 3.9 with Figs. 3.6b,d illustrates the differences between $\tau \rightarrow \rho$ events and standard ν_μ CC and NC events. The missing momentum in $\tau \rightarrow \rho$ events is larger than in ν_μ CC, but smaller than in NC events. $\phi_{\ell h}$ for $\tau \rightarrow \rho$ events is larger than it is in NC, but smaller than in CC. Likewise, ϕ_{mh} tends toward large angles in $\tau \rightarrow \rho$, unlike the flat CC distribution, but not as much as in NC events. Figure 3.10 shows the ϕ–ϕ and ρ–ρ plots for $\tau \rightarrow \rho$ Monte Carlo events, which should be compared to Figs. 3.7 and 3.8.

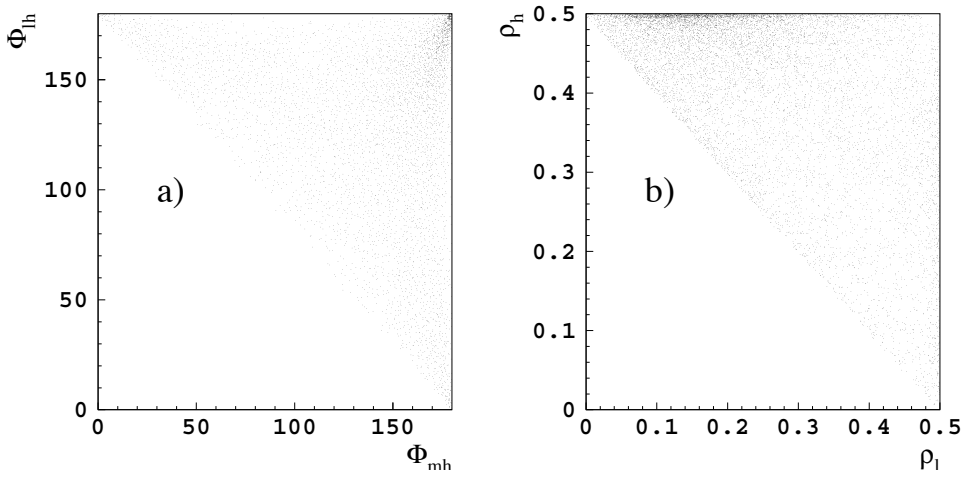

Figure 3.10: a) $\phi_{\ell h}$ vs. ϕ_{mh} and b) ρ_h vs. ρ_ℓ for a sample of Monte Carlo $\tau \rightarrow \rho$ events.

3.2.3 Multidimensional likelihood analysis

The traditional method of selecting $\tau \rightarrow \rho$ events based on their kinematics involves making cuts on a number of variables to increase the overall signal-to-background (S/B) ratio. This can be a tedious procedure as the number of variables increases, and it does not guarantee an optimal set of cuts. In many cases the variables are correlated, and the region of optimal S/B may have a complicated shape, possibly even being composed of more than one distinct phase-space volume.

An alternative, simplifying procedure is the construction of a likelihood measure. In probability theory the likelihood, $\mathcal{L}_0$, for a set of measurements $\{x_i\}$ taken from the probability density functions $f_i(x)$ is just the joint probability density:

$$\mathcal{L}_0 = \prod_{i=1} f_i(x_i). \tag{3.7}$$

In the method of maximum liklihoods, the p.d.f.'s are taken to be a single, parameterizable function $f(x;\vec{\alpha})$, with unknown parameters $\vec{\alpha}$. Then, the optimal parameters are found by solving the likelihood equation

$$\frac{\partial \ln \mathcal{L}_0}{\partial \alpha_i} = 0. \tag{3.8}$$

One could also define a confidence region in the parameter space defined by the elements α_i, by making a threshold cut on the value of $\mathcal{L}_0$.

A similar method, directly based on the method of likelihoods, can be used to separate signal from background in any multidimensional phase space as long as the signal

and background p.d.f.'s are known. The new likelihood measure is

$$\mathcal{L}(x) = \frac{f_S(x)}{f_B(x)}. \tag{3.9}$$

A threshold cut on $\mathcal{L}$ isolates regions of phase space with high S/B ratios, and effectively turns the n-dimensional problem into a single dimensional one. Equivalently, one could cut on the natural log of $\mathcal{L}$, $\ln \mathcal{L} = \ln f_S(x) - \ln f_B(x)$, if that is easier to construct.

In practice, the p.d.f.'s for the signal and background are non-analytical. With a Monte Carlo simulation of the populations, however, they can be modelled statistically. This is the method [136] employed in this analysis. The phase space is binned and the bins are filled with Monte Carlo simulated $\tau \to \rho$ events for the signal and non-ν_τ CC and NC events for the backgrounds. Each background contribution is weighted for the relative abundance expected in the experiment. The signal and background arrays are both normalized to one event per bin. $\mathcal{L}$ thus becomes a discrete function, with a single averaged value in each bin.

The likelihood functions are relied on heavily in this analysis. After loose ρ identification cuts and event quality cuts, the last cut is on the likelihood variable. This cut is reserved for most of the signal discrimination.

3.2.3.1 Defining the signal "box"

At the beginning of this chapter it was noted that this analysis was performed blindly, and that a region of phase space was predefined as the signal "box". This box is prescribed by the likelihood measure $\ln \mathcal{L}$. Since the signal-to-background ratio is larger than unity for positive log-likelihood values, these events could be described as signal-like while events with $\ln \mathcal{L} < 0$ could be called background-like. The signal box for this analysis includes all signal-like events, $\ln \mathcal{L} > 0$.

Seven bins were defined in this signal region, in order to take advantage of our knowledge of the $\ln \mathcal{L}$ distribution. The size of the bins was chosen to balance the desire for fine bin granularity against the need for sufficient signal statistics in each bin. The bins were defined at half-integer intervals from $0 < \ln \mathcal{L} \leq 3$, with the seventh bin including all events with $\ln \mathcal{L} > 3$. Each bin includes several hundred Monte Carlo signal events so the statistical error in each bin is small.

The cuts described in this chapter were tuned using the Monte Carlo $\tau \to \rho^-$ sample, the Monte Carlo background samples searching for both ρ^- and ρ^+, the ρ^+ sample in the data, and the data events with a ρ^- and $\ln \mathcal{L} < 0$ only. Only when the cuts were finalized on these samples "outside the box" was the box opened. Chapter 4 presents the results when the cuts in this chapter are applied to those data events with a negative ρ and $\ln \mathcal{L} > 0$.

3.2.3.2 Likelihood array smoothing

The statistical precision with which the p.d.f.'s can be known is limited by the number of Monte Carlo events available. If the density of events is sufficiently high throughout phase space, one can simply take the number of events in each bin as an approximation of the function in that bin. If the number of events is low and/or there are large regions of phase space with few events, another method is needed.

The technique [136] used in this thesis is to smooth the distributions by calculating a local event density for each bin. To get the local event density for a bin one counts the events in ever-expanding hyperspheres around the given bin until the number of events enclosed by the sphere is above some threshold[4]. The density is the number of events enclosed divided by the volume of the hypersphere. This is repeated for each bin, and the resulting distribution is called the smoothed likelihood.

For distributions in which the density of events is high, such that the number of events in each bin is larger than the threshold, this procedure reduces to counting the number of events in each bin as desired. Its real power is in smoothing sparsely populated distributions, for which purpose it was chosen.

3.2.3.3 Parameterizing events in NOMAD

The kinematics of any event in NOMAD can be completely described by a suitable choice of five independent variables. The lepton and hadron momentum vectors contain all the kinematic information that is available in an event, and they can each be described by three components (p_x, p_y, and p_z, for example). One of these six degrees of freedom is lost, however, through the azimuthal rotational symmetry of the neutrino beam, and we are left with only five: three transverse variables and two longitudinal ones.

Any five suitably independent variables can be chosen to span the space. In this analysis the following five are chosen: the inelasticity y, $Q_\perp$, transverse mass $M_\perp$, $\hat{\mu}$, and $\hat{\nu}$. They are each described below. Although there is some correlation between these variables, they are sufficiently independent to span the available space. y and $Q_\perp$ are the predominantly longitudinal variables, and $M_\perp$, $\hat{\mu}$, and $\hat{\nu}$ are the transverse ones.

The inelasticity is just the fraction of the incident neutrino's energy imparted to the hadron vector. In NOMAD, this is defined as the ratio of the hadron jet energy to the total observed energy in the event (hadron plus lepton). In a CC event in which the outgoing lepton is observed, the total energy in the event is equal to the incident neutrino energy and the formula representrs the true inelasticity. In a NC event the outgoing lepton escapes undetected, so the total event energy is only the energy of the hadron jet. y is still calculated in NC events, but it does not correspond to the true inelasticity.

[4]The threshold used in this analysis was 16 events, for a statistical precision of 25%.

$Q_\perp$ [134] is the transverse momentum of the chosen lepton with respect to the total event momentum vector in three-space. It is defined by

$$Q_\perp^2 = P_\ell^2 - \left(\frac{\vec{P_\ell} \cdot \vec{P_{tot}}}{P_{tot}} \right)^2 , \tag{3.10}$$

where the momenta $\vec{P_\ell}$ and $\vec{P_{tot}}$ are the three-space[5] momentum vectors for the lepton and for the total energy (lepton + hadron jet) in the event, respectively. $Q_\perp$ is bound by zero at its lower end, but it is unbounded on the upper end. In constructing bins for $Q_\perp$, then, the highest bin has no upper bound.

$M_\perp$ is the transverse mass for an event, defined by

$$\begin{aligned} M_\perp^2 &= (P_\ell + P_m)^2 - (\vec{P_\ell} + \vec{P_m})^2 \\ &= (P_\ell + P_m)^2 - P_h^2 \\ &= 2(P_\ell P_m - \vec{P_\ell} \cdot \vec{P_m}) \\ &= 4 P_\ell P_m \sin^2(\phi_{\ell h} + \phi_{mh}), \end{aligned} \tag{3.11}$$

where all vectors are defined in the beam transverse plane. $M_\perp$ is a measure of the invariant mass of the lepton–missing-momentum system, the system recoiling against the hadron jet. In a ν_τ CC event, the missing momentum will largely belong to the escaping ν_τ, the daughter of the τ. Thus, if the τ momentum were entirely in the transverse plane, $M_\perp$ would represent the τ mass; instead, it has an upper bound at the mass of the τ.

$\hat{\mu}$ and $\hat{\nu}$ [135] are constructed from the variables ρ_ℓ, ρ_h, and ρ_m, introduced in Sec. 3.2.1. They convey the same transverse information as those former variables, but $\hat{\mu}$ and $\hat{\nu}$ are constructed to cover a rectangular region instead of a triangular one, and this makes the multidimensional binning easier. The definitions of $\hat{\mu}$ and $\hat{\nu}$ are:

$$\hat{\mu} = 1 - 2\rho_h \tag{3.12}$$

$$\hat{\nu} = \frac{\rho_\ell - \rho_m}{\rho_h}. \tag{3.13}$$

$\hat{\mu}$ takes on values from 0 to 1, and $\hat{\nu}$ covers [-1,1].

Each variable is broken into 16 bins, for a total of 1,048,576 bins. The bin sizes were made variable so that the number of signal events in each bin would be more uniform across each variable. Table 3.2 shows the values of the low edges of each bin. With only a small number of events to populate the bins, such that smoothing across several bins is necessary, the results are not very sensitive to the precise locations of the bin boundaries.

[5] Note the difference from the definitions in Sec. 3.2.1, where P_ℓ referred to the *transverse* momentum.

Bin	y	$Q_\perp$	$M_\perp$	$\hat{\mu}$	$\hat{\nu}$
1	0.0000	0.00	0.00	0.000	-1.00
2	0.0625	0.75	0.50	0.005	-0.99
3	0.1250	1.25	1.00	0.020	-0.95
4	0.1875	1.50	1.25	0.050	-0.90
5	0.2500	1.75	1.50	0.100	-0.80
6	0.3125	2.00	1.75	0.175	-0.60
7	0.3750	2.25	2.00	0.250	-0.40
8	0.4375	2.50	2.25	0.325	-0.20
9	0.5000	2.75	2.50	0.400	0.00
10	0.5625	3.00	3.00	0.475	0.20
11	0.6250	3.50	3.50	0.550	0.40
12	0.6875	4.00	4.00	0.625	0.60
13	0.7500	4.50	4.50	0.700	0.80
14	0.8125	5.50	5.50	0.775	0.90
15	0.8750	7.00	7.00	0.850	0.95
16	0.9375	10.00	10.00	0.925	0.99

Table 3.2: Bin definitions (low edges are displayed) for the likelihood array.

Sample	Odd Array	Even Array
$\tau \to \rho$	6104	6130
ν_μ NC	902	857
ν_μ CC	89	81
$\overline{\nu}_\mu$ CC	13	9
ν_e CC	149	156
$\overline{\nu}_e$ CC	80	73

Table 3.3: Numbers of entries from each category of Monte Carlo event in the likelihood arrays.

The signal array is easy to construct. After selecting ρ^- candidates and applying the event quality cuts (cf. Sec. 3.3), all surviving events are entered into their appropriate bins and the array is smoothed à la Sec. 3.2.3.2.

The background array requires more care since there are several types of backgrounds that need to be combined. After event cuts and selecting ρ^- candidates, events are entered into bins with weights according to their event type. The weights can be read from the third column of Tab. 2.5. The array is then renormalized, such that the contents of the bin with the smallest non-zero entry is equal to 1, and smoothed as in the signal case.

In order to avoid overlap between the events used to construct the likelihood functions and the events analyzed by them, all Monte Carlo events were separated into two groups. The events from each group were used to construct separate likelihood functions, and these functions were used to measure the opposite group. Since the groups were arbitrary, the parity of the event number was used to classify events. Thus, the odd numbered $\tau \to \rho$ events went into the formation of the "odd" signal array, the even events defined the "even" signal array, and likewise for the background arrays. Then, during the final analysis, even events were compared with the odd signal and background functions to get a likelihood measure, and vice versa for the odd events. Table 3.3 shows the number of entries by Monte Carlo type in each of the four likelihood arrays (signal and background, odd and even).

3.3 Event Quality Cuts

Because this $\tau \to \rho$ analysis relies so heavily on kinematics, proper event reconstruction is paramount. Therefore, events with any signs of poor reconstruction are vetoed immediately. In addition, most ν_μ and ν_e CC events can be rejected by identifying the leading lepton. This section details the cuts used to remove such unwanted events.

3.3.1 Reconstruction checks

Low energy charged particles tend to spiral in on themselves in the field of the magnet, leaving a pattern of hits that the track reconstruction algorithm often mishandles. Such POs often appear with inaccurate momentum information and only few hits; however, this does not reflect any gross reconstruction breakdown. Because the error on the total event energy introduced by these low energy tracks is small, such tracks can be neglected without much loss of kinematic information. Therefore, tracks with less than 10 DC hits are "locked out", meaning that they are not considered in any further part of the analysis for that event[6]. In addition, tracks with less than 12 hits are locked if they have a momentum $p < 1$ GeV and a track fit χ^2 per degree of freedom of more than 5.

Other track reconstruction problems can lead to more serious kinematic errors in an event. If the uncertainties obtained by the track fitting procedure are large (≥ 10 GeV/c in momentum, ≥ 0.5 GeV/c in transverse momentum, or χ^2/d.o.f. ≥ 10) for any track in an event, that event is vetoed. Likewise, if the total number of DC hits that are not assigned to any tracks is large (>500), this also suggests poor reconstruction and the event is rejected.

The position of the primary neutrino–nucleon interaction vertex determines the momentum directions for all of the neutral POs in an event. If it is mismeasured, or if the wrong vertex is chosen as the primary one, then the energy vectors could be badly in error. With this in mind, the primary vertex is required to contain at least two tracks, and the sum of the charges of the tracks in the PVTX is required to lie within one unit of electric charge from zero. In a CC event, the total charge should be zero, whereas in a NC the charge could be zero or one depending on whether the struck nucleon is a proton or neutron.

The PVTX can also provide a way to remove events originating outside the detector. Neutrino interactions in the material surrounding the DCs can generate particles which stray into the fiducial volume, triggering the $\overline{V} \times T_1 \times T_2$ trigger. These events will appear to originate on one of the boundaries of the detector. Of particular concern is the magnet and iron return yoke surrounding the sides of the target, and the FCAL in front of the DCs. So, the position of the PVTX is required to lie in the range [-130,130] cm in x, [-125,135] in y, and [5,403] in z. This provides at least a 15 cm cushion around the sides of the DC area, and 5 cm regions at the front and back. The asymmetry in y is to account for the neutrino beam tilt (cf. Sec. 2.2.1).

Finally, POs can pass through the ECAL from sources outside the event. Since the calorimeter includes timing information, though, the vast majority of such occurrances can be identified by rejecting events with ECAL energy outside the event timing window. If the total out-of-time energy in the ECAL is greater than 100 MeV the event is vetoed.

[6] POs that are locked in an event do not contribute to any of the kinematic sums, for instance.

3.3.2 Electron veto

Though not as prevalent as ν_μ CC, ν_e CC events pose a significant potential background to this analysis. The π^- daughter of the ρ^- is required to pass electron veto cuts (cf. Sec. 3.1.3.1), but a leading electron may exist elsewhere in an event.

Primary electron identification is done through the ECAL/TRD/PRS subdetectors. If an electron travelled on a trajectory such that it missed them, it would not be identified as an electron. In order to ensure that leading electrons do hit them, therefore, any track with a transverse momentum ≥ 0.8 GeV/c is required to project into the fiducial volume of the ECAL. If any track in an event fails this requirement, it could be a leading electron, so the event is discarded.

Leading electrons are recognized through a combination of kinematics and particle identification. For the particle identification, two electron definitions are used: tight and loose. The tight definition is the standard definition used in Sec. 3.1.3.1. Since the non-electron contamination should be less than 0.1% in this sample, it is safe to add the Bremsstrahlung strip energy to the momenta of POs satisfying this definition.

Tracks in the loose vertex are identified as loose electrons if they have any "daughter" tracks that are identified as electrons. A daughter track is one whose starting point matches with the endpoint of its parent track. The track from a charged particle which undergoes an interaction in the detector may have several daughter tracks, for example. The helix of an electron which emits a Bremsstrahlung photon will have a discontinuity, and it may be reconstructed as two separate POs. Only the "daughter" PO will have any TRD/PRS/ECAL information, though, and the loose electron definition is designed to catch such a case.

Loose vertex tracks will also satisfy the loose electron requirements if any two of the following three hold:

- The TRD variable ELACC < 0.99
- The PRS energies PRSEV + PRSEH > 20 MIPs
- $\frac{E-P}{E+P} > -0.1$

See Sec. 3.1.3.1 for the variable definitions. If either of the first two conditions hold, but not the third, then the Bremsstrahlung strip energy is temporarily added to the PO and the third condition is retested.

Since POs passing the loose electron cuts may have higher pion contaminations, the Bremsstrahlung strip energy is not added to their track momenta in the leading particle determination, discussed next.

A PO is considered a possible leading particle for the purpose of electron rejection if it has a transverse momentum $P_\perp > 0.8$ GeV/c, or if it has the highest value of any of the following quantities in an event: momentum p, transverse momentum $P_\perp$, isolation

I (cf. Sec. 3.1.4), $Q_\perp$(Sec. 3.2.3.3), or Q_ℓ. Q_ℓ is defined similarly to $Q_\perp$; it is the transverse momentum of the lepton with respect to the hadron vector:

$$Q_\ell^2 = P_\ell^2 - \left(\frac{\vec{P}_\ell \cdot \vec{P}_h}{P_h} \right)^2 . \tag{3.14}$$

As there are may be several POs in an event which satisfy different criteria above, there may be more than one "leading particle"[7] found in an event.

If any charged track in an event satisfies either of the electron definitions and also satisfies any of the kinematic requirements, it is considered a leading electron and the event is vetoed.

3.3.3 Muon veto

Whereas electrons are commonly found in the hadron jet of an event, most muons are the leading leptons from ν_μ (or $\overline{\nu}_\mu$) CC events. Since the ν_μ background is also potentially much larger than the ν_e background, any event with a muon candidate in it is rejected for this $\tau \to \rho$ analysis regardless of the event kinematics.

A charged track is a muon candidate if any of the following apply:

- the reconstruction package matches the DC track with a muon chamber track segment (phase II muon),
- the track has a single daughter which matches to a muon chamber track segment,
- the projected DC track comes within 40 cm of hits in x and y planes of muon chambers in station 1, or within 50 cm in station 2 (loose muon),
- the track is a muon catastrophe.

Most of these are similar to the cuts made in Sec. 3.1.3.2.

In addition, any event with a "shadow muon" is also rejected. A shadow muon is a muon which presumedly comes from the interior of the detector, but for which there is no corresponding DC track. This may happen in, e.g, a high multiplicity event in which the muon DC track is not reconstructed properly. The hits in the muon chambers may form a track segment with direction information. A shadow muon is a muon chamber track segment which projects back into the DC region.

Along with the neutrinos in the beam, many accompanying muons pass straight through the NOMAD detector. These are called halo muons, and their presence should not cause an event to be vetoed. This is actualized by requiring a shadow muon track

[7] This definition of a leading particle is only used in the electron veto. It is different from that used in the $\tau \to \rho$ search.

segment to lie within a box defined by $|x|, |y| < 250$ cm at the muon chambers, or to project backwards to inside a box of $|x|, |y| < 200$ cm at $z = 0$. Halo muons will generally begin outside the box at $z = 0$ and travel along the beam direction. Halo muons inside the box at $z = 0$ will hit the veto planes in front of the detector, and the event will not be triggered by $\overline{V} \times T_1 \times T_2$.

3.4 Monte Carlo Systematic Effects

The oscillation probability derived from this analysis is dependent on the signal and background efficiencies. These are measured by the Monte Carlo, so the accuracy of the efficiencies is directly dependent on the degree to which the Monte Carlo reflects the data. Controlling systematic errors in the Monte Carlo is therefore an important task.

The greatest uncertainty in the Monte Carlo description of the $\nu - N$ interaction is in the nuclear fragmentation, which gives rise to the hadron jet. Thus, signals which rely on a detailed description of the hadronic part of events will suffer most from inaccurate representations in the Monte Carlo. The most obvious of these is the NC background, in which the entire visible energy comes from nuclear fragmentation. The $\tau \rightarrow \rho$ signal is less affected since it relies only on the total hadronic momentum vector, which is determined by kinematics, and not on a detailed description of the jet. CC backgrounds fall somewhere in the middle, relying on hadronic particles to form the π^0 but sometimes incorporating the leading lepton into the "ρ^-".

3.4.1 Data simulator

In order to minimize the systematic errors introduced by the Monte Carlo, a data simulator approach is used in this analysis. Kinematically, a ν_μ CC event is very similar to a NC or a ν_τ CC event. The main difference is the identity of the leading lepton. The data simulator uses this similarity to derive samples of "fake NC" and "τ signal" directly from the ν_μ data themselves. No such technique exists to minimize the systematic error for the CC backgrounds.

The procedure for generating fake NC events is as follows. Reconstructed events are accepted for the simulator if they have one and only one μ^-. In order to avoid identification errors of either kind, the muon is required to pass a tight set of cuts, and no other track (of either charge) in the event is allowed to pass even loose muon cuts. This muon is removed from the event, and analysis proceeds as normal. The only difference for the data simulator analysis is that the event muon veto cuts of Sec. 3.3.3 are not applied, as these would be mutually exclusive with the data simulator requirements. Removing the leading μ^- simulates the behavior of the undetected ν in a NC event.

A PO passes the tight muon cuts if it has a momentum of more then 2.5 GeV/c, and its projected track matches to a track segment in either station of the muon chambers.

A match in station 1 is defined as a spatial proximity of ≤ 40 cm and a χ^2 for the track match of $\leq$20 (for 4 degrees of freedom). A PO will pass the loose muon cuts if it is matched to hits in both planes of either muon station or in the muon veto, or if it satisfies the muon catastrophic energy loss test described in Sec. 3.1.3.2.

The procedure for generating ν_τ simulated events is the same until the last step. Instead of simply removing the found muon in an event, its momentum vector is used to construct a τ PO. The momentum is rescaled [137] to account for the expected difference in the energy spectra between ν_μ CC and ν_τ CC events due to the difference in the lepton masses. The $\tau \rightarrow \rho$ decay chain is simulated, and only the final state particles ($\pi^- \gamma\gamma$) are kept. Their momenta are smeared to account for the detector resolution, and they are placed in the list of reconstructed POs in the event. The function used to smear the momentum of charged tracks is the measured DC resolution (Eq. 2.1). Photons are smeared by an amount

$$\frac{\Delta E}{E} = (3.2 \pm 0.1)\%. \tag{3.15}$$

The advantage of the data simulator procedure is that it allows one to estimate the systematic differences between the data and Monte Carlo. The same procedure can be performed on both real data and on ν_μ CC Monte Carlo events. For N^{sim}_{data} simulated events from the data and N^{sim}_{MC} simulated events in the Monte Carlo, if N^{sel}_{data} and N^{sel}_{MC} events are selected by the analysis, the data simulator efficiencies are

$$\epsilon^{data}_{DS} = \frac{N^{data}_{sel}}{N^{data}_{sim}} \tag{3.16}$$

$$\epsilon^{MC}_{DS} = \frac{N^{MC}_{sel}}{N^{MC}_{sim}}. \tag{3.17}$$

If the same analysis produces an efficiency in the regular (not data simulated) Monte Carlo of ϵ^{MC}_{sig} for the $\tau \rightarrow \rho$ signal and ϵ^{MC}_{bak} for the NC background, then the expected efficiencies for the data are:

$$\epsilon^{data}_{sig} = \epsilon^{MC}_{sig} \left(\frac{\epsilon^{data}_{DS}}{\epsilon^{MC}_{DS}} \right)_{\tau\rightarrow\rho} \tag{3.18}$$

$$\epsilon^{data}_{bak} = \epsilon^{MC}_{bak} \left(\frac{\epsilon^{data}_{DS}}{\epsilon^{MC}_{DS}} \right)_{fakeNC}. \tag{3.19}$$

For ease of notation, let the ratios of efficiencies in Eqs. 3.18 and 3.19 be represented by

$$f^{DS}_i \equiv \left(\frac{\epsilon^{data}_{DS}}{\epsilon^{MC}_{DS}} \right)_i \quad , \quad i = sig, bak. \tag{3.20}$$

Sample	$\tau \to \rho$ Simulator		Fake NC Simulator	
	Data	MC	Data	MC
DST Events	3324927	5032958	3324927	5032958
Simulated Events	899252	2978242	1002656	3216394
$\tau \to \rho$ Candidates	76738	487910	19	10
$\ln \mathcal{L} \leq 0.0$	19848	126126	10	7
$\ln \mathcal{L} > 0.0$	56890	361784	9	3
$0.0 < \ln \mathcal{L} \leq 0.5$	5541	34895	4	1
$0.5 < \ln \mathcal{L} \leq 1.0$	7060	45401	0	0
$1.0 < \ln \mathcal{L} \leq 1.5$	7911	50177	2	0
$1.5 < \ln \mathcal{L} \leq 2.0$	8288	52466	0	1
$2.0 < \ln \mathcal{L} \leq 2.5$	8240	53752	2	0
$2.5 < \ln \mathcal{L} \leq 3.0$	7950	50986	0	0
$\ln \mathcal{L} > 3.0$	11872	74107	1	1

Table 3.4: Number of events in the signal ($\tau \to \rho^-$) and background (fake NC) data simulators in bins of the likelihood variable $\ln \mathcal{L}$.

Table 3.4 shows the number of events in the signal and background data simulators for data and Monte Carlo in bins of the likelihood variable $\ln \mathcal{L}$. The background (fake NC) bins contain the sum of the events in which a ρ^- is found and the events in which an equivalent ρ^+ is found. (See Sec. 3.4.2 and appendix A.)

f_{sig}^{DS} is calculated for each bin and reported in Tab. 3.5. The errors are the Poisson errors for the number of events observed.

From Tab. 3.4 it is evident that the number of surviving events in the fake NC data simulator is insufficient to calculate a statistically meaningful value of f_{DS}^{i} separately for each likelihood bin. One simple approach is to set the value for each bin equal to the average over the whole likelihood region $\ln \mathcal{L} > 0.0$. This yields

$$f_{DS}^{bak} = \frac{9/1002656}{3/3216394} = 9.6^{+4.3}_{-5.7}, \tag{3.21}$$

where the errors are statistical only, and derive from the 34% confidence regions on each side of the Poisson-distributed numbers of events.

Another approach is to fit the data to a simple function in each of the likelihood bins defined in Tab. 3.4 for $\ln \mathcal{L} > 0$. Since there are very few entries in each bin, a

Sample	f_{sig}^{DS}
$\tau \to \rho$ Candidates	0.5209 ± 0.0021
$\ln \mathcal{L} \leq 0.0$	0.5212 ± 0.0040
$\ln \mathcal{L} > 0.0$	0.5208 ± 0.0024
$0.0 < \ln \mathcal{L} \leq 0.5$	0.5259 ± 0.0076
$0.5 < \ln \mathcal{L} \leq 1.0$	0.5150 ± 0.0066
$1.0 < \ln \mathcal{L} \leq 1.5$	0.5222 ± 0.0063
$1.5 < \ln \mathcal{L} \leq 2.0$	0.5232 ± 0.0062
$2.0 < \ln \mathcal{L} \leq 2.5$	0.5077 ± 0.0060
$2.5 < \ln \mathcal{L} \leq 3.0$	0.5164 ± 0.0062
$\ln \mathcal{L} > 3.0$	0.5306 ± 0.0053

Table 3.5: Ratio of data to Monte Carlo efficiencies for the signal data simulator.

maximum-likelihood fit is performed, where the function to be minimized is [138]:

$$\chi^2 = 2 \sum_i \left[\left(N_i^{fit} - N_i^{MC} \right) + N_i^{MC} \ln \left(\frac{N_i^{MC}}{N_i^{fit}} \right) + \left(f(i) N_i^{fit} - N_i^{data} \right) + N_i^{data} \ln \left(\frac{N_i^{data}}{f(i) N_i^{fit}} \right) \right] . \quad (3.22)$$

The sum is over the 7 bins in the fit, N_i^{data} and N_i^{MC} are the numbers of entries in bin i for the data and MC data simulators, and N_i^{fit} and $f(i)$ are fit parameters. $f(i)$ is taken to be a polynomial acting on the low edge of each bin; for example, f(1) corresponds to a polynomial evaluated at the point $x = 0$, f(2) is the value of the same polynomial evaluated at $x = 0.5$, etc. For Poisson distributed data the χ^2 function of Eq. 3.22 behaves asymptotically like the classical χ^2 in a least-squares fit for the purposes of interval estimation and goodness-of-fit.

The function minimization is done with the MINUIT [139] package (release 96.03). MINUIT uses a variable-metric method with numerically determined first- and second-derivatives to minimize the χ^2 function. The errors on the best-fit parameters are determined by following the χ^2 function from its minimum to $\chi^2_{min} + 1$. This prescription defines a surface in the n-dimensional parameter space, and only the endpoints of the projection of this surface onto a single parameter axis are reported for each parameter. For uncorrolated parameters this gives the correct error, and it overestimates the error otherwise.

For 7 likelihood bins there are 14 independent measurements and $8 + 0$ free param-

eters, where $\mathcal{O}$ is the order of the fitted polynomial. The background data simulator is fitted to polynomials of order 0, 1, and 2, yielding

$$f_{DS}^{bak} = 5.2 \pm 2.2 \quad , \quad \chi^2/\text{d.o.f.} = 4.25/6 \tag{3.23}$$

$$f_{DS}^{bak} = (8.5^{+4.5}_{-3.5}) + (-1.8^{+1.5}_{-1.7})x \quad , \quad \chi^2/\text{d.o.f.} = 2.91/5 \tag{3.24}$$

$$f_{DS}^{bak} = (10.3^{+7.1}_{-4.9}) + (-5.4^{+6.7}_{-7.4})x + (1.0 \pm 1.9)x^2, \chi^2/\text{d.o.f.} = 2.60/4, \tag{3.25}$$

where x is the low edge of the given likelihood bin.

The values are all in agreement with the average calculated earlier, which is not surprising given the large errors. However, the precision of both estimates is insufficient for the purpose of controlling systematics. Because of this, the NC data simulator is not used to estimate f_{DS}^{bak} in this analysis. Instead, the ρ^+ data is used, as explained in the next section.

3.4.2 ρ^+ analysis

Another way to estimate the systematic behavior of the Monte Carlo for the NC backgrounds is to compare the predictions for ρ^+ to the data. There is no danger of looking inside the box prematurely because the ρ^+ and ρ^- data samples are distinct. Even if the same event yields both types of candidates, the event kinematics will be different for each choice of ρ, and so the likelihood measure will be different.

The ρ^+ analysis procedes exactly the same as the ρ^- analysis, except that the sign of the charge of the selected ρ is reversed. All other cuts are the same. Since any $\overline{\nu}_\tau$ component in the beam (from $\overline{\nu}_\mu \rightarrow \overline{\nu}_\tau$ oscillation) should be smaller than the ν_τ component by an order of magnitude, the ρ^+ sample should be entirely background.

It is assumed that the systematic errors are similar for all of the CC types. This way the four CC types may be combined to improve the statistics. It is hypothesized that the primary background to the ρ^- signal from CC events comes when a ρ^- is selected in the hadronic jet. Since this depends on the nuclear fragmentation, and not the lepton, it should be similar for all incident neutrino types.

In addition, if the CC backgrounds come from the hadron jet, the data/Monte Carlo differences should be equivalent for $\rho+$ and ρ^-. Thus, the measured difference in the ρ^+ data should accurately reflect the difference in the ρ^- data. The results are presented in Ch. 4.

Chapter 4

Results and Conclusions

This chapter presents the results from the analysis described in Ch. 3. The signal and background efficiencies are presented, and a limit on the oscillation probability is obtained. Finally, this result is compared with other imits obtained in NOMAD.

4.1 Signal Events and Efficiency

In this sction, the signal efficiency is calculated. This is the probability of this analysis algorithm to select an event given that the event contains a genuine ν_τ CC interaction.

Although this analysis is looking for the combination of particles which form the ρ^- from a τ^- decay, the same set of cuts may also select events from other τ^- decay channels. Since the different events are indistinguishable in this analysis, all modes contribute to the "signal" efficiency. For example, in a ν_τ interaction event in which the lepton undergoes the decay $\tau \rightarrow \pi^+\pi^-\pi^-\nu_\tau$, some set of PO's may collectively satisfy the ρ identification requirements of this analysis. If one or more of the τ-daughter pions are included in this "ρ", the event also has a good chance of satisfying the kinematic selections.

The fraction of all ν_τ CC events identified by this analysis is thus:

$$\epsilon_{\rm sig} = \sum_{\rm i} \epsilon_{\rm i} \times {\rm Br}_{\rm i}, \tag{4.1}$$

where i refers to the τ decay channels, $\epsilon_{\rm i}$ is the efficiency of this analysis on events from the $\rm i^{th}$ channel, and ${\rm Br}_{\rm i}$ is the branching fraction of decay channel i. In Monte Carlo samples of 3000 $\tau^- \rightarrow \mu^-\nu_\tau$ events and 269975 $\tau^- \rightarrow e^-\nu_\tau$ events, no ρ candidates were found, so these channels are dropped from the sum.

The other ν_τ CC Monte Carlo event samples generated by the collaboration were the 1-prong and 3-prong hadronic decay channels. In addition, a small sample of inclusive ν_τ CC events was also generated to be used as a cross check. Table 4.1 lists the number

of events in each of these three samples in bins of the likelihood variable $\ln \mathcal{L}$. (Recall that the signal box for this analysis includes all bins with $\ln \mathcal{L} > 0$.)

The relevant quantity for the signal efficiency is $\epsilon \times \mathrm{Br}$, according to Eq. 4.1. The branching fraction [28] for the τ 1-prong hadronic decays is $(42.52 \pm 0.16)\%$, and the branching fraction for the 3-prong modes is $(15.18 \pm 0.13)\%$. Table 4.2 lists the net efficiencies for the 1-prong and 3-prong hadronic decays modes, and their sum. The sums may be compared with the "Inclusive" efficiency from Tab. 4.1, since the branching fraction in this channel is unity by definition. Finally, Tab. 4.3 shows the net τ^- efficiency (from Tab. 4.2) corrected for the data/Monte Carlo biases (cf. Tab. 3.5).

4.2 Background Contamination

Similarly to the signal efficiency, one must know the number of expected background contamination events in order to calculate an oscillation probability. A background contamination event is a non-ν_τ-CC event in which all the signal requirements from Ch. 3 are nonetheless satisfied.

There are five types of backgrounds important to this study (ν_μ CC, $\overline{\nu}_\mu$ CC, ν_e CC, $\overline{\nu}_e$ CC, and NC), and each type is analyzed separately. The number of expected contamination events in likelihood bin i from background type α can be written

$$N_{i,\alpha}^{\mathrm{exp}} = \frac{N_{i,\alpha}^{\mathrm{MC}}}{F_\alpha} f_\alpha^{\mathrm{DS}} \tag{4.2}$$

where $N_{i,\alpha}^{\mathrm{MC}}$ is the number of contamination events surviving in bin i of a Monte Carlo sample with $N_{\mathrm{tot},\alpha}^{\mathrm{MC}}$ α-type events, F_α is a normalization constant, and f_α^{DS} is the data simulator correction factor for background α.

The normalization factor is just the factor by which the total number of Monte Carlo events (of background type α) exceeds the expected number in the data:

$$F_\alpha = \frac{N_{\mathrm{tot},\alpha}^{\mathrm{MC}}}{N_{\mathrm{tot},\alpha}^{\mathrm{exp}}}. \tag{4.3}$$

Since NOMAD collects large numbers of ν_μ CC events, it is convenient to measure well that one rate in the detector and scale the other background types by their known *relative* rates (r_α) with respect to the ν_μ CC rate. Thus, $N_{\mathrm{tot},\alpha}^{\mathrm{exp}}$ becomes

$$N_{\mathrm{tot},\alpha}^{\mathrm{exp}} = r_\alpha N_\mu \tag{4.4}$$

with r_α determined by the beam Monte Carlo (NUBEAM).

The ρ^- analysis of Ch. 3 is applied to the background Monte Carlo samples to get

Sample	τ^- 1-prong		τ^- 3-prong		Inclusive τ^-	
	Number	Efficiency ($\times 10^6$)	Number	Efficiency ($\times 10^6$)	Number	Efficiency ($\times 10^6$)
DST Events	637808	N/A	1167604	N/A	31873	N/A
$\tau \to \rho$ Candidates	5925	9290 ± 120	1252	1070 ± 30	155	4900 ± 400
$\ln \mathcal{L} \leq 0.0$	130	204 ± 18	65	56 ± 7	6	190^{+110}_{-80}
$\ln \mathcal{L} > 0.0$	5795	9090 ± 120	1187	1020 ± 30	149	4700 ± 400
$0.0 < \ln \mathcal{L} \leq 0.5$	179	280 ± 20	69	59 ± 7	2	60^{+80}_{-40}
$0.5 < \ln \mathcal{L} \leq 1.0$	389	610 ± 30	89	76 ± 8	9	280^{+130}_{-90}
$1.0 < \ln \mathcal{L} \leq 1.5$	601	940 ± 40	144	123 ± 10	18	560 ± 130
$1.5 < \ln \mathcal{L} \leq 2.0$	809	1270 ± 40	185	158 ± 12	26	820 ± 160
$2.0 < \ln \mathcal{L} \leq 2.5$	1033	1620 ± 50	221	189 ± 13	30	940 ± 170
$2.5 < \ln \mathcal{L} \leq 3.0$	1294	2030 ± 60	226	194 ± 13	39	1220 ± 200
$\ln \mathcal{L} > 3.0$	1490	2340 ± 60	253	217 ± 14	25	780 ± 160

Table 4.1: Numbers of Monte Carlo events selected in the $\tau \to \rho^-$ analysis. The errors are statistical only.

Sample	Efficiency × Branching Fraction ($\times 10^6$)		
	τ^- 1-prong	τ^- 3-prong	Sum
$\tau \to \rho$ Candidates	4600 ± 60	163 ± 5	4760 ± 60
$\ln \mathcal{L} \leq 0.0$	101 ± 9	8 ± 1	109 ± 9
$\ln \mathcal{L} > 0.0$	4500 ± 60	154 ± 5	4650 ± 80
$0.0 < \ln \mathcal{L} \leq 0.5$	139 ± 10	9 ± 1	148 ± 10
$0.5 < \ln \mathcal{L} \leq 1.0$	302 ± 15	12 ± 1	314 ± 15
$1.0 < \ln \mathcal{L} \leq 1.5$	467 ± 19	19 ± 2	486 ± 19
$1.5 < \ln \mathcal{L} \leq 2.0$	628 ± 22	24 ± 2	652 ± 22
$2.0 < \ln \mathcal{L} \leq 2.5$	802 ± 25	29 ± 2	831 ± 25
$2.5 < \ln \mathcal{L} \leq 3.0$	1000 ± 30	29 ± 2	1030 ± 30
$\ln \mathcal{L} > 3.0$	1160 ± 30	33 ± 2	1190 ± 30

Table 4.2: Efficiencies multiplied by branching fractions for the hadronic 1-prong and 3-prong τ decay samples, and the sum of the two. The errors are dominated by statistics.

Sample	$\epsilon_\tau \times$ Br ($\times 10^6$)
$\tau \to \rho$ Candidates	$2480^{+26.5}_{-13.5}$
$\ln \mathcal{L} \leq 0.0$	$57^{+4.1}_{-0.5}$
$\ln \mathcal{L} > 0.0$	$2420^{+26.6}_{-14.2}$
$0.0 < \ln \mathcal{L} \leq 0.5$	$78^{+4.5}_{-1.2}$
$0.5 < \ln \mathcal{L} \leq 1.0$	$162^{+6.7}_{-2.2}$
$1.0 < \ln \mathcal{L} \leq 1.5$	$254^{+8.9}_{-3.2}$
$1.5 < \ln \mathcal{L} \leq 2.0$	$341^{+8.9}_{-4.2}$
$2.0 < \ln \mathcal{L} \leq 2.5$	$422^{+10.9}_{-5.2}$
$2.5 < \ln \mathcal{L} \leq 3.0$	$534^{+13.3}_{-6.7}$
$\ln \mathcal{L} > 3.0$	$631^{+13.6}_{-6.7}$

Table 4.3: Summed efficiencies multiplied by branching fractions for the Monte Carlo τ^- samples, corrected by the signal data simulator. The errors are statistical and systematic, respectively, where the systematic errors include the branching fraction uncertainty and the error due to the data/MC correction.

Sample	NC	ν_μ CC	$\overline{\nu}_\mu$ CC	ν_e CC	$\overline{\nu}_e$ CC
DST Events	3067890	5032958	588732	2157453	296974
$\tau \to \rho$ Candidates	174	18	7	58	57
$\ln \mathcal{L} \leq 0.0$	109	0	0	4	0
$\ln \mathcal{L} > 0.0$	65	18	7	54	57
$0.0 < \ln \mathcal{L} \leq 0.5$	10	0	0	4	2
$0.5 < \ln \mathcal{L} \leq 1.0$	8	4	0	4	6
$1.0 < \ln \mathcal{L} \leq 1.5$	7	4	0	6	10
$1.5 < \ln \mathcal{L} \leq 2.0$	17	3	4	3	11
$2.0 < \ln \mathcal{L} \leq 2.5$	10	3	1	5	11
$2.5 < \ln \mathcal{L} \leq 3.0$	8	3	2	19	6
$\ln \mathcal{L} > 3.0$	5	1	0	13	11

Table 4.4: Numbers of Monte Carlo events selected in the $\tau \to \rho^-$ analysis applied to the background samples.

$N_{i,\alpha}^{MC}$ in Sec. 4.2.1, the normalization constant F_α is constructed in Sec. 4.2.2, and the data simulator correction for the *background* is determined from the ρ^+ analysis (unlike the data simulator for the *signal*) in Section 4.2.3.

4.2.1 Background Monte Carlo events

Table 4.4 lists the number of background Monte Carlo candidate events that are chosen in the ρ^- background analysis as a function of the $\ln \mathcal{L}$ cut. Of the CC events listed, only two of the ν_e CC events had the leading lepton incorporated into the definition of the ρ^-, this small percentage supporting the rationale for using the ρ^+ events discussed in Sec. 3.4.2. In order to convert the numbers of Monte Carlo events in Tab. 4.4 into an expected background for the ρ^- data, the relative efficiency of each neutrino species must be normalized to the size of the respective data sample and corrected for the data/Monte Carlo difference.

4.2.2 Event normalization

The relative contributions from NC interactions and the four types of CC interactions (ν_μ, $\overline{\nu}_\mu$, ν_e, $\overline{\nu}_e$) are given by the neutrino beam Monte Carlo, NUBEAM (Tab. 2.3).

The absolute normalization (the total flux of ν_μ CC events) is set by the data themselves. The number of ν_μ CC events is measured in the data and Monte Carlo with a set of simple requirements so that any bias introduced is minimal. The total number of

ν_μ CC events in the data is then given by

$$N_\mu = N_\mu^{obs} / \epsilon_\mu^{MC}. \tag{4.5}$$

To a good approximation a ν_μ CC event in NOMAD is any event with a muon in it; every ν_μ CC event contains a muon, and muon production in hadronic jets is relatively rare. The approximation does not have to be exact since any inefficiency or contamination of the signal should be mimicked by the Monte Carlo. However, since there is no procedure like the data simulator to estimate the biases between the data and Monte Carlo for ν_μ CC events, three different ν_μ CC definitions are used, and the N_μ is averaged among them.

One definition has already been encountered in constructing the data simulator (cf. Sec. 3.4.1). The other two definitions are looser and tighter variations on that same theme. The looser definition requires the same fiducial volume requirements of the primary vertex (cf. Sec. 3.3.1), and at least one match between a negatively charged DC track and a muon chamber track segment (phase II muon). The looser definition aims for inclusivity at the expense of purity.

The tighter ν_μ CC requirements try to maximize the purity of the selected sample, but must compromise the efficiency to do so. In principle, this should have little effect on the calculated N_μ since both N_μ^{obs} and ϵ_μ^{MC} should be reduced proportionally, but there is a higher risk of introducing data/Monte Carlo biases in the presence of tighter cuts. The tighter selections are as follows:

- fiducial volume of Sec. 3.3.1,
- exactly one negative phase II muon (cf. Sec. 3.3.3),
- no other phase II muons of either charge,
- no muon catastrophes (cf. Sec. 3.1.3.2),
- no other loose muons (cf. Sec. 3.3.3),
- event passes electron veto of Sec. 3.3.2.

Table 4.5 shows the number of events selected by each ν_μ CC definition, along with the calculated N_μ. These three values yield an average of $(1.62 \pm 0.05) \times 10^6$ events. This is higher than the value quoted in Ref. [99] because of the addition of the 1998 data and the use of a more inclusive[1] fiducial volume for the Monte Carlo sample in this analysis. The fiducial volume difference should have no effect on the

[1]Most other NOMAD analysis normalize their signal efficiencies and N_μ to a Monte Carlo sample with fiducial volume cuts of $|x|, |y| < 130$ cm. This analysis used $|x|, |y| < 140$ cm, so the efficiencies should be relatively lower and the N_μ correspondingly higher.

ν_μ CC Definition	N^{obs}_{data}	N^{obs}_{MC}	N_μ
Tighter Muon	733581	2287010	1.614×10^6
Fake NC DS Muon	1002656	3216394	1.569×10^6
Looser Muon	1163966	3492356	1.677×10^6

Table 4.5: Estimated number of data ν_μ CC events using three different definitions, as described in the text. The total Monte Carlo ν_μ CC sample size is 5032958 events.

Sample	N Monte Carlo / N Data (exp.)
ν_μ CC	3.11
$\overline{\nu}_\mu$ CC	14.5 ± 3.5
ν_e CC	91.8 ± 4.4
$\overline{\nu}_e$ CC	105 ± 13
NC	5.83 ± 0.07

Table 4.6: Factors by which the number of Monte Carlo simulated events outnumber the corresponding expected number of data events. The overall error due to the absolute (N_μ) normalization, which is about 3%, is not included here.

calculated oscillation probability, since it enters only as a normalization constant for both the signal efficiency (ϵ_{sig}) and the data (N_μ).

Given the size of the Monte Carlo samples from Tab. 2.5, the relative expected neutrino fluxes from the NUBEAM Monte Carlo (Tab. 2.3), and the normalization N_μ, one can calculate the factor by which each CC Monte Carlo sample outnumbers the corresponding expected data. The factor for the NC Monte Carlo is given by the expected number of CC events (of all varieties) multiplied by the NC to CC ratio [140] of 0.3117 ± 0.0027.

These factors have already been listed in Tab. 2.5, but are listed again here (Tab. 4.6) with their errors for clarity. Only the error due to the uncertainty in the relative fluxes is listed; the ($\sim 3\%$) error on N_μ is completely correlated among the samples.

4.2.3 Normalized ρ^+ analysis (Data/MC bias)

One can apply the same analysis and normalization to the Monte Carlo events selected by the ρ^+ analysis, as just outlined above for the ρ^- analysis. After normalizing the ρ^+

Sample	NC	ν_μ CC	$\overline{\nu}_\mu$ CC	ν_e CC	$\overline{\nu}_e$ CC
DST Events	3067890	5032958	588732	2157453	296974
$\tau \to \rho$ Candidates	136	35	0	190	23
$\ln \mathcal{L} \leq 0.0$	70	0	0	4	1
$\ln \mathcal{L} > 0.0$	66	35	0	186	22
$0.0 < \ln \mathcal{L} \leq 0.5$	14	6	0	9	1
$0.5 < \ln \mathcal{L} \leq 1.0$	12	4	0	13	1
$1.0 < \ln \mathcal{L} \leq 1.5$	9	7	0	25	1
$1.5 < \ln \mathcal{L} \leq 2.0$	14	5	0	29	4
$2.0 < \ln \mathcal{L} \leq 2.5$	9	5	0	32	6
$2.5 < \ln \mathcal{L} \leq 3.0$	5	6	0	41	6
$\ln \mathcal{L} > 3.0$	3	2	0	37	3

Table 4.7: Numbers of Monte Carlo events selected in the $\tau \to \rho^+$ analysis.

MC samples, any remaining differences between MC and ρ^+ data can be ascribed to some systematic data/MC bias. This bias can be measured using the ρ^+ data and then applied to the signal region of the ρ^- data later.

Table 4.7 lists the number of events selected by the ρ^+ analysis on each of the Monte Carlo background samples. The reconstructed leading lepton was not incorporated into the definition of the ρ^+ in any of the selected CC events, further supporting the hypothesis of Sec. 3.4.2. After normalizing each ρ^+ Monte Carlo sample to the expected size in the NOMAD data, the ratio of these gives the correction factor for the ρ^- background. Table 4.8 lists the expected number of ρ^+ events from all Monte Carlo samples, and the number actually observed in the data.

There are not enough events to derive independent and statistically significant data/Monte Carlo ratios from the information in each bin; therefore, the bins in the region of the signal box ($\ln \mathcal{L} > 0$) are combined in polynomial parameterizations of the data. Fitting the CC and NC Monte Carlo samples independently yields data/Monte Carlo ratios of $0.92^{+0.19}_{-0.13}$ and $0.75^{+0.15}_{-0.13}$, respectively, with a chi-square of 18.08 for 12 degrees of freedom. A better fit may be obtained by using a linear parameterization of the CC contribution. This yields a NC ratio of $0.69^{+0.16}_{-0.12}$ and a CC ratio of $(0.52^{+0.19}_{-0.15}) + (0.27 \pm 0.17)x$, with $\chi^2/\text{d.o.f.} = 12.6/11$. x is the value of the low edge of the $\mathcal{L}$ bin. (The $\mathcal{L} < 0$ bin is neglected in the fits.) Other polynomial fits to the NC and CC backgrounds yield lower chi-squared probabilities. The best-fit values from the CC linear, NC constant fit are thus used to model the ρ^+ backgrounds, and the errors from the fit are used as the basis for the systematic uncertainty.

Sample	Expected Background CC	NC	Observed Data
$\tau \to \rho$ Candidates	$13.6^{+1.9}_{-1.6}$	$23.3^{+2.0}_{-1.9}$	25
$\ln \mathcal{L} \leq 0.0$	< 0.4	$12.0^{+1.4}_{-1.3}$	10
$\ln \mathcal{L} > 0.0$	$13.6^{+1.9}_{-1.6}$	$11.3^{+1.4}_{-1.2}$	15
$0.0 < \ln \mathcal{L} \leq 0.5$	$2.0^{+0.8}_{-0.5}$	$2.4^{+0.6}_{-0.5}$	3
$0.5 < \ln \mathcal{L} \leq 1.0$	$1.4^{+0.6}_{-0.4}$	$2.1^{+0.6}_{-0.4}$	4
$1.0 < \ln \mathcal{L} \leq 1.5$	$2.5^{+0.8}_{-0.6}$	$1.5^{+0.5}_{-0.4}$	3
$1.5 < \ln \mathcal{L} \leq 2.0$	$2.0^{+0.7}_{-0.4}$	$2.4^{+0.6}_{-0.5}$	1
$2.0 < \ln \mathcal{L} \leq 2.5$	$2.0^{+0.7}_{-0.4}$	$1.5^{+0.5}_{-0.4}$	3
$2.5 < \ln \mathcal{L} \leq 3.0$	$2.4^{+0.8}_{-0.5}$	$0.9^{+0.4}_{-0.2}$	0
$\ln \mathcal{L} > 3.0$	$1.1^{+0.4}_{-0.2}$	$0.5^{+0.3}_{-0.2}$	1

Table 4.8: Numbers of expected ρ^+ events from the normalized Monte Carlo and number observed in the data.

4.2.4 Summary of ρ^- backgrounds

Normalizing the background events from Tab. 4.4 according to Tab. 4.6, and applying the data/MC corrections fitted above yields the number of background events of different types expected in the ρ^- data. This is presented in Tab. 4.9, where the errors are statistical and systematic due to the data/MC correction, respectively. The error listed in the bottom row is the systematic error due to the event normalization for each background type, and there is an additional unlisted 3% completely correlated systematic error in each bin due to the ν_μ CC normalization. The uncertainty in the data/MC fits presented in this section is by far the largest source of systematic error.

4.3 Oscillation Probability

This section presents the main results of this thesis: the oscillation allowed region and the sensitivity of the analysis.

After the signal efficiency and background rates have been calculated by the Monte Carlo and corrected by the data simulator, it is time to open the box and find out how many events are found in the signal region. This is briefly presented in Sec. 4.3.1.

Next, one must determine whether these data provide evidence for neutrino oscilla-

Likelihood Bin	NC	Data/MC	ν_μ CC	$\overline{\nu}_\mu$ CC	ν_e CC	$\overline{\nu}_e$ CC	Data/MC
$0.0 < \ln\mathcal{L} \leq 0.5$	$1.18^{+0.51}_{-0.37}$	$^{+23\%}_{-17\%}$	<0.40 @ 90% CL	<0.08	$0.02^{+0.02}_{-0.01}$	$0.010^{+0.013}_{-0.007}$	$^{+37\%}_{-28\%}$
$0.5 < \ln\mathcal{L} \leq 1.0$	$0.947^{+0.47}_{-0.33}$	$^{+23\%}_{-17\%}$	$0.86^{+0.68}_{-0.41}$	<0.11	$0.03^{+0.02}_{-0.01}$	$0.04^{+0.02}_{-0.02}$	$^{+30\%}_{-24\%}$
$1.0 < \ln\mathcal{L} \leq 1.5$	$0.83^{+0.447}_{-0.31}$	$^{+23\%}_{-17\%}$	$1.05^{+0.83}_{-0.50}$	<0.13	$0.05^{+0.03}_{-0.02}$	$0.08^{+0.03}_{-0.03}$	$^{+29\%}_{-24\%}$
$1.5 < \ln\mathcal{L} \leq 2.0$	$2.01^{+0.62}_{-0.48}$	$^{+23\%}_{-17\%}$	$0.93^{+0.90}_{-0.51}$	$0.27^{+0.22}_{-0.14}$	$0.03^{+0.03}_{-0.02}$	$0.10^{+0.04}_{-0.03}$	$^{+29\%}_{-25\%}$
$2.0 < \ln\mathcal{L} \leq 2.5$	$1.18^{+0.51}_{-0.37}$	$^{+23\%}_{-17\%}$	$1.07^{+1.04}_{-0.58}$	$0.08^{+0.18}_{-0.07}$	$0.06^{+0.04}_{-0.03}$	$0.12^{+0.049}_{-0.04}$	$^{+30\%}_{-26\%}$
$2.5 < \ln\mathcal{L} \leq 3.0$	$0.947^{+0.47}_{-0.33}$	$^{+23\%}_{-17\%}$	$1.21^{+1.18}_{-0.66}$	$0.17^{+0.23}_{-0.12}$	$0.26^{+0.08}_{-0.06}$	$0.07^{+0.04}_{-0.03}$	$^{+31\%}_{-27\%}$
$\ln\mathcal{L} > 3.0$	$0.59^{+0.40}_{-0.26}$	$^{+23\%}_{-17\%}$	$0.45^{+1.04}_{-0.37}$	<0.22	$0.20^{+0.07}_{-0.06}$	$0.147^{+0.06}_{-0.047}$	$^{+32\%}_{-29\%}$
Normalization Error	$\pm 1.1\%$		—	$\pm 2.3\%$	$\pm 4.8\%$	$\pm 12\%$	

Table 4.9: Normalized numbers of expected background events by source in the ρ^- channel, corrected for the data/MC bias. The errors quoted together with the background values are statistical only. The columns labelled "Data/MC" show the (correlated) systematic errors due to the correction for the Data/MC bias for NC and CC backgrounds separately. The bottom row shows the systematic error due to the event normalization relative to the ν_μ flux. These errors are correlated within each column. Finally, there is an overall 3% error in each bin (but totally correlated among all bins) due to the ν_μ flux uncertainty.

tions or not, and quote an appropriate limit in terms of oscillation probability. This is performed by a classical (non-Bayesian) statistical analysis, first proposed by Feldman and Cousins[141] of the NOMAD collaboration. The method is described in Sec. 4.3.2.

The Feldman–Cousins approach takes into account the statistical nature of a small signal above a purely Poisson distributed background, and in principle can be applied to a multibin analysis such as the one presented in this thesis. In actuality, though, the expected backgrounds to this analysis are not purely Poisson, and Sec. 4.3.3 outlines an approach to deal with that. With the backgrounds properly treated, the allowed oscillation probability interval is then calculated.

One measure of an experiment's power to resolve a small signal, which is similar to the oscillation limit but largely independent of the data, is the sensitivity. This is defined and calculated in Sec. 4.3.4.

Finally, the oscillation probability intervals (limits) are transformed to allowed (excluded) regions on the traditional phase space plot in Sec. 4.3.5.

4.3.1 ρ^- data (Opening the box)

The expected number of ρ^- background events is given by the numbers counted in the various Monte Carlo samples (from Tab. 4.4) normalized to the data size (cf. Tab. 4.6) and multiplied by the respective data/Monte Carlo correction factors derived from the ρ^+ data. Table 4.10 shows the number of expected background events inside the ρ^- signal box ($\ln \mathcal{L} > 0$), and the number of events observed in the data. The 16 events selected by this analysis are listed by run and event number in Tab. 4.11.

In order to convert this into an oscillation probability, a binned likelihood analysis is performed over the seven bins of Tab. 4.10.

4.3.2 Feldman–Cousins method

The ρ^- results are analyzed using classical (non-Bayesian) statistics to derive an oscillation probability, and confidence intervals are generated via the Feldman–Cousins [141] prescription.

Classical confidence intervals are described in Ref. [141], Sec. IIB. Using classical intervals avoids the use of subjective prior probability density functions for the parameter being measured. The condition which must be satisfied for any confidence interval of probability α is that the true (unknown) value lies inside the interval in a fraction α of experiments. An interval satisfying this requirement is said to provide proper coverage of the measured parameter. For any value α, however, there is an infinite set of confidence regions which satisfy this requirement; upper limits, central intervals, and lower limits are only the three most common choices.

The Feldman–Cousins method specifies a mechanism for choosing particular confidence belts that provides proper coverage while retaining the power to eliminate un-

Sample	Expected Background	Observed Data
$0.0 < \ln\mathcal{L} \leq 0.5$	$1.2^{+0.5+0.3}_{-0.4-0.2}$	0
$0.5 < \ln\mathcal{L} \leq 1.0$	$1.9^{+0.8+0.4}_{-0.5-0.3}$	2
$1.0 < \ln\mathcal{L} \leq 1.5$	$2.0^{+0.9+0.4}_{-0.6-0.4}$	1
$1.5 < \ln\mathcal{L} \leq 2.0$	$3.3^{+1.1+0.6}_{-0.7-0.7}$	4
$2.0 < \ln\mathcal{L} \leq 2.5$	$2.5^{+1.2+0.5}_{-0.7-0.5}$	3
$2.5 < \ln\mathcal{L} \leq 3.0$	$2.7^{+1.3+0.6}_{-0.7-0.6}$	3
$\ln\mathcal{L} > 3.0$	$1.4^{+1.1+0.3}_{-0.5-0.4}$	3
Total	$15.0^{+2.7+2.9}_{-1.6-2.8}$	16

Table 4.10: Numbers of expected ρ^- events from the normalized Monte Carlo, and numbers in the data. The errors are statistical and systematic, respectively, and the systematic uncertainties are correlated.

likely values. By doing so, it also separates the choice of confidence belts (upper limit vs. central interval, e.g.) from the data themselves. The prescription assumes the ability to simulate a hypothetical measurement x which depends on a variable μ with unknown true value μ_t (via a Monte Carlo, for example). Thus, for each possible (physically allowed) value of μ, the probability of obtaining any hypothetical measurement x can be calculated through simulation. This is written $P(x|\mu)$. Conversely, for a given measurement x, there is a physically allowed value of μ which maximizes $P(x|\mu)$. This particular value of μ is denoted by $\hat{\mu}$. The Feldman–Cousins ordering principle uses the ratio of these probabilities. For a given value μ, each possible measurement x is assigned a rank given by

$$R = \frac{P(x|\mu)}{P(x|\hat{\mu})}. \tag{4.6}$$

Arranging all possible measurements for a given μ in decreasing rank, the acceptance region is the smallest[2] set $\{x_1 \ldots x_n\}$ such that $\sum_1^n P(x|\mu) \geq \alpha$. Finally, once an actual measurement x_0 has been made by an experiment, the confidence region for the true

[2]If there is no value of n such that $\sum_1^n P(x|\mu) = \alpha$, which may happen with Poisson statistics where the values of x are discrete, then one must choose an acceptance region which overcovers μ. In this case it is desirable to choose the region which overcovers the least, so the *smallest* region with $\sum_1^n P(x|\mu) > \alpha$ is chosen.

Run	Event	Likelihood $\mathcal{L}$
9146	25795	0.68
13641	8987	0.77
7985	25239	1.25
14162	25050	1.62
14150	5715	1.75
15162	1182	1.85
20622	21389	2.00
20012	16748	2.26
21561	4752	2.38
13414	38325	2.45
14133	4205	2.60
8233	27254	2.76
12454	7214	2.79
17261	28133	3.56
12519	50137	3.69
17120	20937	3.89

Table 4.11: Individual events in the data selected by the ρ^- analysis, listed in order of increasing likelihood.

value μ_t is the union of all μ whose acceptance regions include the value x_0. This method is also known as the frequentist approach.

Feldman and Geiser applied [142] this approach to the analysis of neutrino oscillation data in several bins with expected backgrounds and errors. For N independent measurements of μ_t (for instance, N energy bins, N likelihood bins as in this analysis, N decay channels, or N different experiments), the rank for each μ is just the difference in χ^2 between the μ and $\hat{\mu}$ likelihoods, which for Poisson statistics is [142]:

$$R = 2\sum_{i=1}^{N}\left[(\mu_i - \hat{\mu}_i) + x_i \ln\left(\frac{\hat{\mu}_i}{\mu_i}\right)\right]. \tag{4.7}$$

If μ is the number of oscillation signal events one expects in NOMAD, b is the expected background, and n is the number actually observed, then the rank becomes

$$R = 2\sum_{i=1}^{N}\left[(\mu_i - \hat{\mu}_i) + n_i \ln\left(\frac{\hat{\mu}_i + b_i}{\mu_i + b_i}\right)\right]. \tag{4.8}$$

The error on the background estimation can be included in an approximate way by treating it as a Poisson fluctuation. If the error were truly Poisson, the expression for the rank (Eq. 4.6) would become [142]:

$$R = \frac{P(x|\mu + \hat{\hat{\beta}})P(b|\hat{\hat{\beta}})}{P(x|\hat{\mu} + \hat{\beta})P(b|\hat{\beta})}, \tag{4.9}$$

where $\hat{\hat{\beta}}$ is chosen to maximize the numerator, and $\hat{\mu}$ and $\hat{\beta}$ maximize the denominator.

A Monte Carlo program [143], is used to implement this procedure for the data in the seven likelihood bins of Tab. 4.10. The Feldman–Cousins method calculates a confidence interval on the number (N_{osc}) of ν_τ CC events seen at a specified level α for each likelihood bin, which is either an upper limit or a two-sided limit as the method decides. Given the maximum number (N_τ) of ν_τ CC events possible in each bin, an oscillation probability ($P_{osc} = N_{osc}/N_\tau$) interval is defined for each bin, and the intervals from all bins are combined using Eq. 4.7.

The maximum number of ν_τ CC events in each likelihood bin (i.e. the number of ν_τ CC interactions expected for full $\nu_\mu \rightarrow \nu_\tau$ oscillation) is defined [99] by:

$$N_\tau = N_\mu \times (\sigma_\tau/\sigma_\mu) \times (\epsilon_\tau \times Br), \tag{4.10}$$

where N_μ is the ν_μ CC normalization from Sec. 4.2.2, $\epsilon_\tau \times Br$ was encountered in Sec. 4.1, and the ratio of cross sections expresses the ν_τ CC suppression due to the mass difference between the τ and μ. This last factor has been calculated [99] to be 0.48 in the energy regime relevant to NOMAD analyses. Table 4.12 lists N_τ for the

Sample	N_τ
$0.0 < \ln\mathcal{L} \leq 0.5$	$61 \pm 3 \pm 4$
$0.5 < \ln\mathcal{L} \leq 1.0$	$126 \pm 5 \pm 8$
$1.0 < \ln\mathcal{L} \leq 1.5$	$198 \pm 7 \pm 12$
$1.5 < \ln\mathcal{L} \leq 2.0$	$265 \pm 7 \pm 17$
$2.0 < \ln\mathcal{L} \leq 2.5$	$328 \pm 9 \pm 21$
$2.5 < \ln\mathcal{L} \leq 3.0$	$415 \pm 11 \pm 27$
$\ln\mathcal{L} > 3.0$	$491 \pm 11 \pm 31$

Table 4.12: Number of ν_τ CC events expected in each likelihood bin of this analysis if the oscillation probability were unity. The errors are statistical and systematic, respectively.

seven likelihood bins of this analysis. The systematic error is dominated by the 5% uncertainty in the cross section ratios σ_τ/σ_μ. Also included in the systematic uncertainty is the 3% uncertainty in the absolute ν_μ CC rate, the uncertainty in the τ branching fractions, and the error introduced by the signal data/MC correction.

4.3.3 Background simplifications and the oscillation limit

In the background analysis of this thesis, there are two complicating factors. The first is that the errors are not entirely due to Poisson statistics. Both the background central values and their Poisson errors are reweighted due to the data/Monte Carlo systematic differences; in addition, the relative normalization of the different neutrino species contributes to the background errors. These can still be handled in a consistent way for each likelihood bin by calculating an *effective* integer-valued background, such that the relative Poisson error of this effective error is equivalent to the actual calculated background error. For instance, if the background in some bin is estimated to be 2.5 ± 0.6 (24% error), a Poisson variable with a mean of 16 could be used as an effective error in place of 2.5. Equation 4.9 can then be used to give weights to all possible experimental outcomes, after which the backgrounds are rescaled back to their nominative values. In the example above, the background of 16 would be rescaled by a factor of 0.156 after calculating the rank.

The other complicating factor is that the background errors are partially correlated[3] among the seven likelihood bins, while the procedure described in Ref. [142] assumes

[3]The correlations derive mainly from the data/Monte Carlo correction factors, which come from the fit to the ρ^+ data. These errors are of approximately the same magnitude as the background Poisson errors.

Sample	B_-	B_0	B_+	Data
$0.0 < \ln\mathcal{L} \leq 0.5$	$1.0^{+0.5}_{-0.3}$	$1.2^{+0.5}_{-0.4}$	$1.5^{+0.7}_{-0.5}$	0
$0.5 < \ln\mathcal{L} \leq 1.0$	$1.6^{+0.7}_{-0.4}$	$1.9^{+0.8}_{-0.5}$	$2.2^{+1.0}_{-0.6}$	2
$1.0 < \ln\mathcal{L} \leq 1.5$	$1.7^{+0.8}_{-0.5}$	$2.0^{+0.9}_{-0.6}$	$2.4^{+1.1}_{-0.7}$	1
$1.5 < \ln\mathcal{L} \leq 2.0$	$2.9^{+1.0}_{-0.6}$	$3.3^{+1.1}_{-0.7}$	$4.0^{+1.3}_{-0.8}$	4
$2.0 < \ln\mathcal{L} \leq 2.5$	$2.1^{+1.0}_{-0.6}$	$2.5^{+1.2}_{-0.7}$	$3.0^{+1.4}_{-0.8}$	3
$2.5 < \ln\mathcal{L} \leq 3.0$	$2.2^{+1.0}_{-0.6}$	$2.7^{+1.3}_{-0.7}$	$3.2^{+1.6}_{-0.9}$	3
$\ln\mathcal{L} > 3.0$	$1.1^{+0.9}_{-0.4}$	$1.4^{+1.1}_{-0.5}$	$1.7^{+1.4}_{-0.6}$	3
Total	$12.7^{+2.3}_{-1.3}$	$15.0^{+2.7}_{-1.6}$	$17.9^{+3.2}_{-1.9}$	16

Table 4.13: Numbers of expected background events in the absence of correlated systematic errors (B_0), and shifted up (B_+) and down (B_-) by 1σ of the correlated errors. The quoted errors are the statistical errors only. The number of events seen in the ρ^- data is also shown for reference.

independent bins. To reconcile this, first the correlated errors are separated and removed from the background estimation. The oscillation probability may then be calculated using only the uncorrelated errors in each bin (B_0). The effect of the correlated errors is then estimated by shifting the expected backgrounds first up (B_+) and then down (B_-) according to the sizes of the correlated errors, all the while leaving the uncorrelated errors unchanged. These three sets of backgrounds are listed in Tab. 4.13, and comparing them shows the effect of the systematic errors on the expected backgrounds.

Choosing each set of backgrounds in turn, one may calculate allowed oscillation probability regions using the frequentist approach at arbitrary confidence levels (CL). Table 4.14 lists the oscillation limits that can be set from these data at the 90%, 95%, and 99% CL and shows the effect of the correlated systematic errors on those limits. All confidence regions were determined by the data to be one sided upper limits.

4.3.4 Sensitivity

Reference [141] defines the sensitivity of an experiment (S_{osc}) as "the average upper limit that would be set by an ensemble of experiments with the same expected background in the absence of signal." The sensitivity of an experiment may be different from the limit set by that experiment if the number of observed events differs markedly from the expected background (due to statistical fluctuations, for instance). In order to calculate the sensitivity rigorously, one should sum the limits obtained by all possible

Sample	B_-	B_0	B_+
P_{osc} 90% CL ($\times 10^{-3}$)	6.50	5.52	4.40
P_{osc} 95% CL ($\times 10^{-3}$)	7.41	6.43	5.32
P_{osc} 99% CL ($\times 10^{-3}$)	9.26	8.30	7.23

Table 4.14: Upper limits on the neutrino oscillation probability obtained in the presence of no systematic errors (B_0), and after shifting the expected background levels up (B_+) and down (B_-) by 1σ of the systematic errors.

Sample	B_-	B_0	B_+
P_{osc} 90% CL ($\times 10^{-3}$)	2.11	2.58	3.12
P_{osc} 95% CL ($\times 10^{-3}$)	2.52	3.09	3.73
P_{osc} 99% CL ($\times 10^{-3}$)	3.35	4.08	4.94

Table 4.15: Neutrino oscillation probability sensitivities obtained in the presence of no systematic errors (B_0), and after shifting the expected background levels up (B_+) and down (B_-) by 1σ of the systematic errors.

experimental outcomes weighted by the probability of the outcome. An approximation of this rigorous method would be to randomly sample a large number of outcomes. A less rigorous but still good approximation [142] is to calculate the limit obtained by an experiment which sees the same number of data as its expected background. This last method is by far the simplest to implement, and using it yields the sensitivities listed in Table 4.15.

In order to account for the uncertainty represented by the systematic error, one must choose the sample (B_-,B_0,or B_+) which produces the most conservative result. Comparing Tabs. 4.14 and 4.15, though, one can see that the oscillation limit and the sensitivity anticorrelate among the three background sets. However, since the sensitivity is independent of the data, the set with the most conservative sensitivity (B_+) is chosen as the result of this analysis:

$P_{osc} < 4.40 \times 10^{-3}$, $S_{osc} < 3.12 \times 10^{-3}$ 90% CL,
$P_{osc} < 5.32 \times 10^{-3}$, $S_{osc} < 3.73 \times 10^{-3}$ 95% CL, and
$P_{osc} < 7.23 \times 10^{-3}$, $S_{osc} < 4.94 \times 10^{-3}$ 99% CL.

In the B_+ background sample, there are a total of 17.9 events, and only 16 events were found in the data. If the sensitivity is calculated by computing the limit one would

expect from an experiment that sees exactly the same as expected, one might expect that the limit obtained in the case of *fewer* signal events would be more stringent. In fact, in this case the opposite is true. The explanation can be found in a careful examination of Table 4.13. While the total number of expected background events is larger for the B_+ sample than was seen in the data, the *distribution* of those data events over the seven likelihood bins was different from expected. This difference leads to the higher oscillation limit than sensitivity not only for the B_+ sample, but for all three background sets.

4.3.5 Phase space plots

Given an upper limit on the oscillation probability, one can use Eq. 1.18 to convert this into an excluded region in $\sin^2 2\theta$ for each value of Δm^2 of interest in a phase space plot. For a point neutrino source and a monochromatic beam, this is simply an algebraic exercise. For the NOMAD beam, however, $\sin^2 2\theta$ exclusion regions are defined for each given Δm^2 by:

$$\sin^2 2\theta \left\langle \sin^2 \left(\frac{1.27 \Delta m^2_{jk} (eV^2/c^4) L(m)}{P(MeV/c)} \right) \right\rangle < P_{osc}, \tag{4.11}$$

where $\langle x \rangle$ denotes the expected value of x.

A Monte Carlo program was used to construct the expected value of the second $\sin^2$ term. Given the distribution of neutrino energies for Monte Carlo $\tau \rightarrow \rho$ events which are selected by this analysis (see Fig. 4.1), oscillation lengths were chosen uniformly in the range [421.5,835.6] meters and the resulting $\sin^2$ terms were averaged. According to the NUBEAM beamline Monte Carlo, the distribution of neutrino flight path lengths is approximately uniform on this interval for neutrino energies greater than 25 GeV (see Fig. 4.2).

Using this procedure, upper bounds on $\sin^2 2\theta$ were derived for 1000 values of Δm^2 in the range $1 < \Delta m^2 < 10^5 eV^2/c^4$. These points are plotted and connected by a line in Fig. 4.3 for the 90% confidence exclusion region. Likewise, Fig. 4.4 shows the 90% CL sensitivity region. From these plots one can learn that $\nu_\mu \rightarrow \nu_\tau$ oscillations are excluded by this analysis for $\sin^2 2\theta$ values greater than 8.79×10^{-3} at large Δm^2, and Δm^2 is required to be less than 3.75 $eV^2/c^4$for full two-family neutrino mixing.

4.4 Other NOMAD Results

The official $\nu_\mu \rightarrow \nu_\tau$ oscillation limit from NOMAD is based on the combination of several independent analyses of different τ^- decay modes. For each mode several independent analyses are performed, and only the one with the lowest sensitivity is

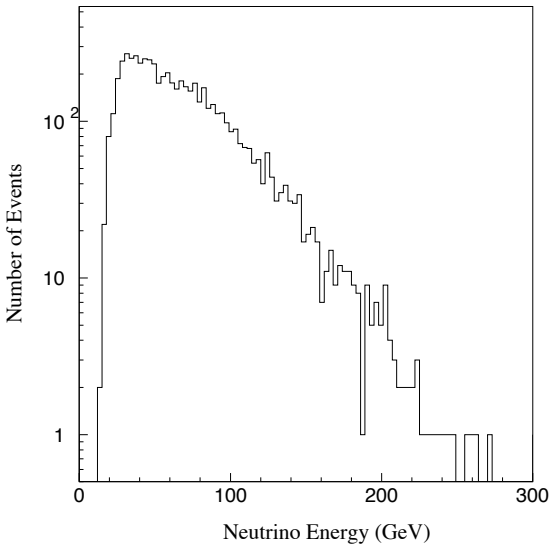

Figure 4.1: Neutrino energy distribution of Monte Carlo $\tau \rightarrow \rho$ events selected by this analysis. The average energy is 68 GeV.

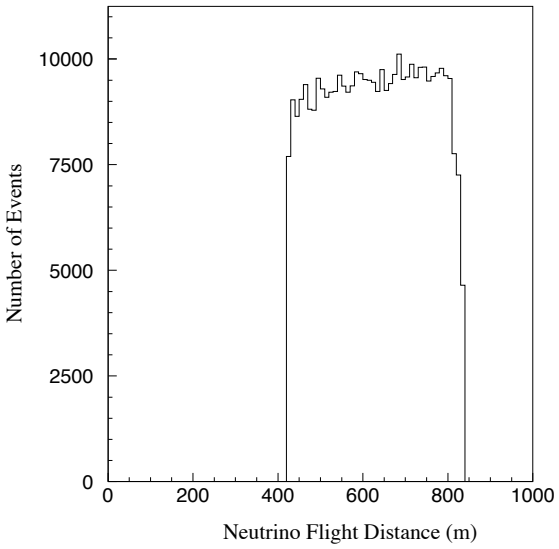

Figure 4.2: Monte Carlo neutrino flight path lengths for neutrinos with energies greater than 25 GeV.

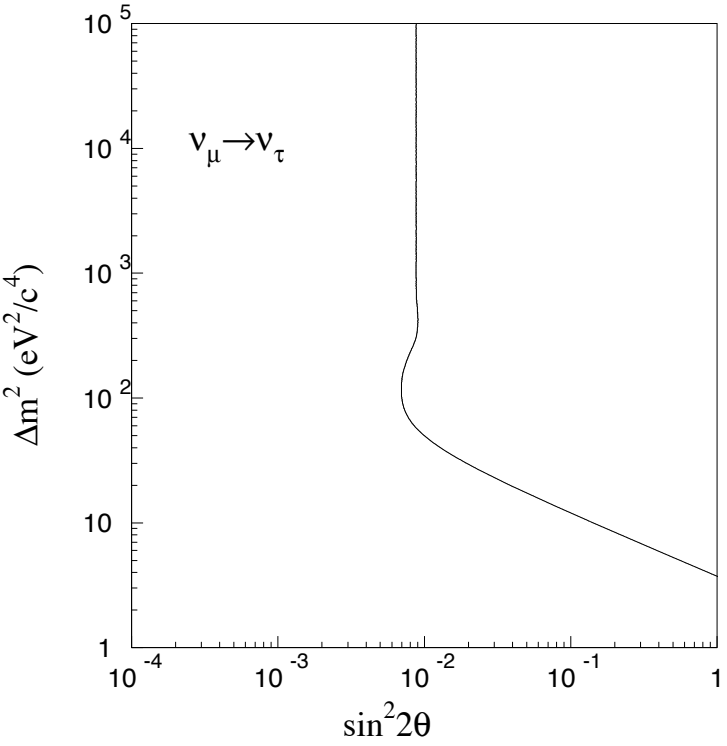

Figure 4.3: Phase space exclusion plot for this analysis. The 90% confidence excluded region lies to the right of the curve.

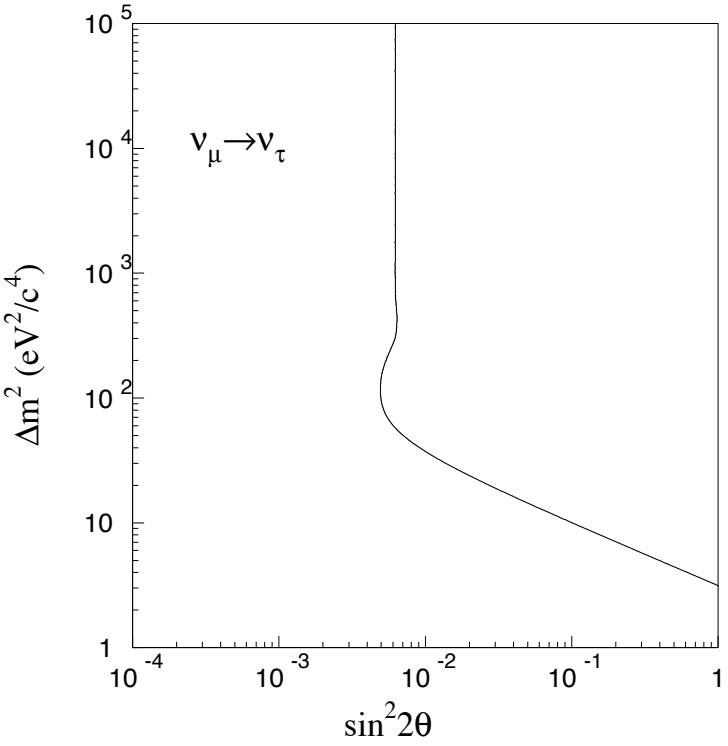

Figure 4.4: Phase space sensitivity plot for this analysis. The 90% confidence excluded region lies to the right of the curve.

published. The modes are combined as independent bins using the Feldman–Cousins approach, just as the likelihood bins of this analysis were combined in Sec. 4.3.2.

Since the *sensitivity* (not the oscillation limit) of an analysis with no expected signal is dependent only on the expected background, choosing the analysis with the smallest sensitivity is almost data-independent. The fluctuation of a few events in the signal box region does not affect the sensitivity of an analysis at all.

The analysis presented in this thesis is not the official published one for the $\tau \rightarrow \rho$ decay channel because one other analysis had a slightly lower sensitivity. In the next section I compare and contrast these two analyses. Following that, I present the data and limits from all τ decay modes in NOMAD.

4.4.1 Comparison with the official $\tau \rightarrow \rho$ analysis

The official NOMAD result for the $\nu_\mu \rightarrow \nu_\tau$ oscillation in the $\tau \rightarrow \rho$ channel is based on an analysis that is similar to the one presented in this thesis. The basic approaches of the two analyses are identical. Both make a set of event quality and CC veto cuts, both identify rho candidates and use kinematics to separate $\tau \rightarrow \rho$ events from CC and NC backgrounds. Both analyses use multidimensional likelihood functions, and they both use a data simulator to reduce systematic effects.

The substantive differences between the analyses are summarized below:

1. The official analysis uses separate likelihood functions for the CC and NC backgrounds, rather than the total background function of Sec. 3.2.3.

2. The likelihood functions used by the official analysis to separate $\tau \rightarrow \rho$ events from the CC and NC backgrounds are convolutions of a two-dimensional and two three-dimensional likelihood functions:

$$\mathcal{L} = \mathcal{L}_3 \left(\mathcal{L}_2 \left(\mathcal{L}_1 \left(\theta_{\nu T}, \theta_{\nu h} \right), \theta_{\ell h}, Q_\perp \right), \phi_{\ell h}, \not{P}_\perp \| \right)$$

   where $\theta_{\nu T}$ and $\theta_{\nu h}$ are the angles between the neutrino beam direction and the total energy vector and the hadron jet vector, respectively, $\phi_{\ell h}$has been encountered in Sec. 3.2.2 and $Q_\perp$ was defined in Sec. 3.2.3.3, $\theta_{\ell h}$ is the 3-space equivalent of the transverse plane angle $\phi_{\ell h}$, and $\not{P}_\perp \|$ is the component of the missing transverse momentum that lies parallel to the τ transverse momentum. Because each likelihood function ($\mathcal{L}_1$, $\mathcal{L}_2$, $\mathcal{L}_3$) is only a function of 2 or three variables, the smoothing of Sec. 3.2.3.2 is unnecessary.

3. In the official analysis, π^0's composed of one PO are treated independently from two-PO π^0's.

4. The official analysis uses another likelihood analysis to identify ρ's in an event. For one-PO π^0's the function uses the angle in 3-space between the τ (ρ) and

Bin	Background	Data	N_τ
I. 1-PO π^0	6.10 ± 1.93	5	883
II. 1-PO π^0	$0.33^{+0.74}_{-0.10}$	0	1736
III. 2-PO π^0	3.00 ± 1.40	2	466
IV. 2-PO π^0	$0.06^{+0.88}_{-0.04}$	0	222

Table 4.16: Results of the official NOMAD $\tau \rightarrow \rho$ analysis. For the four bins of that analysis, the estimated backgrounds, observed data events, and estimated number of events for full oscillation are listed. Data obtained from Ref. [144].

the hadron jet and also the ratio of the τ energy to the total visible energy in the event:

$$\mathcal{L}_{1PO}\left(\theta_{\tau h}, E_\tau / E_{vis}\right)$$

For the two-PO π^0's, the likelihood contains the ratios of the π^0 and the π^+ energies to the total visible energy:

$$\mathcal{L}_{2PO}\left(\mathcal{L}'_{2PO}\left(E_{\pi^0}/E_{vis}, E_{\pi^+}/E_{vis}\right), \theta_{\tau h}\right)$$

5. The data simulator was sufficient for calculating the data/MC correction in both the signal and background regions, so the official analysis did not need to rely on the ρ^+ data for this.

6. Two likelihood bins were constructed in the signal regions in both the one-PO and two-PO data, for a total of four independent bins.

These four signal bins are listed in Tab. 4.16, with their respective numbers of background, events seen in the data, and effective N_τ.

Using the data from these bins to set an oscillation limit yields:

- $P_{osc} < 0.52 \times 10^{-3}$ at 90% CL,
- $P_{osc} < 0.79 \times 10^{-3}$ at 95% CL, and
- $P_{osc} < 1.44 \times 10^{-3}$ at 99% CL.

The sensitivity is estimated to be:

- $S_{osc} < 0.85 \times 10^{-3}$ at 90% CL,

- $S_{osc} < 1.14 \times 10^{-3}$ at 95% CL, and
- $S_{osc} < 1.82 \times 10^{-3}$ at 99% CL.

The limits and sensitivities from the official analysis are significantly better than the ones derived from the analysis of this thesis, but the results are not inconsistent with each other. The fact that neither analysis sees any sign of neutrino oscillation is a good mutual confirmation.

The analysis of this thesis used a more conservative approach in estimating the background systematics and used only one grand likelihood function. The data simulator approach used for the backgrounds in this analysis (Sec. 4.2.3) contributes a large part of the systematic error; without that, the sensitivity might be 20% lower. The bulk of the difference, however, comes from the separating power of the likelihood arrays. With more events to populate the arrays, or with smaller arrays, the likelihood functions become more smooth. The fact that the likelihood/smoothing approach taken in this thesis was successful at all is remarkable given the sparseness of especially the background likelihood arrays (around 1 event per 1000 bins).

4.4.2 The NOMAD oscillation results

Other analyses in NOMAD probed the τ hadron 1-prong and 3-prong decay channels as well as the electron leptonic decay channel to include 83% of the total τ branching fraction. The muonic decay channel was not used as the background due to ν_μ CC events was overwhelming. The greatest sensitivity search in each channel was then used to define a global confidence interval for the NOMAD experiment.

The searches with the highest sensitivities all used some form of a kinematic likelihood function to discriminate CC signal from NC backgrounds, and some of them even used likelihood functions to help select their τ candidates. The largest systematic errors came from the data/MC correction (data simulator), at 20%.

In addition to the high multiplicity DIS searches, like the one in this thesis, additional searches were performed with the low multiplicity (LM) event topologies. A single τ with little or no accompanying hadronic shower may be found in a ν_τ CC event when the ν_τ–nucleon interaction is either quasi-elastic or at a nuclear resonance. While the kinematic properties of LM events are not as clear as DIS ones, the τ reconstruction is made considerably easier. In addition, the cross section ratio σ_τ/σ_μ is significantly higher for LM events as compared with DIS (0.60–0.82 vs. 0.48). The LM analyses required the hadronic energy to be less than 1.5 GeV in an event, whereas the DIS searches required it to be greater than the same amount, so these were really independent searches.

Table 4.17 shows the backgrounds and efficiencies for the analyses used to define the NOMAD confidence interval. These data suggest an upper limit on $\nu_\mu \rightarrow \nu_\tau$

Decay Channel		Bin	Est. Bkgrnd	Obs.	N_τ
$\tau \to e^- \overline{\nu}_e \nu_\tau$	DIS	I	$1.15^{+0.26}_{-0.17}$	2	178
		II	$0.53^{+0.23}_{-0.12}$	1	208
		III	$0.28^{+0.31}_{-0.09}$	0	903
		IV	2.13 ± 0.23	2	654
		V	0.98 ± 0.16	0	473
		VI	0.25 ± 0.09	0	1694
	LM	I	3.09 ± 0.67	3	282
		II	1.50 ± 0.41	2	285
		III	0.82 ± 0.41	1	292
$\tau \to \rho^- \nu_\tau$	DIS	I	6.10 ± 1.93	5	883
		II	$0.33^{+0.74}_{-0.10}$	0	1736
		III	3.00 ± 1.40	2	466
		IV	$0.06^{+0.88}_{-0.04}$	0	222
	LM	I	5.2 ± 1.8	7	458
$\tau \to h^- / \rho^- \nu_\tau$	DIS		$0.0^{+0.74}_{-0.0}$	1	210
$\tau \to h^- \nu_\tau$	DIS	I	4.4 ± 1.9	3	817
		II	2.4 ± 0.8	2	1205
	LM		6.7 ± 2.3	5	357
$\tau \to h^- h^+ h^- \nu_\tau$	DIS		9.6 ± 2.4	9	1820
	LM		$0.4 \pm 0.60.4$	0	108

Table 4.17: $\nu_\mu \to \nu_\tau$ oscillation search results from all official NOMAD $\tau \to \rho$ analyses. Data obtained from Ref. [144].

oscillation probability of

$$P_{osc}(\nu_\mu \to \nu_\tau) < 2.1 \times 10^{-4} \tag{4.12}$$

at 90% CL. The sensitivity of the experiment, also at 90% CL, is

$$P_{osc}(\nu_\mu \to \nu_\tau) = 4.2 \times 10^{-4}. \tag{4.13}$$

4.5 Conclusion

Using the full (1995–1998) NOMAD data sample, and selecting the $\tau \to \rho$ decay channel, a limit on the $\nu_\mu \to \nu_\tau$ oscillation probability is made at the 90% confidence level of $P_{osc} < 4.40 \times 10^{-3}$. The sensitivity of this analysis is $S_{osc} < 3.12 \times 10^{-3}$

at 90% confidence. The oscillation limit excludes $\sin^2 2\theta$ at values greater than 8.79×10^{-3} at large Δm^2, and restricts Δm^2 to values of less than 3.75 eV^2/c^4 for full mixing.

The published [144] NOMAD analysis on 1995–1998 data makes a better limit, but that includes all analyzed τ^- decay channels. The official $\tau \rightarrow \rho$ analysis achieves a better sensitivity, and is able to place a more stringent limit on oscillations.

The event selection method based on a kinematical likelihood has been shown to be effective. Even with very loose requirements on the ρ^-, this analysis has been able to make an oscillation limit consistent with other NOMAD analyses.

The main limitation to this analysis was in understanding the differences between data and Monte Carlo backgrounds. Because of a lack of Monte Carlo statistics the data simulator method was not viable. The precision of the data/Monte Carlo correction factor was thus dependent on the number of ρ^+ events in both data and Monte Carlo.

Appendix A

Charge Bias in the Data Simulator

In Sec. 3.4.1 the NC data simulator is used to derive an estimate of the ratio of background efficiencies in the data and the MC:

$$f_{bak}^{DS} \equiv \left(\frac{\epsilon_{DS}^{data}}{\epsilon_{DS}^{MC}}\right)_{bak} \approx f_{bak} \equiv \left(\frac{\epsilon^{data}}{\epsilon^{MC}}\right)_{bak}, \tag{A.1}$$

where ϵ_{DS}^{data} and ϵ_{DS}^{MC} are the measured analysis efficiencies on the background (fake NC) data simulator, and ϵ^{data} and ϵ^{MC} represent the true, unmeasurable efficiencies on data and Monte Carlo, respectively.

The ratio of efficiencies for the CC backgrounds (f_{bak}^{CC}) and for the NC background (f_{bak}^{NC}) is assumed to be the same. This is not unreasonable, since the ρ^- in non-ν_τ CC and in NC events both come from the hadron jet, and the kinematics should be similar.

One might think that the numbers of selected events (N_{sel}^{data} in Eq. 3.16 and N_{sel}^{MC} in Eq. 3.17) would just be the number of events in which a ρ^- is found by this analysis. In fact the *sum* of the ρ^- events and ρ^+ events found in the background data simulator was used in the efficiency ratio calculation. The rest of this appendix serves as a justification for this procedure, which was originally proposed in Ref. [145].

Figure A.1 shows the ρ production mechanisms for NC and ν_μ CC events. Restricting ourselves to first generation quarks, the NC interaction takes a u (d) quark to a u (d) quark. The probability of finding a ρ^+/ρ^- in the hadron jet initiated by a u quark is $P(u \to \rho^+)/P(u \to \rho^-)$. Since the leading u can form a ρ^+ directly with a $\bar{d}$ from the sea (see Fig. A.1a), the probability $P(u \to \rho^+)$ is much larger than $P(u \to \rho^-)$. The d quark has the corresponding probabilities $P(d \to \rho^+)$ and $P(d \to \rho^-)$ of forming a ρ^+ and ρ^-, respectively. The cross sections for producing ρ^+ and ρ^- in NC events are thus:

$$\sigma_{NC}^{+} = \sigma_{\nu u \to \nu u} \times P(u \to \rho^+) + \sigma_{\nu d \to \nu d} \times P(d \to \rho^+) \tag{A.2}$$

$$\sigma_{NC}^{-} = \sigma_{\nu u \to \nu u} \times P(u \to \rho^-) + \sigma_{\nu d \to \nu d} \times P(d \to \rho^-). \tag{A.3}$$

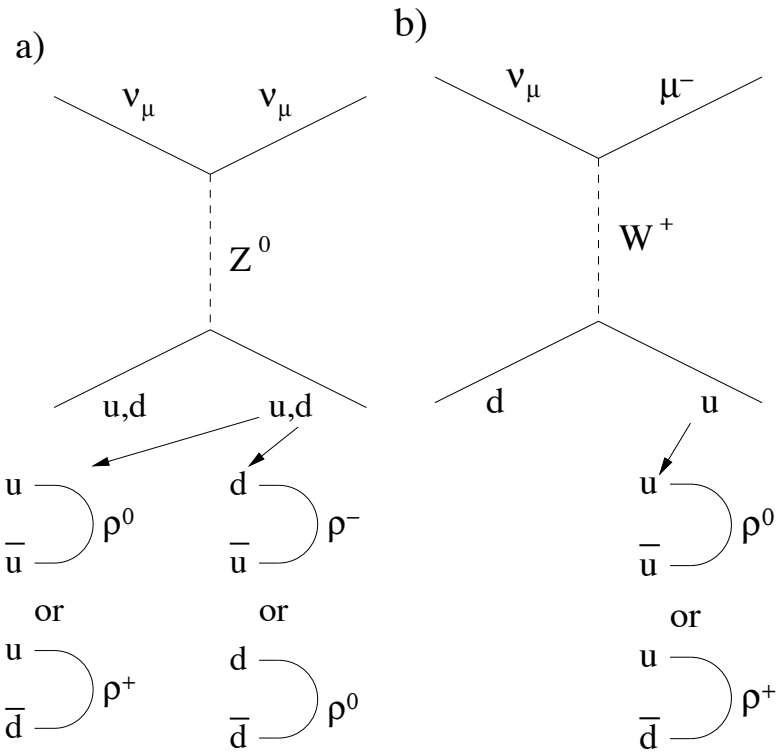

Figure A.1: Production mechanisms for ρ mesons in a) NC and b) ν_μ CC events.

In a CC event (Fig. A.1b), the W^+ takes a d quark to a u, so the cross sections for producing ρ^+ and ρ^- in CC events are:

$$\sigma^+_{CC} = \sigma_{\nu d\to\mu^- u} \times P(u \to \rho^+) \tag{A.4}$$
$$\sigma^-_{CC} = \sigma_{\nu d\to\mu^- u} \times P(u \to \rho^-). \tag{A.5}$$

By strong isospin symmetry, the fragmentation probabilities should be equivalent:

$$P(u \to \rho^+) = P(d \to \rho^-) \tag{A.6}$$
$$P(u \to \rho^-) = P(d \to \rho^+). \tag{A.7}$$

Writing the NC cross sections in terms of the CC cross sections, we get:

$$\sigma^+_{NC} = \frac{\sigma_{\nu u\to\nu u}}{\sigma_{\nu d\to\mu^- u}} \times \sigma^+_{CC} + \frac{\sigma_{\nu d\to\nu d}}{\sigma_{\nu d\to\mu^- u}} \times \sigma^-_{CC} \tag{A.8}$$
$$\sigma^-_{NC} = \frac{\sigma_{\nu u\to\nu u}}{\sigma_{\nu d\to\mu^- u}} \times \sigma^-_{CC} + \frac{\sigma_{\nu d\to\nu d}}{\sigma_{\nu d\to\mu^- u}} \times \sigma^+_{CC}. \tag{A.9}$$

From the difference in Z–quark couplings we find that $\sigma_{\nu u\to\nu u} \approx 0.8\sigma_{\nu d\to\nu d}$. Since the NOMAD target is approximately isoscalar, we also have $\sigma_{NC}/\sigma_{CC} \approx 1/3$. Putting these together we have

$$\begin{aligned}
\sigma_{NC} &= \underbrace{\sigma_{\nu u\to\nu u}}_{0.8\sigma_{\nu d\to\nu d}} + \sigma_{\nu d\to\nu d} \\
&\approx \frac{1}{3}\sigma_{CC} \\
&= \frac{1}{3}\sigma_{\nu d\to\mu^- u} \\
&\Longrightarrow \\
\frac{9}{5}\sigma_{\nu d\to\nu d} &\approx \frac{1}{3}\sigma_{\nu d\to\mu^- u}.
\end{aligned} \tag{A.10}$$

Putting this back into Eqs. A.8 and A.9 we get

$$\sigma^+_{NC} = \frac{1}{3}\left(\frac{4}{9}\sigma^+_{CC} + \frac{5}{9}\sigma^-_{CC}\right) \tag{A.11}$$
$$\sigma^-_{NC} = \frac{1}{3}\left(\frac{4}{9}\sigma^-_{CC} + \frac{5}{9}\sigma^+_{CC}\right). \tag{A.12}$$

Since the cross sections *must* be the same in the Monte Carlo and data by construction, we can get f^{DS}_{bak} by comparing the right side of Eq. A.12 between Monte Carlo and data in the NC data simulator. Recall that the NC data simulator measures the ρ component in the hadron jet of ν_μ CC events, i.e. σ^+_{CC} and σ^-_{CC}. So, in order to calculate f^{DS}_{bak}, we need to sum the NC data simulator contributions from both ρ^- and ρ^+ events.

The relative contributions from ρ^+ and ρ^- events appear to enter with different weights in the above. In the ratio of data to Monte Carlo overall constants cancel, but we are still left with a factor of 0.8 between the additive terms. We have made many simplifying assumptions in reaching relation A.12, though. Including sea quarks makes the disparity between σ^+_{CC} and σ^-_{CC} less pronounced, as does the introduction of quasi-elastic and resonance-producing neutrino interactions. We assumed that the selection efficiencies for ρ^+ and ρ^- were equal, but this analysis slightly favors ρ^+ because the negative backgrounds are larger.

Therefore, in light of the imprecision with which Eq. A.12 is derived, and especially in view of the limited statistics in Tab. 3.4, the exact deviation from parity between the ρ^+ and ρ^- samples is ignored in this analysis, and the two samples are simply added. As an additional benefit, implementing this method increases the available NC data simulator statistics.

Bibliography

[1] N. Bohr, *J. Chem. Soc. (London)* , 349 (1932).

[2] Laurie M. Brown, "The Idea of the Neutrino," *Physics Today*, September 1978, p. 23.

[3] S.A. Goudsmit, in [2], *Convegno di Fisica Nucleare* , 41 (1932).

[4] *Rapports du Septième Conseil de Physique Solvay, 1933*. Paris: Gauthier-Villars, 1934, p. 324 (in French); English translation of Pauli's comments in [2].

[5] F. Perrin, in [2], *Compt. Rend.* **197**, 1625 (1933).

[6] J. Chadwick, *Proc. Roy. Soc.* **A136**, 692 (1932).

[7] J.F. Carlson and J.R. Oppenheimer, *Phys. Rev.* **41**, 763 (1932).

[8] E. Fermi, *Z. Phys.* **88**, 161 (1934) (in German); English translation in F.L. Wilson, *Amer. J. Phys.* **36**, 1150 (1968).

[9] V.F. Weisskopf, in Exploring the History of Nuclear Physics (C. Weiner, ed.), New York: American Institute of Physics, 1972.

[10] N. Bohr, *Nature* **138**, 25 (1936).

[11] C.L. Cowan, Jr. et al., *Science* **124**, 103 (1956).

[12] B. Pontecorvo, Chalk River Report PD-205 (Chalk River, Canada, 1946).

[13] L. Alvarez, UCRL-328 (University of California Radiation Laboratory, 1949).

[14] F. Reines and C.L. Cowan, Jr., *Phys. Rev.* **92**, 830 (1953).

[15] C.S. Wu, *Phys. Rev.* **105**, 1413 (1957); R.L. Garwin, L.M. Lederman, and M. Weinrich, *Phys. Rev.* **105**, 1415 (1957).

[16] T.D. Lee and C.N. Yang, *Phys. Rev.* **105**, 1671 (1957); L. Landau, *Nucl. Phys.* **3**, 127 (1957); A. Salam, *Nuovo Cim.* **5**, 299 (1957).

[17] M. Goldhaber, L. Grodzins, and A.W. Sunyar, *Phys. Rev.* **109**, 1015 (1958).

[18] R.P. Feynman and M. Gell-Mann, *Phys. Rev.* **109**, 193 (1958).

[19] E.C.G. Sudarshan and R. Marshak, *Phys. Rev.* **109**, 1860 (1958).

[20] G. Feinberg, *Phys. Rev.* **110**, 1482 (1958).

[21] D. Bartlett et al., *Phys. Rev. Lett.* **8**, 120 (1962); S. Frankel et al., *Phys. Rev. Lett.* **8**, 123 (1962).

[22] B. Pontecorvo, *JETP* **37**, 1751 (1959) (in Russian); English translation in B. Pontecorvo, *Sov. Phys.–JETP* **10**, 1236 (1960).

[23] M. Schwartz, *Phys. Rev. Lett.* **4**, 306 (1960).

[24] G. Danby et al., *Phys. Rev. Lett.* **9**, 36 (1962).

[25] M.L. Perl et al., *Phys. Rev. Lett.* **35**, 1489 (1975).

[26] G.S. Abrams et al. (Mark II Collaboration), *Phys. Rev. Lett.* **63**, 2173 (1989).

[27] D. Decamp et al. (ALEPH Collaboration), *Phys. Lett.* **B231**, 519 (1989).

[28] C. Caso et al. (Particle Data Group), *Eur. Phys. J.* **C3**, 1 (1998).

[29] F.J. Hasert et al. (Gargamelle Collaboration), *Phys. Lett.* **B45**, 138 (1973).

[30] E.G. Cazzoli et al., *Phys. Rev. Lett.* **34**, 1125 (1975).

[31] S.R. Mishra et al., NEVIS-1465 (1992); published in *SLAC Summer Inst. 1991* pp. 407–426.

[32] K. Hirata et al. (Kamiokande II Collaboration), *Phys. Rev. Lett.* **58**, 1490 (1987).

[33] R.M. Bionta et al. (IMB Collaboration), *Phys. Rev. Lett.* **58**, 1494 (1987).

[34] L.L. Langer and R.J.D. Moffat, *Phys. Rev.* **88**, 689 (1952).

[35] K. Assamagan et al., *Phys. Rev. D* **53**, 6065 (1996).

[36] R. Barate et al. (ALEPH Collaboration), *Eur. Phys. J.* **C2**, 395 (1998).

[37] E. Majorana, *Nuovo Cim.* **14**, 171 (1937).

[38] L. Wolfenstein, *Phys. Rev. D* **17**, 2369 (1978).

[39] S.P. Mikheyev and A.Y. Smirnov, *Nuovo Cim.* **9C**, 17 (1986).

[40] R.N. Mohapatra and P.B. Pal, Massive Neutrinos in Physics and Astrophysics, Singapore: World Sci. Pub., 1991.

[41] J.N. Bahcall, N. Cabibbo, and A. Yahil, *Phys. Rev. Lett.* **28**, 316 (1972).

[42] L.J. Hall, V.A. Kostelecky, and S. Raby, *Nucl. Phys.* **B267**, 415 (1986).

[43] J. Schechter and J.W. Valle, *Phys. Rev. D* **24**, 1883 (1981).

[44] J. Schechter and J.W. Valle, *Phys. Rev. D* **22**, 2227 (1980).

[45] J.N. Bahcall, *Neutrino Physics and Astrophysics*, Cambridge University Press, 1989; J.N. Bahcall and R. Ulrich, *Rev. Mod. Phys.* **60**, 297 (1988); J.N. Bahcall and M.H. Pinsonneault, *Rev. Mod. Phys.* **64**, 885 (1992); J.N. Bahcall and M.H. Pinsonneault, *Rev. Mod. Phys.* **67**, 781 (1995); J.N. Bahcall, S. Basu, and M.H. Pinsonneault, *Phys. Lett.* **B433**, 1 (1998); S. Turck-Chièze et al., *Astrophys. J.* **335**, 415 (1988); S. Turck-Chièze and I. Lopes, *Astrophys. J.* **408**, 347 (1993); S. Turck-Chièze et al., *Phys. Rep.* **230**, 57 (1993); V. Castellani, S. Degl'Innocenti, and G. Fiorentini, *Astron. Astrophys.* **271**, 601 (1993); V. Castellani et al., *Phys. Lett.* **B324**, 425 (1994); F. Ciacio et al., *Astron. Astrophys. Suppl. Ser.* **123**, 449 (1997).

[46] S.M. Bilenky, C. Giunti, and W. Grimus, "Phenomenology of Neutrino Oscillations", hep-ph/9812360 and UWTHPH-1998-61 (Vienna, December 1998), to be published in *Prog. Part. Nucl. Phys.* **43**, ().

[47] R. Davis, Jr., D.S. Harmer, and K.C. Hoffman, *Phys. Rev. Lett.* **20**, 1205 (1968).

[48] A.I. Abazov et al. (SAGE Collaboration) *Phys. Rev. Lett.* **67**, 3332 (1991); J.N. Abdurashitov et al.(SAGE Collaboration), *Phys. Lett.* **B328**, 234 (1994); J.N. Abdurashitov et al.(SAGE Collaboration), *Phys. Rev. Lett.* **77**, 4708 (1996).

[49] P. Anselmann et al.(GALLEX Collaboration), *Phys. Lett.* **B285**, 376 (1992); W. Hampel et al.(GALLEX Collaboration), *Phys. Lett.* **B388**, 384 (1996).

[50] K.S. Hirata et al.(Kamiokande II Collaboration), *Phys. Rev. Lett.* **65**, 1297 (1990); Y. Fukuda et al.(Kamiokande III Collaboration), *Phys. Rev. Lett.* **77**, 1683 (1996).

[51] Y. Fukuda et al. (Super-Kamiokande Collaboration), *Phys. Rev. Lett.* **82**, 1810 (1999).

[52] N. Hata and P. Langacker, *Phys. Rev. D* **56**, 6107 (1997).

[53] Sudbury Neutrino Observatory (SNO), `http://www.sno.phy.queensu.ca/`.

[54] Imaging Cosmic and Rare Underground Signal (ICARUS),
`http://www.aquila.infn.it/icarus/`;
P. Cennini et al. (ICARUS Collaboration), LNGS-94-99-I (1994); A. Rubbia et al. (ICARUS Collaboration), CERN-SPSLC-96-58 (1996).

[55] Borexino Experiment, `http://borex.lngs.infn.it/borex/about/`.

[56] Kamioka Liquid scintillator Anti-Neutrino Detector (KamLAND),
`http://www.awa.tohoku.ac.jp/html/KamLAND/`;
P. Alivisatos et al. (KamLAND COllaboration), "KamLAND: A Liquid Scintillator Anti-Neutrino Detector at the Kamioka Site", Stanford-HEP-98-03 and Tohoku-RCNS-98-15 (July 1998).

[57] HELium à la température de L'AZote liquide (HELLAZ),
`http://cdfinfo.in2p3.fr/Experiences/Hellaz/hellaz.html`,
`http://sg1.hep.fsu.edu/hellaz/`.

[58] M. Honda et al., *Phys. Rev. D* **52**, 4985 (1995); V. Agrawal et al., *Phys. Rev. D* **53**, 1314 (1996); G.K. Gaisser et al. *Phys. Rev. D* **54**, 5578 (1996).

[59] V. Barger et al., "Neutrino Decay and Atmospheric Neutrinos", hep-ph/9907421 and MADPH-99-1127 (Wisconsin, July 1999).

[60] N. Fornengo, M.C. Gonzalez-Garcia, and J.W.F. Valle, "On the Interpretation of the Atmospheric Neutrino Data in Terms of Flavor Changing Neutrino Interactions", hep-ph/9906539 and FTUV-99-45 (Valencia, June 1999).

[61] F. Reines et al., *Phys. Rev. Lett.* **15**, 429 (1965).

[62] C.V. Achar et al., *Phys. Lett* **18**, 196 (1965).

[63] T.J. Haines et al. (IMB Collaboration), *Phys. Rev. Lett.* **57**, 1986 (1986).

[64] C.R. Wuest et al. (IMB Collaboration), *Nucl. Instr. Meth.* **A239**, 467 (1985); R. Claus et al. (IMB Collaboration), *Nucl. Instr. Meth.* **A261**, 540 (1987).

[65] Kamioka Nuclear Decay Experiment (Kamiokande),
`http://www-sk.icrr.u-tokyo.ac.jp/doc/kam/kamiokande.html`.

[66] Ch. Berger et al. (Fréjus Collaboration), *Nucl. Instr. Meth.* **A262**, 463 (1987); Ch. Berger et al. (Fréjus Collaboration), *Nucl. Instr. Meth.* **A302**, 406 (1991).

[67] R. Becker-Szendy et al. (IMB Collaboration), *Nucl. Phys. B (Proc. Suppl.)* **38**, 331 (1995); E. Kearns, *Nucl. Phys. B (Proc. Suppl.)* **70**, 315 (1999).

[68] K. Daum et al. (Fréjus Collaboration), *Z. Phys. C* **66**, 417 (1995).

[69] M. Aglietta et al. (NUSEX Collaboration), *Europhys. Lett.* **8**, 611 (1989).

[70] T. Kafka, *Nucl. Phys. B (Proc. Suppl.)* **70**, 340 (1999).

[71] Y. Fukuda et al. (Kamiokande Collaboration), *Phys. Lett.* **B335**, 237 (1994).

[72] K.S. Hirata et al. (Kamiokande Collaboration), *Phys. Lett* **B280**, 146 (1992).

[73] Y. Fukuda et al.(Super-Kamiokande Collaboration), *Phys. Rev. Lett.* **81**, 1562 (1998).

[74] M. Messier, Talk presented at *1999 Meeting of the Division of Particles and Fields of the American Physical Society (DPF '99)*, UCLA, 5–9 January 1999, published electronically in the conference proceedings:
`http://www.library.ucla.edu/dpf99/`.

[75] G.G. Raffelt, "Neutrino Astrophysics at the Cross Roads", hep-ph/9902271 (February 1999), to be published in *Proc. 1998 Summer School in High-Energy Physics and Cosmology, ICTP, Trieste, Italy, 29 June–17 July 1998*, ed. by G. Senjanovic and A. Yu. Smirnov, World Scientific, Singapore.

[76] M. Apollonio et al. (CHOOZ Collaboration), *Phys. Lett.* **B420**, 397 (1998).

[77] W.M. Alberico and S.M. Bilenky, "New Developments in Neutrino Physics", hep-ph/9905254 and DFTT-26-1999 (Turin, May 1999).

[78] Y. Declais et al. (Bugey Collaboration), *Phys. Lett.* **B338**, 383 (1994).

[79] G. Zacek et al. (Gösgen Collaboration), *Phys. Rev. D* **34**, 2621 (1986).

[80] A.A. Kuvshinnikov et al. (Krasnoyarsk Collaboration), *JETP Lett.* **54**, 255 (1991).

[81] F. Böhm et al. (Palo Verde Collaboration), "Proposal for the San Onofre Neutrino Oscillation Experiment", Caltech 1994; "Addendum to the San Onofre Proposal", Calt-63-721 (1996).

[82] G. Gratta, "Neutrino Oscillation Experiments at Nuclear Reactors", hep-ex/9905011 and STANFORD-HEP-99-02 (April 1999), submitted to World Scientific, to be included in *Proceedings of WIN99, Cape Town, South Africa, Jan99*.

[83] C. Athanassopoulos et al. (LSND Collaboration), *Phys. Rev. Lett.* **77**, 3082 (1996).

[84] C. Athanassopoulos et al. (LSND Collaboration), *Phys. Rev. Lett.* **81**, 1774 (1998).

[85] G. Drexlin et al. (KARMEN Collaboration), *Nucl. Instr. Meth.* **A289**, 490 (1990).

[86] B. Armbruster (for KARMEN Collaboration), Talk presented at the XXXIIInd *Rencontres de Moriond: Electroweak Interactions and Unified Theories*, Les Arcs 1800 (France), 14–21 March 1998, cited in [46].

[87] Booster Neutrino Experiment (BooNE), `http://www.neutrino.lanl.gov/BooNE/` and `http://www-boone.fnal.gov/`.

[88] I-216 experiment at CERN, `http://chorus01.cern.ch/ pzucchel/loi/`.

[89] Oak Ridge Large Neutrino Detector (ORLaND), `http://www.phys.subr.edu/orland/`.

[90] Neutrinos at the European Spallation Source (NESS), `http://www.isis.rl.ac.uk/ess/neut%5Fess.htm`.

[91] N. Ushida et al. (FNAL-E531 Collaboration), *Phys. Rev. Lett.* **57**, 2897 (1986).

[92] M. Gruwe et al. (CHARM-II Collaboration), *Phys. Lett.* **B309**, 463 (1993).

[93] E. Eskut et al. (CHORUS Collaboration), *Nucl. Instr. Meth.* **A401**, 7 (1997).

[94] L.A. Ahrens et al. (BNL-E734 Collaboration), *Phys. Rev.* **D36**, 702 (1987).

[95] L. Borodovsky et al. (BNL-E776 Collaboration), *Phys. Rev. Lett.* **68**, 274 (1992).

[96] W. Von Ruden for the CDHSW Collaboration, *IEEE Trans. Nucl. Sci.* **29**, 360 (1982).

[97] W.K. Sakumoto et al. (CCFR Collaboration), *Nucl. Instr. Meth.* **A294**, 179 (1990); B.J. King et al. (CCFR Collaboration), *Nucl. Instr. Meth.* **A302**, 254 (1991).

[98] J. Altegoer et al. (NOMAD Collaboration), *Nucl. Instr. Meth.* **A404**, 96 (1998).

[99] J. Astier et al. (NOMAD Collaboration), *Phys. Lett.* **B453**, 169 (1999).

[100] The CHORUS Collaboration, Contribution to XIXth *International Symposium on Lepton and Photon Interactions at High-Energies* (LP 99), Stanford, CA, 9-14 August 1999.

[101] K. Nishikawa et al. (K2K Collaboration), "E362 KWK-PS Proposal", March 1995; K. Nishikawa et al. (K2K Collaboration), *Nucl. Phys. (Proc. Suppl.)* **B59**, 289 (1997).

[102] E. Ables et al. (MINOS Collaboration), "Main Injector Neutrino Oscillation Search", FERMILAB-PROPOSAL-P-875 (1995); D. Ayres et al. (MINOS Collaboration), NUMI-L-63 (1995).

[103] H. Shibuya et al. (OPERA Collaboration), CERN-SPSC-97-24 (1997); H. Shibuya et al. (OPERA Collaboration), CERN-SPSC-98-25 (1998).

[104] M. Ambrosio et al. (NOE Collaboration), *Nucl. Instr. Meth.* **A363**, 604 (1995); INFN-AE-98-09 (1998); G.C. Barbarino et al. (NOE Collaboration), INFN-AE-96-11 (1996).

[105] T. Ypsilantis et al.(AQUA-RICH Collaboration), CERN-LAA-96-13 (1996).

[106] G. Baldini et al. (NICE Collaboration), LNGS-LOI-98-13 (1998).

[107] G.F. Smoot et al., *Astrophys. J* **396**, 3, 115-B5 (1992); *Astrophys. J* **396**, L1, 160-B1 (1992).

[108] M.L. Fisher et al., *Astrophys. J* **388**, 242, 53-C11 (1992).

[109] A.N. Taylor and M. Rowan-Robinson, *Nature* **359**, 396 (1992).

[110] G. Acquistapace et al., CERN-ECP 95-14 (July 1995).

[111] K. De Winter et al. (CHARM-II Collaboration), *Nucl. Instr. Meth.* **A278**, 670 (1989); D. Geiregat et al. (CHARM-II Collaboration), *Nucl. Instr. Meth.* **A325**, 92 (1993).

[112] Application Software Group, "GEANT: Detector Description and Simulation Tool", CERN Programming Library Long Writeup W5013.

[113] K. Lassila, CERN-CN-91-13 (1991); P.A. Aarnio et al., CERN-TIS-93-08-CF (1993), published in *MC 93: Proceedings*, P. Dragovitsch, S.L. Linn, and M. Burbank, eds., Singapore: World Sci., 1994.

[114] G. Collazuol et al., CERN-OPEN-98-032 (November 1998).

[115] R. Das and S. Mishra, "Measurement of the Neutrino Flux in NOMAD", NOMAD memo 97-038 (October 1997).

[116] F. Weber et al., "The Construction and Use of the Flux Reweighting Tables", NOMAD memo 97-037 (November 1997).

[117] B. van de Vyver, *Nucl. Instr. Meth.* **A385**, 91 (1997); M.C. González-Garcia and J.J. Gómez-Cadenas, *Phys. Rev.* **D55**, 1297 (1997).

[118] M. Baldo-Ceolin et al., *Z. Phys.* **C63**, 409 (1994).

[119] M. Barranco-Luque et al. (The UA1 Collaboration), *Nucl. Instr. Meth.* **A176**, 175 (1980).

[120] A. Geiser, P. Nedelec, and R. Petti, "The 1996 $\overline{V} \times T_1 \times T_2$ Filter", NOMAD memo 97-008 (July 1998).

[121] G. Bassompierre et al., *Nucl. Instr. Meth.* **A403**, 363 (1998); G. Bassompierre et al., *Nucl. Instr. Meth.* **A411**, 63 (1998).

[122] D. Autiero et al., *Nucl. Instr. Meth.* **A373**, 358 (1996).

[123] P. Hurst, "The Performance of the Hadron Calorimeter", NOMAD memo 97-042 (November 1997).

[124] K. Eggert et al., *Nucl. Instr. Meth.* **A176**, 217 (1980).

[125] K. Varvell, "NOMAD Reconstruction Software: NOMAD DST Package Version v7r3", NOMAD Software Note, February 1998.

[126] J.-P. Meyer and A. Rubbia, "NOMAD Event Generator Off-Line Manual", version 5.00, NOMAD Software Note, December 1994.

[127] G. Ingleman, "LEPTO Version 6.1: The Lund Monte Carlo for Deep Inelastic Lepton–Nucleon Scattering", *Physics at HERA* (proceedings), vol. 3, p. 1366 (October 1991).

[128] J. Altegoer et al., "NOMAD GEANT Off-Line Manual", version 5.12, NOMAD Software Note, September 1996.

[129] H.C. Fesefeldt, "Simulation of Hadronic Showers", PITHA report 85-02 (RWTH Aachen, September 1985).

[130] F. Weber, "A Search for $\nu_\mu \rightarrow \nu_e$ Oscillations Using ν_e CC Events in the 1995 Data", NOMAD memo 97-029 (July 1997).

[131] B. Yabsley, "Particle Identification Using TRD Information", NOMAD memo 97-028 (July 1997).

[132] E. Gangler, private communication.

[133] R. Cousins, "Ills of the Phi–Phi Plot and How to Cure Them", NOMAD memo 97-035 (July 1997).

[134] L. DiLella, private communication.

[135] J.J. Gomez-Cadenas and J.A. Hernando, "Search for nu_mu-¿nu_tau Oscillations Using the tau-¿3pi nu Decay Channel", NOMAD memo 97-032 (July 1997); M.J. Costa, J.A. Hernando, and J.J Gomez-Cadenas, "Study of Correlation in the tau-¿3pi Analysis Using Uniform Variables", NOMAD memo 97-040 (November 1997).

[136] The multidimensional likelihood method and the likelihood array smoothing technique were both suggested and developed by G. Feldman (private communication).

[137] R. Cousins, "A Method for ν_τ CC Simulation in Nomad [sic] Using ν_μ CC Events", NOMAD memo 98-001 (January 1998).

[138] S. Baker and R. Cousins, *Nucl. Instr. Meth.* **221**, 437 (1984).

[139] F. James, "MINUIT: Function Minimization and Error Analysis", CERN Programming Library Long Writeup D506.

[140] C.G. Arroyo et al. (CCFR Collaboration), *Phys. Rev. Lett.* **72**, 3452 (1994).

[141] G. Feldman and R. Cousins, *Phys. Rev. D* **57**, 3873 (1998).

[142] G. Feldman and A. Geiser, "Calculation of $\nu_\tau \rightarrow \nu_\mu$ Oscillation Limits", NOMAD memo 99-001 (June 1999).

[143] `nomad_bins`, a FORTRAN program written by G. Feldman.

[144] P. Astier et al. (NOMAD Collaboration), "Current Results from the ν_τ Appearance Search in NOMAD", 6 December 1999, to be published.

[145] A. Geiser, "Reduction of Charge Bias in the NC Data Simulator", NOMAD memo 97-031 (July 1997).